The Effects of Ice Crystal Shape on the Evolution of Optically Thin Cirrus Clouds in the Tropics

Rick Russotto

A thesis
submitted in partial fulfillment of
the requirements for the degree of

Master of Science

University of Washington

2015

Reading Committee:

Thomas P. Ackerman, Chair

Dale R. Durran, Chair

Robert Wood

Program Authorized to Offer Degree:
Department of Atmospheric Sciences

University of Washington

Abstract

The Effects of Ice Crystal Shape on the Evolution of
Optically Thin Cirrus Clouds in the Tropics

Rick Russotto

Co-Chairs of the Supervisory Committee:
Professor Thomas P. Ackerman
Department of Atmospheric Sciences

Professor Dale R. Durran
Department of Atmospheric Sciences

Thin cirrus clouds in the tropical tropopause layer (TTL) play potentially important roles in Earth's radiation budget and in the transport of water into the stratosphere. Radiative heating of these clouds results in mesoscale circulations that maintain them against sedimentation and redistribute water vapor. In this study, the System for Atmospheric Modeling (SAM) cloud-resolving model is modified in order to calculate the fall speeds, growth rates, and radiative absorption coefficients of non-spherical ice crystals. This extended model is used in simulations that aim to constrain the effects of ice crystal shape on the time evolution of thin cirrus clouds and to identify the physical processes responsible. Model runs assuming spheroidal crystals result in a higher center of cloud ice mass than in the control, spherical case, which is roughly 60% due to a reduction in fall speeds and 40% due to stronger updrafts caused by stronger radiative heating. Other effects of ice crystal shape on the cloud evolution include faster growth and sublimation in supersaturated and subsaturated environments, respectively, and local temperature increases caused by diabatic heating. Effects of ice crystal shape on the total and mean ice crystal masses are within about 10% but do not appear to be entirely negligible. Comparisons of modeled ice crystal size distributions with recent airborne observations of

TTL cirrus show that incorporating non-spherical shape has the potential to bring the model closer to observations. It is hoped that this work will eventually lead towards a more realistic physical representation of thin tropical cirrus in global climate models.

TABLE OF CONTENTS

LIST OF FIGURES

LIST OF TABLES

NOMENCLATURE

α	thermal accommodation coefficient for ice
β	aspect ratio of a spheroid
β	deposition coefficient for water vapor on ice
Δz	thickness of cloud layer
Δ_d	water vapor jump length
Δ_k	thermal jump length
$F_{\text{bot}}^{\downarrow}$	downward radiation flux at cloud bottom
$F_{\text{top}}^{\downarrow}$	downward radiation flux at cloud top
$F_{\text{bot}}^{\uparrow}$	upward radiation flux at cloud bottom
$F_{\text{top}}^{\uparrow}$	upward radiation flux at cloud top
Γ	aspect ratio of hexagonal plate or column
κ	dynamic shape factor
λ	wavelength
λ_{air}	mean free path of air
μ	dynamic viscosity of air
ω_0	single-scattering albedo

$\overline{\mu}$	cosine of effective zenith angle
$\mathcal{P}$	Prandtl number
$\mathcal{R}$	Reynolds number
ρ_{air}	density of air
$\mathcal{S}$	Schmidt number
σ	Stefan-Boltzmann constant
σ_{abs}	absorption cross section
σ_{ext}	extinction cross section
τ	optical depth
θ'	perturbation potential temperature
A	area of smallest possible ellipse or circle that circumscribes a falling particle in a plane normal to its fall direction
A	linear eccentricity of an ellipse
A	surface area
a	for a column or plate, the distance along hexagonal face from the center to one of the vertices
a	initial cloud quarter-width
a	semi-major axis of an ellipse
A_e	cross-sectional area in a plane normal to a particle's fall direction

B	blackbody emission
b	semi-minor axis of an ellipse
C	capacitance
c	length of column or thickness of plate
C_c	Cunningham slip-correction factor
C_p	heat capacity of air at constant pressure
d	half of initial cloud thickness
D_v	diffusivity of water vapor in air
D_v'	modified diffusivity of water vapor in air
e	eccentricity of an ellipse
e	the base of natural logarithms
$e_{\text{sat,ice}}$	saturation vapor pressure over planar ice surface
$f(x)$	specifies dependence of initial ice crystal number concentration on longitude
$f_{k,d}$	surface non-equilibrium coefficient for vapor diffusivity
$f_{k,k}$	surface non-equilibrium coefficient for thermal conductivity
$f_{v,d}$	ventilation coefficient for vapor diffusivity
$f_{v,k}$	ventilation coefficient for thermal conductivity
FC	radiative flux convergence

g	acceleration due to gravity
g	asymmetry factor
$g(z)$	specifies dependence of initial ice crystal number concentration on altitude
k_a	thermal conductivity of air
k_a'	modified thermal conductivity of air
L	characteristic length scale
L_s	latent heat of sublimation of ice
m	ice crystal mass
m_{Im}	imaginary part of index of refraction
m_{Re}	real part of index of refraction
N	ice crystal number concentration
N_0	maximum ice crystal number concentration in initialized cloud
N_{broad}	number concentration of broadening gases
N_s	number concentration of spheres of radius r_{VA} needed to conserve mass when replacing a cloud of non-spherical ice crystals
p	air pressure
p_{ref}	reference pressure; represents surface pressure; 1×10^5 Pa
q_v	water vapor mixing ratio

$q_{v,s}^{*}$	saturation mixing ratio at initial cloud center
r	sphere radius
R_{air}	gas constant for dry air
R_{v}	gas constant for water vapor
r_{VA}	radius of sphere of equal surface area to volume ratio
r_{V}	radius of sphere of equal volume
S_{ice}	saturation ratio with respect to ice
T	temperature
t	transmissivity
T_{r}	reference temperature; melting point of ice; 273.15 K
u	zonal component of wind velocity
V	volume
v	terminal velocity
$v_{\text{Böhm}}$	terminal velocity following *Böhm* (1989)
v_{Stokes}	terminal velocity following Stokes's Law
w	vertical component of wind velocity
X	Davies number
X	cube root of the Schmidt number times square root of the Reynolds number

Y	cube root of the Prandtl number times square root of the Reynolds number
z	altitude
z_{bot}	altitude of bottom of cloud
z_{top}	altitude of top of cloud
z_c	initial height of cloud center
ADDA	Amsterdam Discrete Dipole Approximation
ATTREX	Airborne Tropical Tropopause Experiment
CALIPSO	Cloud-Aerosol Lidar and Infrared Pathfinder Satellite Observations
DISORT	discrete-ordinates method code
GCM	global climate model
IGOM	Improved Geometric Optics Method
LW	longwave
PMOM	phase function moment in DISORT and RRTM codes
RAPRAD	Rapid Calculation of Radiative Heating Rates model
RRTM	Rapid Radiative Transfer Model
SAM	System for Atmospheric Modeling cloud-resolving model
SW	shortwave
TTL	tropical tropopause layer

AUTHOR'S NOTE

I have made extensive use of footnotes and appendices in order to allow the main text to flow better while including details that may be important for people (including myself) trying to reproduce or extend my work. I hope this thesis will be detailed enough that future students working on similar projects will be able to reproduce what I did. I encourage future readers to contact me with any questions.

ACKNOWLEDGMENTS

Chapter 1

INTRODUCTION

Optically thin cirrus clouds in the tropics have recently been a topic of interest in the atmospheric science community. These clouds are located in the tropical tropopause layer (TTL), which is defined by *Fueglistaler et al.* (2009) as a transition layer with properties of both the troposphere and stratosphere located between about 14.0 and 18.5 km. Satellite observations have shown that thin cirrus are common in the TTL (e.g. *Wang et al.*, 1996; *Mace et al.*, 2009; *Virts and Wallace*, 2010). While these clouds are too optically thin in the shortwave to be visible to the naked eye, they absorb longwave radiation. This results in radiative heating rates of several K/day (*Jensen et al.*, 1996a; *Comstock et al.*, 2002), suggesting an important role for these clouds in Earth's radiation budget.

In addition, TTL cirrus play an as-yet unquantified role in the exchange of water vapor between the troposphere and stratosphere. Water vapor is a greenhouse gas, and changes in stratospheric water vapor have potential global climate impacts. For example, *Solomon et al.* (2010) argued that the roughly 10% decline in stratospheric water vapor between 2000 and 2010 helped to reduce the rate of surface warming since that time. Water vapor also plays key roles in catalyzing stratospheric ozone depletion, both in the gas phase, by providing a source of OH radicals (*Dvortsov and Solomon*, 2001), and in mixed-phase chemistry, by acting as a constituent of polar stratospheric clouds, which provide a surface for reactions in which free chlorine radicals are formed (*Solomon et al.*, 1986). For these reasons, there is considerable interest in the climate and atmospheric chemistry communities in understanding the processes governing the exchange of water vapor between the troposphere and stratosphere.

The principal source of water vapor in the lower stratosphere is transport across the tropical tropopause, a source first recognized by *Brewer* (1949).[1] The stratosphere is very dry, with water vapor mixing ratios less than 4 ppmv in the tropical lower stratosphere (e.g. *le Texier et al.*, 1988), because air enters the stratosphere through the cold TTL as part of the Brewer-Dobson circulation, forcing most of the water vapor to deposit onto ice crystals.

Efforts to more quantitatively understand the processes governing transport of water vapor into the stratosphere have proven difficult. It has long been recognized (e.g. *Newell and Gould-Stewart*, 1981) that the zonal mean tropical tropopause temperature is too warm to account for the observed stratospheric dryness if air rises uniformly through the tropopause into the stratosphere and is dehydrated to its saturation vapor pressure. *Holton and Gettelman* (2001) argued that horizontal transport of water vapor through the coldest longitudes of the TTL, *i.e.* the western Pacific, would be enough to dehydrate the stratosphere to observed levels. To test this hypothesis, *Jensen and Pfister* (2004) ran a 1-dimensional Lagrangian cloud model following horizontal trajectories in the TTL. These simulations predicted *lower* than observed stratospheric humidities, indicating that a missing source of water vapor needed to be accounted for.

It has been hypothesized that thin TTL cirrus help hydrate the stratosphere because radiative heating of the clouds induces a circulation that advects water vapor upward (*Corti et al.*, 2006). However, this circulation can also help dehydrate the stratosphere by encouraging growth and sedimentation of ice crystals (*Jensen et al.*, 1996b). The complexity of the interactions between TTL cirrus and troposphere-stratosphere water vapor exchange, as well as a more general desire to understand how the observed TTL cirrus are formed and maintained, has motivated study of these clouds with sophisticated cloud-resolving models. Over the past few years, much work in this area has been

---

[1]In the upper stratosphere, another major water source is the oxidation of methane, a source first recognized by *Bates and Nicolet* (1950), but this source is less important in the lower stratosphere because the air there has not yet had enough time for much of its methane to be oxidized.

done by Dr. Tra Dinh, a recent graduate of the Department of Atmospheric Sciences at the University of Washington, and Drs. Dale Durran and Thomas Ackerman, professors in the department.

Initially, *Durran et al.* (2009) used a 2-D cloud-resolving model to numerically simulate the dynamical response to radiative heating of ice crystals in TTL cirrus. Their model assumed that all ice crystals were spherical with a radius of 4.2 μm and did not consider the effects of sedimentation of ice crystals, but the simulated updraft speeds were greater than the terminal fall speeds of the ice crystals, suggesting that the radiatively induced circulation could maintain the clouds against sedimentation for at least a few hours. Subsequently, *Dinh et al.* (2010) implemented a bin microphysics scheme, which explicitly calculated diffusional growth rates and fall speeds for spherical ice crystals of various masses. This expanded model showed that a thermally induced circulation led to moisture convergence in the cloud, allowing ice crystals to grow despite diabatic heating, and that the thermally induced circulation could maintain the cloud against sedimentation for several days without requiring large-scale uplift.[2] This provided a mechanism to explain observations of TTL cirrus persisting for several days (*Winker and Trepte*, 1998; *Taylor et al.*, 2011).

Jensen et al. (2011) argued that strong wind shear could dissipate the cirrus before the radiatively induced circulation could form, so it needed to be shown that the radiatively induced circulation could maintain the clouds even in the presence of a realistic large-scale dynamical regime. This was done by *Dinh et al.* (2012), who simulated TTL cirrus induced by an equatorial Kelvin wave. To improve numerical efficiency with the large-scale flow included, the dynamical core of the model was switched from Dr. Durran's Meso06 model to the System for Atmospheric Modeling (SAM), described in *Khairoutdinov and Randall* (2003). An improved bin microphysics scheme, described in *Dinh and Durran* (2012), was also implemented. These simulations showed that even

---

[2]Work up to this point is also described in the M.S. thesis by *Dinh* (2009).

in the presence of realistic large-scale motion, including time-varying wind shear, the cloud was still maintained by the radiatively induced circulation. Under the conditions specific to their simulations, the circulation resulted in net upward transport of water vapor, because the upward advection of water vapor more than compensated for the sedimentation of ice crystals.[3] *Dinh et al.* (2014) further explored the way an individual thin cirrus cloud redistributes the moisture field in its environment and found that the cloud results in an upward flux of water vapor in a subsaturated environment but a downward flux of water vapor in a supersaturated environment. *Dinh and Fueglistaler* (2014) found that the most important large-scale effect of thin cirrus on stratospheric water vapor is the temperature increase caused by the cloud radiative heating, which allows more water vapor to reach the stratosphere without leaving the gas phase. A positive feedback, not currently represented in global climate models, exists between the radiative heating, the mesoscale circulation, and the growth of ice crystals.

The importance of the circulation induced by radiative heating of cirrus ice crystals suggests that the simulation of the microphysics and radiative transfer should be made as accurate as possible. Model simulations by Dinh *et al.* up to this point have assumed that all ice crystals are spherical, which results in discrepancies between modeled and observed ice crystal size distributions, particularly for larger crystals.[4] Non-spherical crystals would be expected to fall more slowly and therefore grow to larger sizes than their spherical counterparts before falling out, possibly leading to better agreement with observations. To develop the infrastructure to test this hypothesis, and to try to con-

---

[3]Work up to this point is also described in the Ph.D. thesis by *Dinh* (2012).

[4]More specifically, *Dinh et al.* (2012) found that the assumption of spherical crystals led to an underestimate of the concentrations of crystals > 20 μm in length, compared with observations. To try to reconcile this discrepancy, they replaced 2% of the crystals in the model output with hexagonal plates, and 1% with hexagonal columns, with aspect ratios of 6, as suggested by observations (*Lawson et al.*, 2008). They were sized so that their terminal velocities matched those of the spherical crystals that they replaced. Since plates or columns fall slower than spheres of the same mass, the replacement crystals were heavier, so their number concentration was decreased in order to conserve mass. Despite the decrease in concentration, the ice crystal size distribution (based on length of maximum dimension) from this post-processing calculation agreed with observations much better than the raw model output, due to the extended lengths of the non-spherical crystals.

strain the possible effects of ice crystal shape on the evolution and maintenance of thin TTL cirrus, I have incorporated non-spherical ice crystals into the SAM cloud-resolving model. Chapter 2 describes changes to the model microphysics, including ice crystal fall speeds and growth rates. Chapter 3 describes the incorporation of non-spherical crystals into the model's radiative absorption calculations. Chapter 4 describes SAM simulations to test the effects of these changes on the simulated cloud properties. Chapter 5 contains conclusions and possible directions for future work.

Chapter 2

IMPROVEMENTS TO MODEL MICROPHYSICS

Plate and columnar crystals are often represented in models as oblate and prolate spheroids, respectively, because for these shapes, analytical solutions exist for the growth rate and fall speed calculations, whereas actual hexagonal prisms would require detailed numerical computations or empirically derived approximations.[1] This is the approach I have chosen for representing non-spherical ice crystals in SAM, for the purposes of the microphysical calculations. Model treatments of the fall speeds and growth rates for spheroidal crystals are described in Sections 2.1 and 2.2, respectively.[2]

2.1 Ice crystal fall speeds

2.1.1 Fall speed calculations for spherical ice crystals

I will first describe the calculation of the terminal fall speeds of spherical ice crystals, including changes I have made to this calculation. *Dinh et al.* (2012) calculated terminal fall speeds according to (*Böhm*, 1989):

$$v_{\text{Böhm}} = \frac{\mu \mathcal{R}}{2\rho_{\text{air}}r} \tag{2.1}$$

where μ is the dynamic viscosity of air, $\mathcal{R}$ is the Reynolds number, ρ_{air} is the density of air, and r is the radius of the ice crystal. The dynamic viscosity of air is calculated

---

[1]The study of ice crystal growth in subvisible cirrus by *Jensen et al.* (2008) is one example of a study using a spheroid model for fall speed and growth rate calculations.

[2]In the ice microphysics observation community, "spheroids" often refers to any nearly spherical particle. Here I am using the mathematical definition of a spheroid as the solid formed by rotating an ellipse about its major (for a prolate spheroid) or minor (for an oblate spheroid) axis.

according to the empirical expression (*Rogers and Yau*, 1989, p. 102)

$$\mu = \frac{\left(6.7596 \times 10^{-3}\right)\left(\frac{T}{273.15}\right)^{1.5}}{T + 120} \tag{2.2}$$

where T is the temperature in degrees Kelvin. The Reynolds number is defined as $\mathcal{R} = \rho_{\text{air}} v L / \mu$, where v is the fall speed and L is the characteristic length scale. In the case of a spherical particle, $L = 2r$. However, since this definition of $\mathcal{R}$ requires knowledge of v, which is what we are trying to calculate, we need an alternative way of obtaining $\mathcal{R}$. *Böhm* (1989) closed this problem by calculating the Reynolds number with the following empirical expression:

$$\mathcal{R} = 8.5 \left[\sqrt{1 + 0.1519 X^{1/2}} - 1\right]^2 \tag{2.3}$$

where X is the Davies number, calculated according to

$$X = \frac{8mg\rho_{\text{air}}}{\pi \mu^2} \left(\frac{A}{A_e}\right)^{1/4} \tag{2.4}$$

where m is the mass of the particle, g is the acceleration due to gravity, A_e is the cross-sectional projected area of the particle on a plane normal to the fall direction, and A is the area of the smallest possible ellipse or circle on that plane which circumscribes the particle.

Equation 2.1 is intended to be a general equation for terminal fall speeds of hydrometeors across a wide range of sizes, including large particles such as graupel and hail. However, *Böhm* (1989) does not test it for $\mathcal{R} \ll 1$, which, as shown later, is the case for ice crystals in TTL cirrus. The ratio A/A_e may appear to provide a potential way to correct for ice crystal shape, but for spheroidal particles, A/A_e is still unity because spheroids have circular or elliptical cross-sections, so this correction would show no difference between the fall speeds of spheroidal and spheroidal particles. Also note that an irregular shape, for which $A/A_e > 1$, would imply a *greater* fall speed than for a spherical particle. This may be appropriate for large particles such as hailstones, but not for the ice crystals that comprise cirrus clouds.

For small, spherical particles, there is a more specific expression for the fall speed, based on Stokes flow theory (*Fuchs*, 1964, p.23; *Lamb and Verlinde*, 2011, p. 388):

$$v_{\text{Stokes}} = \frac{2}{9} \frac{\rho_{\text{ice}} g}{\mu_{\text{air}}} r^2 \tag{2.5}$$

This expression is valid in the Stokes fluid dynamical regime, wherein the particle is large enough that the air can be treated as a continuum ($L >> \lambda_{\text{air}}$, where λ_{air} is the mean free path of air), but small enough that the inertia of the displaced fluid is negligible ($\mathcal{R} << 1$) (*Lamb and Verlinde*, 2011, p. 386).

To demonstrate that the latter condition is reasonable for ice crystals in thin TTL cirrus, consider the following conservatively large estimate for $\mathcal{R}$. The largest ice crystals observed in TTL cirrus have a length of about $L = 100~\mu$m (*Lawson et al.*, 2008). Updraft velocities may reach, at most, on the order of 10 mm/s (*Dinh et al.*, 2010). Since the TTL is about 2 scale heights above the ground, let $\rho_{\text{air}} = 1.2 \times e^{-2} = 0.162~\text{kg m}^{-3}$. Finally, the dynamic viscosity of air at 180 K (a conservatively low temperature) is about 1.2×10^{-5} kg m^{-1} s^{-1}, using Equation 2.2. This gives a value of $\mathcal{R}$ of about 0.0135, which is much less than 1. Therefore, effects of the inertia of the displaced fluid should not be important for our simulations.

As for the condition that $L >> \lambda_{\text{air}}$, the particle diameter may be comparable to λ_{air} for the smaller size bins in the model. In the model simulations described in Chapter 4, the center of the cloud is at an altitude of 16.25 km. At this altitude, in the U.S. Standard Atmosphere, the mean free path of air is 5.07642×10^{-7} m.[3] The smallest size bin in our model has a particle diameter of 5×10^{-7} m, so the Stokes regime may not be completely valid for the smaller crystals in the simulation. There exists a simple, empirical correction to the Stokes fall speed in the transition regime where the non-continuum nature of the fluid becomes important. This correction is called the Cunningham slip-correction

---

[3]Values from the 1976 U.S. Standard Atmosphere can be obtained at <http://www.luizmonteiro.com/StdAtm.aspx>.

factor and is calculated according to: (*Lamb and Verlinde*, 2011, p. 386)

$$C_c = 1 + (1.26)\frac{\lambda_{\text{air}}}{r} \ . \tag{2.6}$$

The corrected fall speed is equal to v_{Stokes} multiplied by C_c.

Figure 2.1a shows the corrected and uncorrected Stokes fall speeds, and the Böhm fall speed, as a function of particle diameter. Figure 2.1b shows the ratio of the Böhm and uncorrected Stokes to the corrected Stokes fall speed. Figure 2.1b shows that for the smallest particles simulated in the model, neglecting the effects of the non-continuum nature of the air leads to fall speeds being underestimated by as much as a factor of 2/3. However, Figure 2.1a shows that fall speeds are generally very small at these sizes, less than 5 mm/s for particles smaller than 10 μm in diameter. For larger particles, the relative error is generally less than about 10%, for both the Böhm and uncorrected Stokes fall speeds.

Figure 2.1 suggests that the errors from using the Böhm fall speed for spherical crystals should be acceptably small. However, since the fall speed corrections for spheroidal particles described in Section 2.1.2 are based on Stokes flow theory, I have replaced the original calculation of fall speeds for spherical particles in the model with one based on Equation 2.5. I have not incorporated the Cunningham shape-correction factor into the model because the errors from ignoring this effect appear to be reasonably small when the fall speeds are non-negligible, and because it is not clear how to properly account for its dependence on the radius when the particle is non-spherical.

2.1.2   *Modification for non-spherical ice crystals*

The dynamic shape factor, here denoted as κ, is the ratio of the fall speed of a spherical particle to that of a spheroidal particle of the same mass. *Fuchs* (1964, pp. 37-40) provides expressions, based on Stokes flow theory, for the dynamic shape factor as a function of the aspect ratio, β, which is the ratio of the spheroid's major axis to its minor axis.
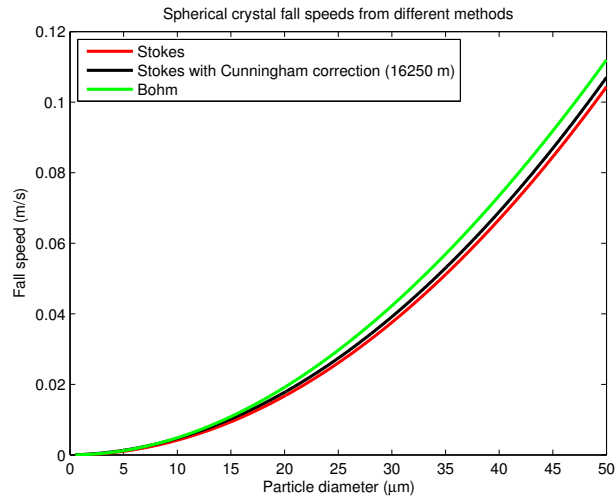
(a)
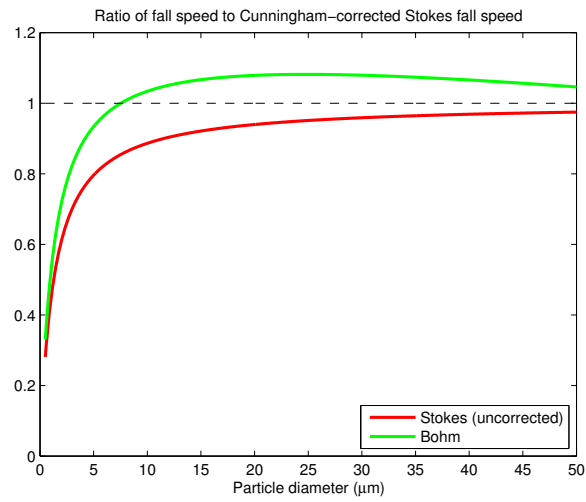
(b)

Figure 2.1: (a) The fall speeds of spherical crystals calculated using Stokes formula (Equation 2.5), Stokes with Cunningham Correction Factor (Equation 2.6), and Böhm formula (Equation 2.1). (b) Ratio of the uncorrected Stokes and Böhm fall speeds to the corrected Stokes fall speed. Assumptions for these plots: altitude = 16 250 m; ice density = 920 kg m^{-3}; air density = 0.162 kg m^{-3}; gravity = 9.8 m s^{-2}; dynamic viscosity of air = 1.2×10^{-5} kg m^{-1} s^{-1}. Smallest diameter plotted is 0.5 μm.

The preferred orientations of falling ice crystals are those which present the largest possible horizontal cross-sectional area. For oblate spheroids, this means that the polar axis (the axis of revolution) is oriented vertically; for prolate spheroids, the polar axis is oriented horizontally. For an oblate spheroid falling along the polar axis, the dynamic shape factor is

$$\kappa = \frac{\frac{4}{3}\left(\beta^{1/3}\right)\left(\beta^2 - 1\right)}{\frac{\beta(\beta^2-2)}{\sqrt{\beta^2-1}}\tan^{-1}\left(\sqrt{\beta^2-1}\right)+\beta} \; . \tag{2.7}$$

For a prolate spheroid falling transverse to the polar axis, the dynamic shape factor is

$$\kappa = \frac{\frac{8}{3}\left(\beta^{-1/3}\right)\left(\beta^2 - 1\right)}{\frac{(2\beta^2-3)}{\sqrt{\beta^2-1}}\ln\left(\beta + \sqrt{\beta^2-1}\right)+\beta} \; . \tag{2.8}$$

Figure 2.2 shows the inverse dynamic shape factor, $1/\kappa$, for oblate and prolate spheroids of various aspect ratios calculated using Equations 2.7 and 2.8, respectively. This is the factor by which the ice crystals' fall speeds are reduced by the non-spherical shape if their mass is held constant. For an aspect ratio of 6, used in the model simulations (see Chapter 4), fall speeds are reduced by about 1/3.

2.2 Ice crystal growth rates

In these simulations, ice crystal nucleation is not being considered (although it was considered by *Dinh et al.* (2012)). Ice crystals are assumed to grow by deposition from the vapor onto pre-existing ice crystals. The simulations are initialized with monodisperse spherical or spheroidal ice crystals, whose initial size, aspect ratio, spatial distribution, and number concentration are specified for each model run.

2.2.1 Spherical ice crystals

I have not made any changes to the calculation of depositional growth rate for spherical crystals, but I still think it is worthwhile to discuss the calculation in detail. This has been previously discussed in the dissertation by *Dinh* (2012), but there were several errors
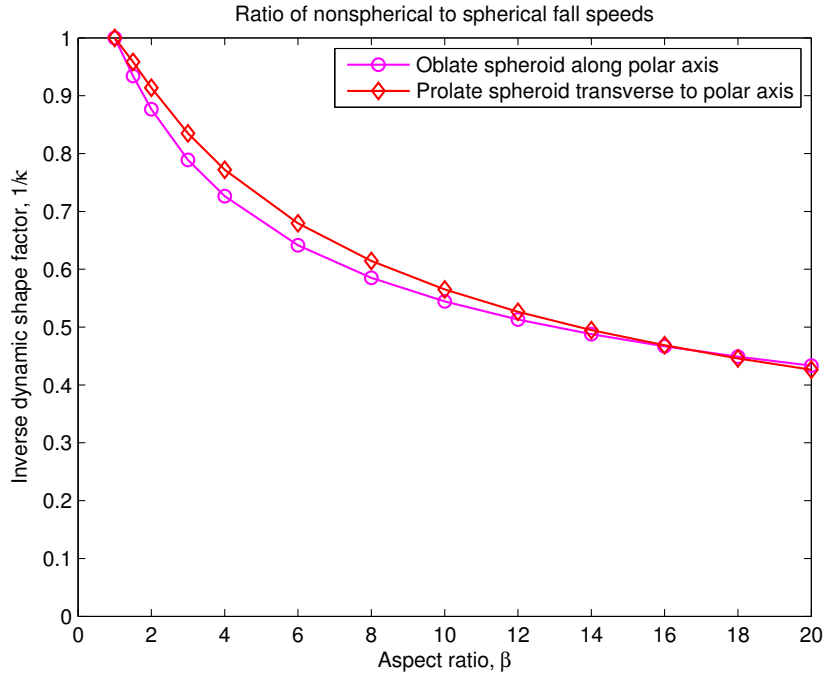
Figure 2.2: Ratios of the fall speeds of spheroidal particles to those of spherical particles of the same mass, based on Equations 2.7 and 2.8 for oblate and prolate spheroids, respectively.

there (noted in footnotes), and it may be helpful for future users of the model to see the equations presented in a format closer to the way they are actually written in the code. Modifications to these calculations for spheroids are discussed in the next subsection.

The depositional growth rate is calculated according to (*Pruppacher and Klett*, 1978, Eq. 13-28):

$$\frac{\mathrm{d}m}{\mathrm{d}t} = \frac{4\pi r \left(S_{\mathrm{ice}} - 1\right)}{\frac{R_v T}{e_{\mathrm{sat,ice}} D'_v} + \frac{L_s}{k'_a T} \left(\frac{L_s}{R_v T} - 1\right)} \tag{2.9}$$

where m is the mass of the ice crystal, r is the ice crystal radius, $e_{\mathrm{sat,ice}}$ is the saturation vapor pressure over a planar ice surface, S_{ice} is the saturation ratio with respect to ice (the ratio of the partial pressure of water vapor to $e_{\mathrm{sat,ice}}$), R_v is the gas constant for water vapor, T is the temperature in degrees Kelvin, D'_v is the modified diffusivity of water vapor in air, k'_a is the modified thermal conductivity of air, and L_s is the latent heat of

sublimation of ice.[4] The process of shifting the new ice mass accumulated during a time step into the appropriate size bin is described in detail in *Dinh and Durran* (2012). Below is a description of how the values of the variables in Equation 2.9 are obtained.

The saturation vapor pressure $e_{\text{sat,ice}}$ is calculated using the Goff-Gratch Equation (*List*, 1984):

$$e_{\text{sat,ice}} = 610.71 \left(\frac{T}{T_r}\right)^{3.56654} \times 10^{\left\{-9.09718\left(\frac{T_r}{T}-1\right)+0.876793\left(1-\frac{T}{T_r}\right)\right\}} \tag{2.10}$$

where T is the temperature in K, $T_r = 273.15$ K, and $e_{\text{sat,ice}}$ is in Pa.

The modified diffusivity and thermal conductivity coefficients are related to the unmodified coefficients by

$$D'_v = D_v f_{v,d} f_{k,d} \tag{2.11}$$

$$k'_a = k_a f_{v,k} f_{k,k} \quad . \tag{2.12}$$

Here, D_v and k_a are the unmodified diffusivity and thermal conductivity coefficients, respectively, $f_{v,d}$ and $f_{v,k}$ represent the effects of ventilation induced by the particle's movement, and $f_{k,d}$ and $f_{k,k}$ represent non-equilibrium behavior at the ice surface. More specifically, $f_{k,d}$ accounts for the the effects of discontinuities in the vapor concentration field near the ice crystal surface and of inefficiency in the incorporation of water molecules into the crystal lattice, while $f_{k,k}$ accounts for discontinuities in the temperature field and inefficiency in obtaining thermal equilibrium at the crystal surface.

The diffusivity coefficient for air is calculated according to (*Pruppacher and Klett*, 1978, Eq. 13-3):

$$D_v = \left(2.11 \times 10^{-5}\right) \frac{p_{\text{ref}}}{p} \left(\frac{T}{T_r}\right)^{1.94} \tag{2.13}$$

---

[4]In *Dinh* (2012), this equation was printed erroneously, but the implementation in the model code was correct.

where p is the ambient air pressure, $p_{\text{ref}} = 1 \times 10^5$ Pa is a reference surface pressure, and T_r is the freezing point of water, 273.15 K.[5] The thermal conductivity of air is calculated using the expression (*Pruppacher and Klett*, 1978, Eq. 13-16):[6]

$$k_a = 2.38 \times 10^{-2} + 7.11 \times 10^{-5} (T - T_r) \; . \tag{2.14}$$

The ventilation coefficients are calculated using empirical expressions given in *Hall and Pruppacher* (1976). The ventilation coefficient for water vapor diffusion is (*Hall and Pruppacher*, 1976, Eq. 16):

$$f_{v,d} = \begin{cases} 1.00 + 0.14 X^2, & \text{if } X < 1.0 \\ 0.86 + 0.28 X^2, & \text{if } X > 1.0 \end{cases} \tag{2.15}$$

where $X = \mathcal{S}^{1/3} \mathcal{R}^{1/2}$, $\mathcal{S}$ is the Schmidt number, assumed equal to 0.63, and $\mathcal{R}$ is the Reynolds number, calculated using Equation 2.3. The ventilation coefficient for thermal conductivity is (*Hall and Pruppacher*, 1976, Eq. 17):

$$f_{v,k} = \begin{cases} 1.00 + 0.14 Y^2, & \text{if } Y < 1.0 \\ 0.86 + 0.28 Y^2, & \text{if } Y > 1.0 \end{cases} \tag{2.16}$$

where $Y = \mathcal{P}^{1/3} \mathcal{R}^{1/2}$, and $\mathcal{P}$ is the Prandtl number, assumed equal to 0.72.

The surface non-equilibrium effects on vapor diffusion are accounted for using (*Pruppacher and Klett*, 1978, Eq. 13-13; *Hall and Pruppacher*, 1976, Eq. 6):

$$f_{k,d} = \frac{1}{\frac{r}{r+\Delta_D} + \frac{D_v f_{v,d}}{r} \left(\frac{2-\beta}{2\beta} \right) \sqrt{\frac{2\pi}{R_v T}}} \tag{2.17}$$

where $\Delta_d = 1 \times 10^{-7}$ m is the water vapor jump length and $\beta = 0.01$ (with considerable uncertainty) is the deposition coefficient for water vapor on ice. The surface non-equilibrium effects on thermal conductivity are accounted for using (*Pruppacher and*

---

[5]In *Dinh* (2012), this equation erroneously omitted the exponent, although it was correctly included in the model, and P_{ref} was listed as 1.013×10^5 Pa rather than 1×10^5 Pa, the value actually used in the model.

[6]The coefficients in *Pruppacher and Klett* are different because they are listed in SI units here but in cgs and calorie units in the book.

Klett, 1978, Eq. 13-20):

$$f_{k,k} = \frac{1}{\frac{r}{r+\Delta_k} + \frac{k_a f_{v,k}}{\rho_{\text{air}} \alpha C_p r} \sqrt{\frac{2\pi}{R_{\text{air}} T}}}$$ (2.18)

where R_{air} is the gas constant for dry air, $C_p = 1004$ J kg^{-1} K^{-1} is the heat capacity of air at constant pressure, $\Delta_k = 2 \times 10^{-7}$ is the thermal jump length, and $\alpha = 1$ is the thermal accommodation coefficient for ice. See *Dinh* (2012, pp. 9-10) for further discussion of Δ_k, Δ_D, α and β.

2.2.2 *Modification for non-spherical ice crystals*

A common technique for calculating the diffusional growth rate of non-spherical ice crystals is to express the effects of their size and shape in a single variable, the capacitance C, which is analogous to the radius of a spherical particle. This is based on an analogy to electrostatics: the relation between the diffusion of vapor to a growing ice crystal and the water vapor distribution surrounding the crystal has the same mathematical form as the relation between the flow of electric charge to a single conducting object to the distribution of electric potential surrounding the object (see *Lamb and Verlinde*, 2011, pp. 343-345). The particle growth rate is obtained by replacing r with C in Equation 2.9 (*Pruppacher and Klett*, 1978, Eq. 13-71):

$$\frac{\text{d}m}{\text{d}t} = \frac{4\pi C (S_{\text{ice}} - 1)}{\frac{R_v T}{e_{\text{sat,ice}} D_v'} + \frac{L_s}{k_a' T} \left(\frac{L_s}{R_v T} - 1 \right)}$$ (2.19)

For a sphere, the capacitance is simply equal to the radius r. For an oblate spheroid, the capacitance is (*Pruppacher and Klett*, 1978, Eq. 13-73):

$$C_{\text{oblate}} = \frac{ae}{\sin^{-1} e}; \quad e = \sqrt{1 - \frac{b^2}{a^2}}$$ (2.20)

where a is the semi-major axis of the ellipse of revolution, b is the semi-minor axis of the ellipse of revolution, and e is the ellipse's eccentricity. For a prolate spheroid, the

capacitance is (*Pruppacher and Klett*, 1978, Eq. 13-74):

$$C_{\text{prolate}} = \frac{A}{\ln\left(\frac{a+A}{b}\right)}; \quad A = \sqrt{a^2 - b^2} \tag{2.21}$$

where A is the ellipse's linear eccentricity.

The existing microphysics scheme defines size bins according to ice crystal mass, and the growth rate is calculated as a mass growth rate. The effect of non-spherical shape on the growth rate is calculated in a subroutine that takes as input arguments the mass m (proportional to volume V) and aspect ratio $\beta = a/b$, then retrieves a and b using the following volume formulae for spheroids:

$$V_{\text{oblate}} = \frac{4}{3}\pi a^2 b \tag{2.22}$$

$$V_{\text{prolate}} = \frac{4}{3}\pi a b^2 \, . \tag{2.23}$$

Then, capacitance is calculated using Equation 2.20 or 2.21, and the growth rate is calculated using Equation 2.19. Since bin masses are used to determine a and b, and since the growth rate is still calculated as a mass growth rate, no changes need to be made to the bin shift procedure described in *Dinh and Durran* (2012).

Besides the capacitance, the ventilation and non-equilibrium coefficients used to define the modified diffusivity and thermal conductivity coefficients D'_v and k'_a also depend on the ice crystal size, and we must consider how to account for the effects of the non-spherical shape here.

The ventilation coefficients $f_{v,d}$ and $f_{v,k}$ (Equations 2.15 and 2.16) depend on the Reynolds number, which is dependent on the particle size. For the purposes of these coefficients, the Reynolds number is calculated using the Böhm formulation (Equation 2.3), for which the Reynolds number is the same for a sphere or spheroid. The actual definition of the Reynolds number, $\mathcal{R} = \rho_{\text{air}} v L / \mu$, suggests that $\mathcal{R}$ should depend on the spheroid's aspect ratio, but since the particle length L increases with aspect ratio while the terminal velocity v decreases, the change should be kept relatively small by compensation between these effects. For now the calculation of the ventilation coefficients

is left unchanged, but it may be useful to run a sensitivity test to constrain the possible effects of the dependence of the ventilation coefficients on the aspect ratio.

The non-equilibrium corrections $f_{k,d}$ and $f_{k,k}$ depend on r in Equations 2.17 and 2.18. *Pruppacher and Klett* (1978) and *Lamb and Verlinde* (2011) do not explicitly state what should replace r in the calculations for spheroids, but I believe it should be the capacitance because the derivation for these coefficients, like the overall growth rate equation, involves an analogy to Maxwell's electromagnetic equations. This is what I have used for the simulations described in Chapter 4. Besides capacitance, the semi-major axis a and the semi-minor axis b are other possibilities, which bracket the range of possible analogues to the radius.

This choice is actually very important to the calculated growth rate. Figure 2.3 shows the ratio of the growth rate for spheroids, calculated using Equation 2.19, to that of the equivalent-mass sphere, as a function of particle size, for the 3 aforementioned measures of particle size in the calculation of $f_{k,d}$ and $f_{k,k}$.[7] If the capacitance is used (which I believe to be correct), the spheroids grow at about 1.5 to 1.6 times the rate of spheres. However, if the semi-major axis is used, the growth rate could be double or even quadruple that for a spherical particle, and if the semi-minor axis is used, the growth rate could be as little as 40% of that for a spherical particle. Given the potential importance of this parameter, future texts on the diffusional growth rate of non-spherical particles should address this issue more explicitly.

This concludes the discussion of the theoretical basis for the changes to the model's growth rate and fall speed calculations. The effects of these changes on the evolution of TTL cirrus are explored in the model simulations described in Chapter 4. The effects of the ice crystals' shape on their radiative properties are examined in Chapter 3.

---

[7]Since the calculated growth rates depend on the temperature and pressure, I have chosen reasonable values for the TTL: $T = 190$ K, $p = 135$ hPa.
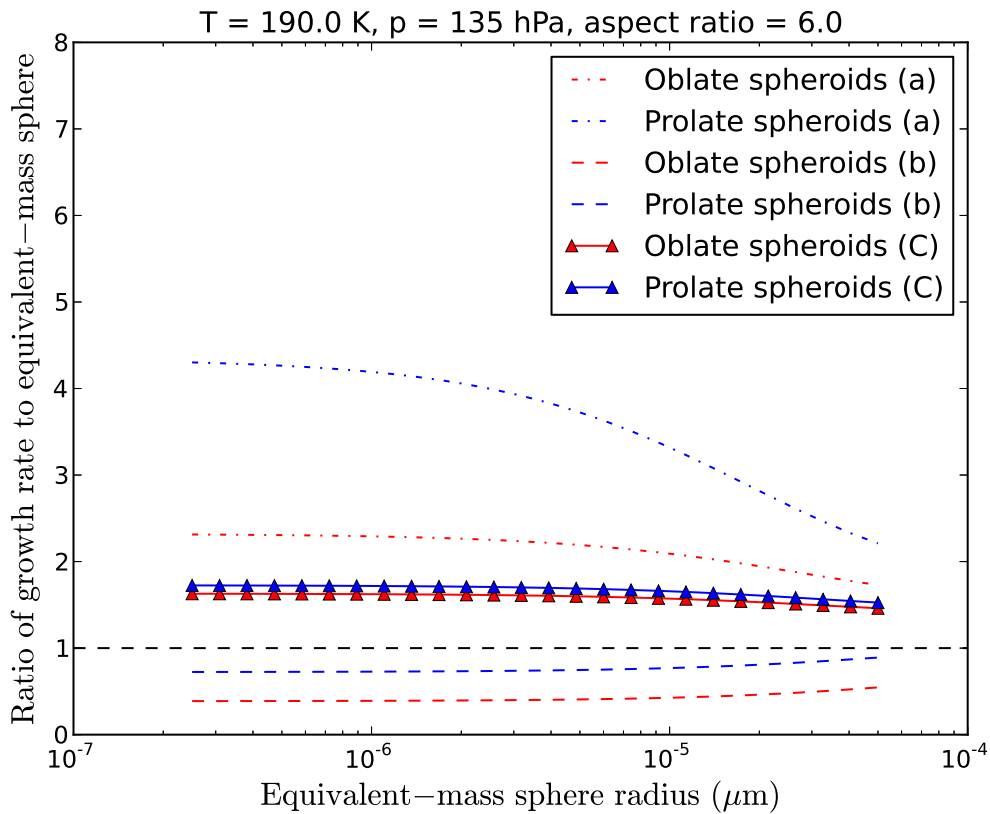
Figure 2.3: Ratios of mass growth rates for oblate (red) and prolate (blue) spheroids with aspect ratios of 6 to those for the equivalent-mass sphere, as a function of particle size. Assuming a temperature of 190 K and a pressure of 135 hPa. Three versions are plotted, depending on whether the measure of particle size used in the calculations of $f_{k,d}$ and $f_{k,k}$ is the capacitance (C, solid lines), semi-major axis (a, dot-dash lines), or semi-minor axis (b, dashed lines).

Chapter 3

IMPROVEMENTS TO MODEL RADIATION

In the cirrus radiation scheme developed by Dr. Tra Dinh for the System for Atmospheric Modeling (SAM) cloud resolving model, the radiative effects of ice crystals are calculated according to a lookup table of broadband shortwave (SW) and longwave (LW) absorption cross sections as functions of ice crystal size. This is intended to save computational expense relative to calculating fluxes at multiple wavelengths. In order to generate this lookup table, a one-dimensional, multiple-scattering, spectrally-resolved radiative transfer model is used to calculate the radiative heating rate in a cloud layer containing ice crystals of a particular size. Then, the SAM radiation scheme is inverted to calculate the broadband absorption cross section such that SAM would calculate the same radiative heating rate as the radiative transfer model, for a single cloud layer.

Now that we are considering non-spherical ice crystals in SAM, it is necessary to investigate the effects of ice crystals' shape on their radiative properties. In the course of doing this analysis I have recreated Dr. Dinh's original lookup table for spherical particles using somewhat different methods, and obtained similar results. Dr. Dinh's methods are described in her theses (*Dinh*, 2009, Section 3.1.1; *Dinh*, 2012, Section 2.2). I have also described these methods below in Section 3.1, and I have included additional details that have not been previously published in a thesis or paper. My reproduction of this work for spherical crystals is described in Section 3.2. The extension to non-spherical crystals is described in Section 3.3.

3.1 Original calculations for spheres

The radiative transfer model used to generate the original absorption cross section table is known as Rapid Calculation of Radiative Heating Rates (RAPRAD). In this code, absorption is calculated using the k-distribution method. The longwave absorption calculation is based on the method described in *Mlawer et al.* (1997), and the shortwave absorption calculation is based on *Kato et al.* (1999). Scattering is calculated using the two-stream algorithm described in *Toon et al.* (1989).[1]

For a cirrus cloud layer, RAPRAD requires the specification of the altitudes of the top and bottom of the cloud layer, the number concentration of ice crystals, and a phase function file containing the ice crystals' single scattering properties (asymmetry factor, extinction cross section, and absorption cross sections)[2] in each of the wavelength bands for the k-distribution binning.The choice of the phase function file determines the ice crystal size via these properties. The phase function files were generated using the Mie scattering code for spherical particles developed by *Toon and Ackerman* (1981). This code requires as input the real and imaginary index of refraction of ice, known as the "ice optical constants" despite their wavelength dependence. The ice optical constants were obtained from Table 1 of *Warren* (1984). A revised compilation of ice optical constants was made by *Warren and Brandt* (2008); the effects of these revisions on the calculated broadband ice properties are discussed in Section 3.2.

RAPRAD was run for 500 m vertical resolution, with the cloud layer between 16 000 and 16 500 m.[3] The cloud number concentration was set so that the LW optical depth would be approximately 0.005. For small optical depths, the calculated ice crystal ab-

---

[1] For the shortwave, the option also exists to use the 4-stream algorithm described in *Liou et al.* (1988) instead, but neither Dr. Dinh nor I have used this option.

[2] The phase function files also contain the single-scattering albedo and scattering cross section, which are redundant with these properties, and moments 0 through 4 of the phase function, which are used only in the 4-stream version of the code.

[3] Tra Dinh tried 250 m resolution, still with a 500 m thick cloud, and got results that were not significantly different from those obtained using one cloud layer.

sorption cross section should not depend on the cloud optical depth, so the calculation was redone with LW optical depths of 0.05 and 0.0005 (still plausible values for actual thin cirrus) to confirm that the calculated absorption cross section remained the same to within about 5%. Temperature, H_2O, and O_3 profiles were specified based on a March climatological average for the Galápagos Islands, an equatorial site with a cold tropical tropopause. These were the profiles used by *Gettelman et al.* (2004) in a study of the radiative balance of the tropical tropopause layer. The CO_2 concentration was set to 355 ppmv.[4]

The radiation scheme used in SAM is much simpler than RAPRAD, involving only broadband LW and SW fluxes. The broadband ice crystal absorption cross sections used in SAM are determined from the RAPRAD results by inverting the SAM radiation scheme so that the radiative heating rate calculated by SAM for a single cloudy model layer would match that calculated by RAPRAD. Assuming a constant heat capacity, this radiative heating rate can be expressed in terms of the flux convergence, FC, defined as:

$$FC = F_{\text{bot}}^{\uparrow} + F_{\text{top}}^{\downarrow} - F_{\text{bot}}^{\downarrow} - F_{\text{top}}^{\uparrow} \tag{3.1}$$

where $F_{\text{bot}}^{\uparrow}$ is the upwelling radiative flux at the bottom of the cloud, $F_{\text{top}}^{\downarrow}$ is the downwelling flux at the top of the cloud, $F_{\text{bot}}^{\downarrow}$ is the downwelling flux at the bottom of the cloud, and $F_{\text{top}}^{\uparrow}$ is the upwelling flux at the top of the cloud. The values of $F_{\text{bot}}^{\uparrow}$, $F_{\text{top}}^{\downarrow}$, $F_{\text{bot}}^{\downarrow}$, and $F_{\text{top}}^{\uparrow}$ in the shortwave and longwave are output by RAPRAD. $F_{\text{bot}}^{\uparrow}$ and $F_{\text{top}}^{\downarrow}$ are boundary conditions that do not depend on the cloud properties, while $F_{\text{bot}}^{\downarrow}$ and $F_{\text{top}}^{\uparrow}$ do depend on the cloud properties. Note that while SAM ignores absorption and emission by gases, RAPRAD includes it, so for RAPRAD, the flux convergence from a clear-sky case must be subtracted out in order to isolate the effect of the cloud. The parameterized broadband absorption cross section can be obtained from FC, $F_{\text{bot}}^{\uparrow}$, and $F_{\text{top}}^{\downarrow}$, using expressions derived below.

While RAPRAD considers scattering, the SAM radiative transfer scheme includes only

---

[4]This value was hard-coded in RAPRAD. It should not affect the calculated ice crystal properties.

absorption and emission. In SAM, the fluxes exiting a cloud layer are calculated according to:

$$F_{\text{top}}^{\uparrow} = F_{\text{bot}}^{\uparrow} t + (1 - t)B \tag{3.2}$$

$$F_{\text{bot}}^{\downarrow} = F_{\text{top}}^{\downarrow} t + (1 - t)B . \tag{3.3}$$

where t is the cloud layer transmissivity and $B = \sigma T^4$, where σ is the Stefan-Boltzmann constant and T is the temperature.[5] The first term in these expressions represents attenuation due to absorption. The second term represents blackbody emission, where B is the flux density of radiation emitted by a perfect blackbody, and $(1 - t)$ is the emissivity, which is equal to the absorptivity by Kirchhoff's law.[6]

By substituting Equations 3.2 and 3.3 into Equation 3.1 and rearranging, we can obtain an expression for the transmissivity of the layer in terms of the flux convergence and flux boundary conditions:

$$t = 1 - \frac{FC}{F_{\text{bot}}^{\uparrow} + F_{\text{top}}^{\downarrow} - 2B} \tag{3.4}$$

The transmissivity of the layer is related to the absorption cross section via the layer's optical depth. For vertically incident radiation, the optical depth is

$$\tau = \sigma_{\text{abs}} N \Delta z \tag{3.5}$$

where σ_{abs} is the ice crystal absorption cross section, N is the ice crystal number concentration, and Δz is the thickness of the cloud layer. The transmissivity of the layer is calculated in SAM according to

$$t = e^{-\tau/\overline{\mu}} \tag{3.6}$$

---

[5]Note that SAM includes multiple model layers and does this calculation for each layer that contains cloud ice, whereas RAPRAD is run with only one cloud layer. Tests with two adjacent cloud layers in RAPRAD did not significantly affect the parameterized absorption cross sections.

[6]Note that in reality the blackbody emission in the shortwave at atmospheric temperatures is negligible, so the emission term should arguably be neglected for the shortwave. However, for consistency, if this term is included in SAM then it should also be included when calculating the parameterized SW absorption cross section.

where $\overline{\mu} = 1/2$ is the cosine of the effective zenith angle (*Petty*, 2006, p. 214).[7] Therefore, the parameterized broadband absorption cross section is found using:

$$\sigma_{\text{abs}} = \frac{-\ln(t)}{2N\Delta z} \,, \tag{3.7}$$

where t is calculated using Equation 3.4 based on the fluxes calculated by RAPRAD.

Figure 3.1 summarizes the information flow from ice optical constants to broadband absorption cross sections. The broadband absorption cross sections calculated by Tra Dinh using this method are shown in Table 3.1.

3.2 Revised calculations for spheres

In the process of developing the methods for calculating the radiative properties of non-spherical particles, I have made several changes to the calculations for spherical particles in the longwave. These changes were made largely for methodological consistency with the non-spherical cases and are not meant to imply that the absorption cross sections listed in Table 3.1 are incorrect. These changes are described below.

The shortwave is responsible for only about 10% of the radiative absorption in thin cirrus, so small changes to the shortwave absorption cross sections would have a negligible effect on the overall radiative heating. Therefore, I have not attempted to recalculate the shortwave absorption cross sections for spherical or non-spherical crystals. See Appendix B for more on the relative importance of SW and LW heating in thin cirrus.

3.2.1 T-Matrix code

The *Toon and Ackerman* (1981) Mie scattering code does not allow for shapes other than spheres. Because of this limitation, I switched to a different code, which is based on the T-Matrix method for numerically solving Maxwell's equations, in order to compute

---

[7]The SAM radiative transfer scheme assumes a plane-parallel atmosphere but the cloud-resolving model is 2-dimensional; the effective zenith angle accounts for multiple angles of incidence and emission.
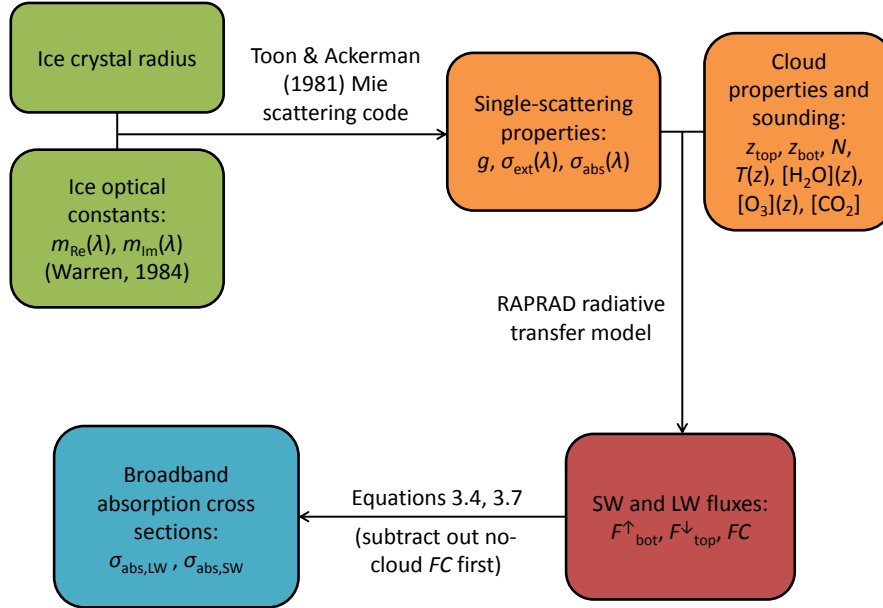
Figure 3.1: Summary of procedure for generating ice crystal absorption cross section lookup table for spheres, following Tra Dinh's methodology. m_{Re} = real index of refraction; m_{Im} = imaginary index of refraction; λ = wavelength; g = asymmetry factor; σ_{ext} = extinction cross section σ_{abs} = absorption cross section; z = altitude; N = number concentration of ice crystals; T = temperature; [] denotes chemical concentration; $F^{\uparrow}_{bot}$ = upward flux at bottom of cloud; $F^{\downarrow}_{top}$ = downward flux at top of cloud; FC = flux convergence in cloud.

the single-scattering properties of ice. This code is described in *Mishchenko and Travis* (1998). It is applicable to rotationally symmetric particles, including spheroids, circular cylinders, and Chebyshev particles. I have used the spheroid case, including the special case of a spherical particle.

Inputs to the T-Matrix code include the wavelength of light; the real and imaginary optical constants of bulk ice at that wavelength; the ice crystal size, expressed in terms of the radius of the equivalent-volume sphere; the aspect ratio of the particles; and the size distribution of particles, although I have only run monodisperse cases. Outputs include the extinction and scattering cross sections, the asymmetry parameter, and the

r (μm)	$\sigma_{\mathrm{abs,LW}}$ (m^2)	$\sigma_{\mathrm{abs,SW}}$ (m^2)
1.0	6.5×10^{-13}	1.0×10^{-14}
2.2	6.6×10^{-12}	1.0×10^{-13}
3.4	2.2×10^{-11}	3.0×10^{-13}
4.6	4.7×10^{-11}	6.1×10^{-13}
5.8	8.2×10^{-11}	1.0×10^{-12}
7.0	1.3×10^{-10}	1.5×10^{-12}
8.2	1.8×10^{-10}	2.2×10^{-12}
9.4	2.5×10^{-10}	3.0×10^{-12}
10.6	3.3×10^{-10}	4.1×10^{-12}
11.8	4.1×10^{-10}	5.4×10^{-12}
13.0	5.1×10^{-10}	6.4×10^{-12}
15.5	7.4×10^{-10}	1.0×10^{-11}
22.9	1.6×10^{-9}	2.6×10^{-11}
33.8	3.5×10^{-9}	6.8×10^{-11}
50.0	7.5×10^{-9}	1.8×10^{-10}

Table 3.1: Look up table of longwave and shortwave absorption cross sections used in SAM for spherical ice crystals. These values were calculated by Tra Dinh using the procedure described in Section 3.1.

moments of the phase function.[8]

Comparisons of the T-Matrix output to the RAPRAD phase function files used by Tra Dinh showed that the results of the two scattering codes matched to within 1% (and usually much better) in the longwave for the 15 spherical particle sizes in the lookup table. For the shortwave, however, a limitation was reached for particles with radii greater than

---

[8]The variable names for the output are listed in *Mishchenko and Travis* (1998).

9.6 μm: the code does not converge because the size parameter, $2\pi r/\lambda$, gets too large for the shortest wavelengths included in the radiative transfer model.[9]

3.2.2 RRTM

Because it is simpler to use and runs faster than RAPRAD, I have been using a different multiple-scattering radiative transfer model, known as the Rapid Radiative Transfer Model, or RRTM.[10] RRTM was created by the firm Atmospheric and Environmental Research and is available to download at <http://rtweb.aer.com/rrtm_frame.html>. There are two versions of RRTM. One is intended for use in global climate models (GCMs), but since it does not account for scattering in the longwave, I have used the other, standalone version. In RRTM, as in RAPRAD, the absorption calculation is based on *Mlawer et al.* (1997), with changes to two of the band boundaries. Scattering is calculated using a code, known as DISORT, that implements the discrete-ordinates method. DISORT is described in the paper by *Stamnes et al.* (1988), and a much more detailed discussion is given in the NASA technical report by *Stamnes et al.* (2000).[11] DISORT can be run in 4, 8, or 16 streams in RRTM; I have used the 4-stream version.

RRTM input is provided in 2 files: INPUT_RRTM and IN_CLD_RRTM. The INPUT_RRTM file specifies the temperature profile and vertical resolution. It also specifies the volume mixing ratios of absorbing gases including H_2O, CO_2, O_3, N_2O, CO, CH_4, and O_2, as well as the layer concentration of "broadening" (non-absorbing) gases, i.e. N_2 and Ar, in cm^{-2}. I ran RRTM for the same vertical grid as RAPRAD (0-45 km, 500 m resolution)

---

[9]An extended precision version of the code exists but attempting to use it did not solve this problem.

[10]Originally I started using RRTM because I could not reproduce Tra Dinh's original absorption cross sections with RAPRAD, which I thought was due to code maintenance issues in RAPRAD but was actually because I was not subtracting out the clear-sky flux convergence before calculating the absorption by the ice crystals. RAPRAD is slower to run than RRTM largely because RAPRAD needs to be recompiled every time the properties of the ice crystals are changed, although it could probably be re-engineered to fix this problem.

[11]Another documentation file, focused on the code itself, is also available at <ftp://climate1.gsfc.nasa.gov/ridgway/Multiple_Scatt/DISORT2.0beta/DISORT.doc>.

and with temperature, H_2O, and O_3 concentrations taken from the Galapagos sounding (*Gettelman et al.*, 2004) used for RAPRAD. For the remaining greenhouse gases, I used the values from the clear-sky tropical test case included with the RRTM code, interpolated to the 500 m grid.[12] The broadening gas concentration was calculated according to the ideal gas law and the pressure, temperature, and depth of the layer.[13]

The IN_CLD_RRTM file contains information about the cloud location and properties. These properties include the extinction optical depth of the cloud layer, the single-scattering albedo, and moments 0 through 4 of the phase function, in each of the 16 RRTM longwave bands. I obtained these properties by running the T-Matrix code at the midpoints of these 16 bands in wavenumber space.[14] The extinction optical depth is calculated by multiplying the extinction cross sections obtained from the T-Matrix code by the layer thickness and the number concentration of cloud particles.[15] Note that the phase function moments output by the T-Matrix code must be normalized for RRTM by dividing the nth moment by $(2n+1)$.[16]

Like RAPRAD, RRTM outputs the upwelling and downwelling fluxes at the top and bottom of the cloud which can be used to calculate the broadband absorption cross sections using Equations 3.4 and 3.7. The absorption cross sections calculated using this

---

[12]The CO_2 concentration in this case is nearly constant at about 355 ppmv.

[13]Originally I had interpolated the broadening gas densities from the test case to the 500 m grid, but that was incorrect as this quantity depends on the layer thickness. This led to the clear-sky radiative fluxes being much different between RAPRAD and RRTM; after fixing this problem, the clear-sky agreement between the models was much better.

[14]The band properties are specified in order of increasing wavenumber, the opposite order from RAPRAD. Specifying these properties in reverse order originally led me to think that the two models were producing vastly different results.

[15]I have written a Python script to generate the IN_CLD_RRTM file based on this information and the T-Matrix output; this way the T-Matrix code only needs to be run once for multiple cloud configurations with the same ice crystal size.

[16]The moments of the phase function are the coefficients of Legendre polynomials into which the phase function has been expanded. Their precise definition differs between the T-Matrix and DISORT codes. In the output to the T-matrix code, these phase function moments are given as the vector ALPH1. To see that this is the correct normalization, see the definition of PMOM in the DISORT.doc file at <ftp://climate1.gsfc.nasa.gov/ridgway/Multiple_Scatt/DISORT2.0beta/DISORT.doc>).

method for the optical constants of ice listed in *Warren* (1984) are shown in the "RRTM (old optical constants)" column of Table 3.2. The results from RRTM match those from RAPRAD to within about 6%. The differences between the results from the two radiative transfer models are likely due to the choice of wavelengths within the bands at which to run the Mie scattering code. Appendix A explores this choice as a potential source of uncertainty.
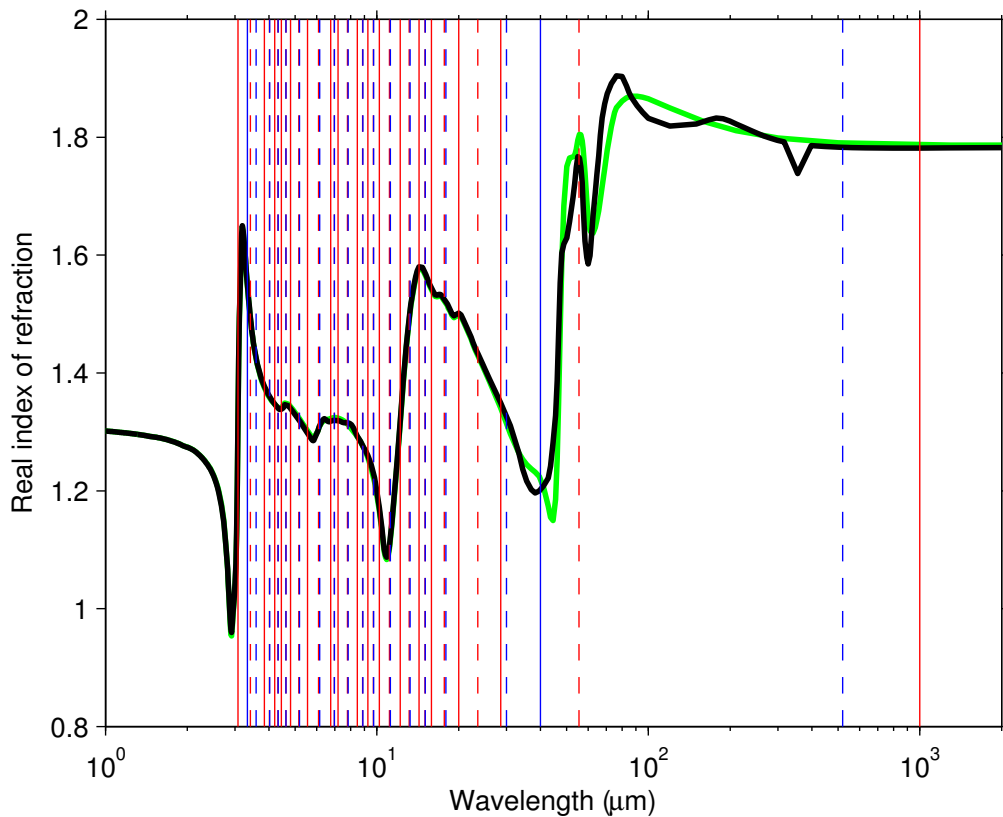
Figure 3.2: Real index of refraction of ice from *Warren* (1984) (green) and *Warren and Brandt* (2008) (black) as a function of wavelength in the longwave. RRTM band boundaries shown as red, solid, vertical lines; RAPRAD band boundaries, where they differ, shown in blue. (The only differences are for the lower bound of the shortest-wavelength bin and the boundary between the second-longest-wavelength and longest-wavelength bin). Midpoints of the RAPRAD bins in wavelength space shown as blue dashed lines; midpoints of the RRTM bins in wavenumber space shown as red dashed lines.

3.2.3 Updated optical constants of ice

The ice optical constants compiled by *Warren* (1984) have been updated by *Warren and Brandt* (2008) in order to incorporate the intervening 24 years of ice physics research. Figures 3.2 and 3.3 compare the real and imaginary indices of refraction, respectively, from these two papers across the LW wavelength ranges considered by RAPRAD and RRTM.
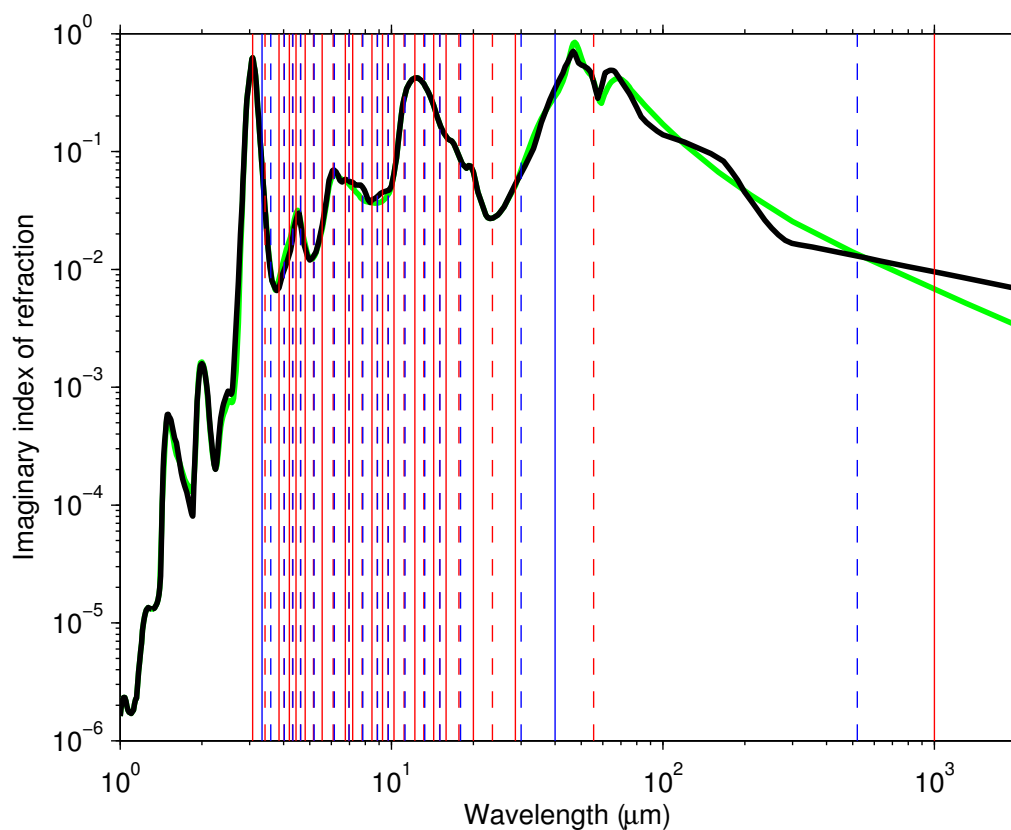
Figure 3.3: Same as figure 3.2 but for the imaginary index of refraction of ice.

Because there were some updates to the optical constants within the LW wavelength range of RRTM, I have recalculated the LW absorption cross sections for spheres using the new optical constants, again using RRTM as the radiative transfer model. Table 3.2

compares these results, the results from the old optical constants, and Tra Dinh's original table. The changes in the optical constants for RRTM cause a change in the parameterized absorption cross section of at most about 3.5%.

r (μm)	RAPRAD	RRTM (old optical constants)	RRTM (new optical constants)
1.0	6.50×10^{-13}	6.79×10^{-13}	6.65×10^{-13}
2.2	6.60×10^{-12}	6.99×10^{-12}	6.81×10^{-12}
3.4	2.20×10^{-11}	2.29×10^{-12}	2.23×10^{-12}
4.6	4.70×10^{-11}	4.91×10^{-11}	4.76×10^{-11}
5.8	8.20×10^{-11}	8.49×10^{-11}	8.22×10^{-11}
7.0	1.30×10^{-10}	1.31×10^{-10}	1.27×10^{-10}
8.2	1.80×10^{-10}	1.85×10^{-10}	1.79×10^{-10}
9.4	2.50×10^{-10}	2.50×10^{-10}	2.42×10^{-10}
10.6	3.30×10^{-10}	3.21×10^{-10}	3.10×10^{-10}
11.8	4.10×10^{-10}	4.04×10^{-10}	3.91×10^{-10}
13.0	5.10×10^{-10}	4.94×10^{-10}	4.79×10^{-10}
15.5	7.40×10^{-10}	7.18×10^{-10}	7.00×10^{-10}
22.9	1.60×10^{-9}	1.59×10^{-9}	1.56×10^{-9}
33.8	3.50×10^{-9}	3.41×10^{-9}	3.39×10^{-9}
50.0	7.50×10^{-9}	7.33×10^{-9}	7.32×10^{-9}

Table 3.2: Parameterized LW absorption cross sections, in m^2, from RAPRAD (values used in *Dinh et al.* (2012)), and from RRTM with old (*Warren*, 1984) and new (*Warren and Brandt*, 2008) optical constants of ice.

Figures 3.2 and 3.3 show that the imaginary index of refraction, in particular, varies over as much as several orders of magnitude *within* the RRTM bands, suggesting that the possible error associated with the precise choice of wavelength is larger than the effect
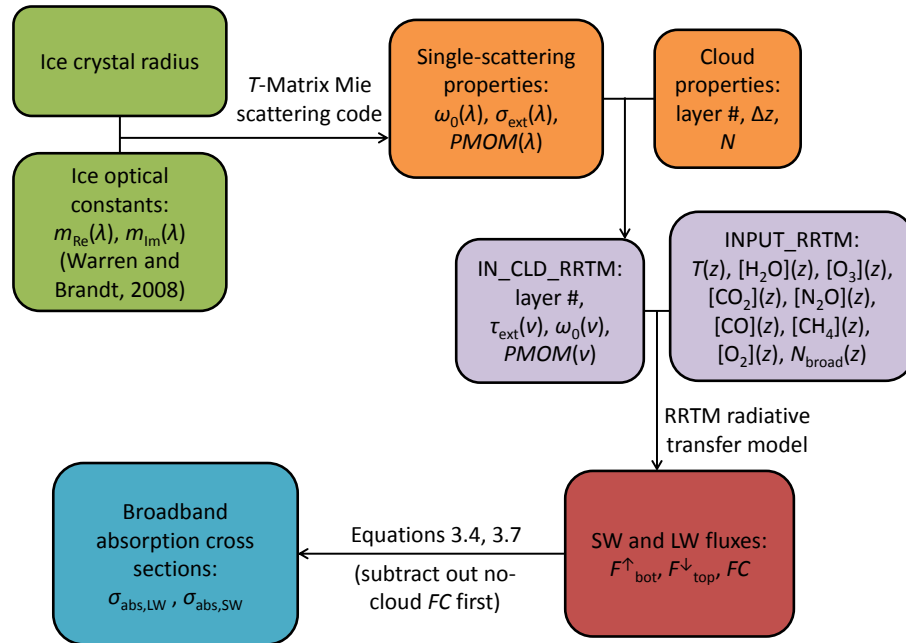
Figure 3.4: Information flow for the radiation parameterization, for my revised methodology, for spheres. This is the method used to generate the "RRTM (new optical constants)" case in Table 3.2. m = index of refraction; λ = wavelength; ω_0 = single-scattering albedo; σ_{ext} = extinction cross section; $PMOM$ = moments of phase function; z = altitude; layer # = position of cloud; Δz = cloud layer thickness; N = number concentration of ice crystals; T = temperature; [] denotes chemical concentration; N_{broad} = concentration of broadening gases; $F^{\uparrow}_{\mathrm{bot}}$ = upward flux at bottom of cloud; $F^{\downarrow}_{\mathrm{top}}$ = downward flux at top of cloud; FC = flux convergence in cloud.

of the *Warren and Brandt* (2008) updates to the ice optical constants. This may in fact be the reason for the differences between the "RAPRAD" and "RRTM (old optical constants)" case shown in Table 3.2, because the Mie scattering codes were run at different wavelengths for the two models.[17] To explore this possible source of error, Appendix A includes some sensitivity tests to the choice of optical constants within the bands, with the "RRTM (new optical constants)" case shown in Table 3.2 used as the control case.

---

[17]Running the two codes with single-scattering properties calculated at the same wavelengths for all bands would pose its own problems, because the band boundaries are not the same.

These tests suggest that the uncertainty caused by the choice of wavelengths within the bands is larger than the differences between RAPRAD and RRTM or those caused by the updates to the ice optical constants.

Figure 3.4 is an analogue to Figure 3.1 for my updated methods for spheres, i.e. the methods used to create the "RRTM (new optical constants)" numbers shown in Table 3.2. Hereafter, I will be using these numbers for the LW absorption cross sections for spheres, rather than the ones used by Dr. Dinh. This is not to suggest that the original numbers were incorrect, but is rather being done for consistency with the methods used for non-spherical ice crystals, which are described in the next section.

3.3 *Extension to non-spherical ice crystals*

I had originally planned to use the T-Matrix code to directly calculate the radiative properties of prolate and oblate spheroids of ice, with volumes equal to those of spheres with the radii listed in Table 3.2. However, when I tried to do this for oblate spheroids with an aspect ratio of 6, it only worked for the three smallest sizes in the table. For larger sizes, the T-Matrix code failed to converge. For prolate spheroids, the problem was even worse, with convergence obtained only for the smallest mass in the table. Therefore, instead of spheroids, I have chosen a different representation of columns and plates for the radiation parameterization.

3.3.1 *Equal-V/A spheres method*

This method involves representing a cloud of nonspherical ice crystals using spheres with the same surface area to volume ratio (referred to as "equal-V/A spheres" hereafter for brevity), with the number concentration adjusted to conserve mass. The accuracy of this method for the calculation of upward and downward fluxes of radiation in multiple-scattering radiative transfer models was first demonstrated by *Grenfell and Warren* (1999), who considered the case of cylindrical ice crystals. *Neshyba et al.* (2003) extended this method to solid, hexagonal plates and columns, and *Grenfell et al.* (2005)

further extended it to hollow columns and plates. The rationale for this method is that the scattering caused by a cloud layer depends mainly on the total ice crystal surface area, the absorption depends mainly on the total volume of ice, and the number concentration of ice crystals (at constant total mass) is not very important for the radiative fluxes.[18]

In order to obtain the best possible approximation of realistic ice crystals, I have used the equal-V/A spheres method for hexagonal columns and plates, following *Neshyba et al.* (2003). For consistency with the aspect ratios for spheroids I have used an aspect ratio of 6 for the columns and 1/6 for the plates, where the aspect ratio is here defined as (*Neshyba et al.*, 2003, Eq. 5):

$$\Gamma \equiv \frac{c}{2a} \tag{3.8}$$

where c is the length of the column or thickness of the plate, and a is the distance along the hexagonal face from the center to one of the vertices.[19] The volume of a hexagonal prism is given by (*Neshyba et al.*, 2003, Eq. 6c):

$$V = 3\sqrt{3}a^3\Gamma . \tag{3.9}$$

The radius of the sphere whose ratio of volume to surface area matches that of the hexagonal column or plate (the "equal-V/A sphere") is (*Neshyba et al.*, 2003, Eq. 6a):

$$r_{VA} = \frac{3\sqrt{3}a\Gamma}{4\Gamma + \sqrt{3}} . \tag{3.10}$$

It is sometimes convenient to express sizes of the columns and plates in terms of the radius, r_V, of the equivalent-volume sphere, even though this is not the actual sphere being used in the model. A useful expression can be derived for the ratio of r_{VA} to r_V in

---

[18]Unlike for angle-integrated fluxes, the equal-V/A spheres method would not be accurate for angle-dependent intensities, but those are not important for our purposes.

[19]This is a slightly different definition from the aspect ratio for spheroids, so the consistency is not perfect.

terms of only the aspect ratio Γ:[20]

$$\frac{r_{VA}}{r_V} = \left(\frac{3\sqrt{3}\Gamma}{4\Gamma + \sqrt{3}}\right)\left(\frac{4\pi}{9\sqrt{3}\Gamma}\right)^{1/3} . \tag{3.11}$$

To conserve the total ice mass in the cloud layer, the ice crystal number concentration should be multiplied by (*Neshyba et al.*, 2003, Eq. 6b)

$$\frac{N_s}{N} = \frac{\left(4\Gamma + \sqrt{3}\right)^3}{36\pi\Gamma^2} , \tag{3.12}$$

where N_s is the number concentration of equal-V/A spheres and N is the number concentration of columns or plates.

For $\Gamma = 6$ (columns), $r_{VA}/r_V = 0.6206$ and $N_s/N = 4.1847$. For $\Gamma = 1/6$ (plates), $r_{VA}/r_V = 0.6106$ and $N_s/N = 4.3933$. Table 3.3 shows the values of r_{VA} for colums and plates with Γ of 6 and 1/6, respectively, associated with each of the ice crystal masses (expressed in terms of r_V) in the original absorption cross section lookup table. It also shows N, the number concentration used in the original parameterization for spheres, and N_s, the number concentration of equal-V/A spheres such that the cloud mass remains the same. To generate absorption cross sections for columns and plates, the T-Matrix code was run for spheres with the radii r_{VA} given in Table 3.3, and then RRTM was run with a number concentration N_s of these spheres. In the last step of the parameterization (Equation 3.7), N was used instead of N_s so that the absorption would be attributed to the correct number of non-spherical ice crystals.

3.3.2   Results

The LW absorption cross sections generated using the equal-V/A spheres method to represent hexagonal plates and columns are shown in Table 3.4, under columns labeled "Plate (multi-sphere)" and "Column (multi-sphere)". Comparing these columns to the "Sphere" column (which is the same as the "RRTM (new optical constants)" case from

---

[20]To derive this expression, first eliminate a from Equations 3.9 and 3.10 to express r_{VA} in terms of Γ and V. Then, substitute $\frac{4}{3}\pi r_V^3$, the volume of a sphere of radius r_V, for V.

r_V	r_{VA} (columns)	r_{VA} (plates)	N	N_s (columns)	N_s (plates)
(μm)	(μm)	(μm)	(m^{-3})	(m^{-3})	(m^{-3})
1.0	0.621	0.611	1.5×10^7	6.277×10^7	6.590×10^7
2.2	1.365	1.343	1.5×10^6	6.277×10^6	6.590×10^6
3.4	2.110	2.076	4.5×10^5	1.883×10^6	1.977×10^6
4.6	2.855	2.809	2.1×10^5	8.788×10^5	9.226×10^5
5.8	3.599	3.541	1.2×10^5	5.022×10^5	5.272×10^5
7.0	4.344	4.274	7.6×10^4	3.180×10^5	3.339×10^5
8.2	5.089	5.007	5.5×10^4	2.302×10^5	2.416×10^5
9.4	5.833	5.739	4.0×10^4	1.674×10^5	1.757×10^5
10.6	6.578	6.472	3.0×10^4	1.255×10^5	1.318×10^5
11.8	7.322	7.205	2.4×10^4	1.004×10^5	1.054×10^5
13.0	8.067	7.937	1.9×10^4	7.951×10^4	8.347×10^4
15.5	9.619	9.464	1.3×10^4	5.440×10^4	5.711×10^4
22.9	14.211	13.982	6.1×10^3	2.553×10^4	2.680×10^4
33.8	20.975	20.637	2.8×10^3	1.172×10^4	1.230×10^4
50.0	31.028	30.529	1.3×10^3	5.440×10^3	5.711×10^3

Table 3.3: Parameters for radiative transfer model runs representing hexagonal columns and plates, with aspect ratios of 6 and 1/6, respectively, as collections of equal-V/A spheres (*Neshyba et al.*, 2003). r_V = radius of equal-volume sphere (measure of ice crystal mass). r_{VA} = radius of equal-V/A sphere. N = number concentration of columnar or plate crystals. N_s = number concentration of equal-V/A spheres that conserves total ice mass in the cloud layer.

Table 3.4) shows that the effect of non-spherical shape on the parameterized LW absorption cross sections is minimal for the smallest crystals, but amounts to a factor of about 1.6 for the largest crystals. Generally, non-spherical crystals have greater absorption cross sections than their equivalent-mass spherical counterparts, except for the smallest

size listed in the table. The differences between the columns and plates are very small, because the surface area to volume ratios are very similar for aspect ratios of 6 and 1/6.

r_V (μm)	Sphere	Plate (multi-sphere)	Column (multi-sphere)	Oblate (direct)	Prolate (direct)	Oblate (multi-sphere)	Prolate (multi-sphere)
1.0	6.65×10^{-13}	6.51×10^{-13}	6.51×10^{-13}	6.86×10^{-13}	6.69×10^{-13}	6.47×10^{-13}	6.52×10^{-13}
2.2	6.81×10^{-12}	7.12×10^{-12}	7.12×10^{-12}	6.94×10^{-12}		7.13×10^{-12}	7.10×10^{-12}
3.4	2.23×10^{-12}	2.54×10^{-11}	2.53×10^{-11}	2.29×10^{-11}		2.57×10^{-11}	2.48×10^{-11}
4.6	4.76×10^{-11}	5.88×10^{-11}	5.85×10^{-11}			5.99×10^{-11}	5.65×10^{-11}
5.8	8.22×10^{-11}	1.08×10^{-10}	1.08×10^{-10}			1.12×10^{-10}	1.02×10^{-10}
7.0	1.27×10^{-10}	1.74×10^{-10}	1.73×10^{-10}			1.81×10^{-10}	1.63×10^{-10}
8.2	1.79×10^{-10}	2.56×10^{-10}	2.54×10^{-10}			2.68×10^{-10}	2.36×10^{-10}
9.4	2.42×10^{-10}	3.52×10^{-10}	3.48×10^{-10}			3.71×10^{-10}	3.22×10^{-10}
10.6	3.10×10^{-10}	4.64×10^{-10}	4.59×10^{-10}			4.93×10^{-10}	4.24×10^{-10}
11.8	3.91×10^{-10}	5.93×10^{-10}	5.85×10^{-10}			6.27×10^{-10}	5.36×10^{-10}
13.0	4.79×10^{-10}	7.34×10^{-10}	7.24×10^{-10}			7.79×10^{-10}	6.62×10^{-10}
15.5	7.00×10^{-10}	1.08×10^{-9}	1.06×10^{-9}			1.14×10^{-9}	9.60×10^{-10}
22.9	1.56×10^{-9}	2.47×10^{-9}	2.44×10^{-9}			2.64×10^{-9}	2.21×10^{-9}
33.8	3.39×10^{-9}	5.54×10^{-9}	5.44×10^{-9}			5.93×10^{-9}	4.90×10^{-9}
50.0	7.32×10^{-9}	1.21×10^{-8}	1.19×10^{-8}			1.31×10^{-8}	1.07×10^{-8}

Table 3.4: Longwave absorption cross sections (m^2) for spheres (see Section 3.2) and for non-spherical crystals generated using various methods. "Multi-spheres" means that RRTM was run with a cloud of spheres with the surface-area-to-volume ratio the same as those for hexagonal columns or plates, following *Neshyba et al.* (2003) (columns 3 and 4), or for oblate or prolate spheroids (rightmost two columns), all with aspect ratios of 6. "Direct" means that single-scattering properties were generated by running the *T*-Matrix code for spheroids; for larger spheroids, the code failed to converge.

To try to gain some sense of the uncertainty associated with the use of this method, I have also shown results from several other methods in Table 3.4. The columns labeled "direct" show results where the single-scattering properties were obtained using the *T*-Matrix code for spheroids; recall that this code only converged for the few smallest sizes.

I also ran cases where I used a cloud of spheres with the surface-area-to-volume ratio matching oblate and prolate spheroids, rather than plates and columns. The results from this method are shown in the last two columns of Table 3.4 and as dotted lines in Figure 3.5. This method keeps the represented shapes consistent with the micro-physical calculations described in Chapter 2, but it amounts to an "approximation to an approximation" of the more physically realistic plate and column shapes. Also, un-like for columns and plates (*Neshyba et al.*, 2003), no publication exists comparing the radiative fluxes obtained using equal-V/A spheres to represent spheroids with the re-sults obtained using more accurate (but computationally expensive) representations of spheroids.

Figure 3.5 shows the ratios of the longwave absorption cross sections for non-spherical crystals to those for spheres–that is, the ratio of the other columns to the "Spheres" col-umn in Table 3.4. For the "multi-spheres" cases for hexagonal crystals, the results for plates and columns are very similar. For larger (> 10 μm in equivalent-mass sphere ra-dius) crystals, the non-spherical crystals absorb 50-60% more LW radiation than their spherical counterparts. For smaller crystals, the effect diminishes until the absorption coefficients are about the same for the very smallest crystals considered. For the di-rect T-Matrix calculations for spheroids, the non-spherical crystals consistently have greater absorption coefficients than their spherical counterparts, but for the smallest size considered, the *Neshyba et al.* (2003) method shows a reduction rather than an in-crease in the particle absorption, and for the next two sizes, the multi-sphere method for plates results in a much larger increase in the absorption cross section relative to spheres than does the direct calculation for oblate spheroids. For the equal-V/A calcu-lations for oblate spheroids, the resulting absorption cross sections are generally greater than those for hexagonal plates, while those for prolate spheroids are generally less than those for hexagonal columns but still greater than those for spheres (with the exception of the smallest size considered).

In the absence of more accurate methods that I have been able to get to work for all

sizes in the table, the "Plate (multi-sphere)" and "Column (multi-sphere)" cases shown in Table 3.4 and Figure 3.5 represent my current best guess as to the longwave absorption cross sections for columns and plates with aspect ratios of 6. I would put the uncertainty of these values at around ± 20%, because the largest differences in Figure 3.5 between the different methods I have tried for the same ice crystal mass are about 20%. The Future Work section (5.2) describes some alternative strategies that may produce a more accurate radiation parameterization in the future.

Figure 3.5 shows that non-spherical ice crystals with aspect ratios of 6 generally have stronger longwave radiative absorption than spheres of the same mass. For larger crystals, this effect can be as much as a factor of 1.6, but note that in the cloud-resolving model simulations described in Chapter 4, the ice crystals start with equivalent-mass sphere radii of 3.0 μm, which implies a smaller effect of a factor of about 1.1. The effects of using the non-spherical absorption coefficients derived here on the time evolution of the clouds are explored in the cloud-resolving model simulations described in Section 4.4.2.
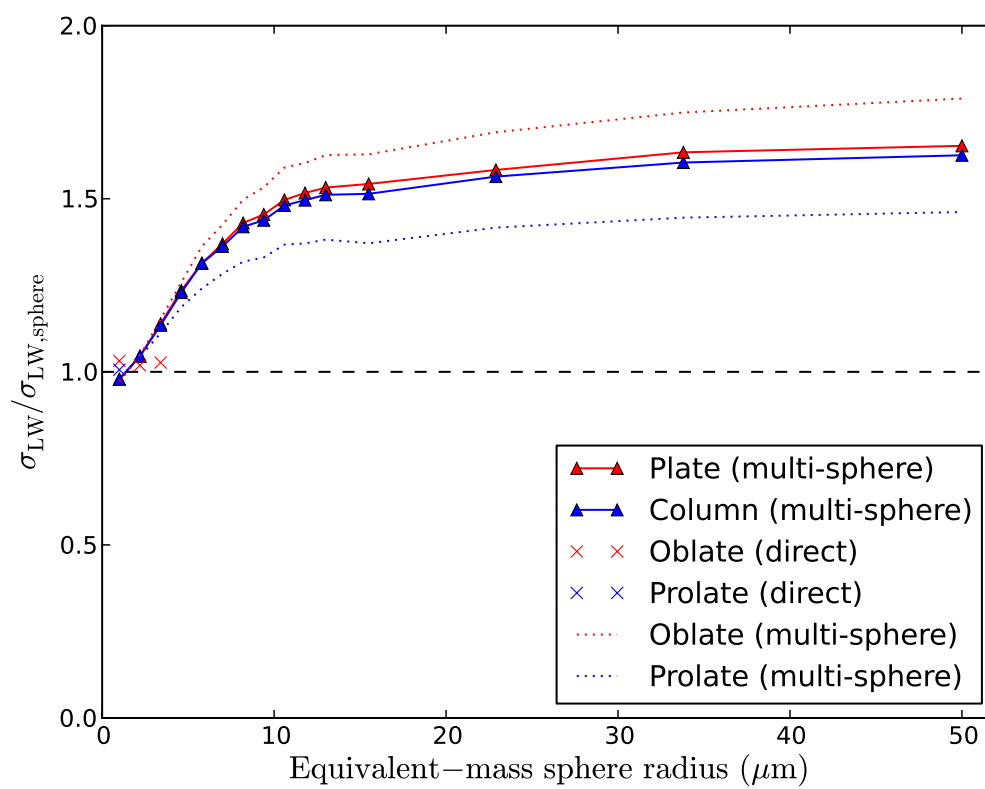
Figure 3.5: Ratios of the parameterized longwave absorption cross sections for non-spherical crystals calculated using various methods to those for spheres of equivalent mass, as a function of equivalent-mass sphere radius. The legend entries correspond to the columns of Table 3.4.

Chapter 4

CLOUD-RESOLVING MODEL SIMULATIONS

Section 4.1 briefly describes the cloud-resolving model I have been using to study thin tropical tropopause layer cirrus. Section 4.2 describes the setup of the simulations. Section 4.3 contains the results of control simulations containing spherical ice crystals. Comparisons to the simulations by *Dinh et al.* (2010) are made in order to demonstrate that the model produces similar results to previous work. Section 4.4 contains the results of simulations involving non-spherical crystals. Section 4.5 contains sensitivity tests involving more extreme changes in the fall speed and radiative absorption. Section 4.6 compares the ice crystal size distributions produced by the model to observations.

4.1 Model description

The cloud-resolving model used here is based on the System for Atmospheric Modeling (SAM), described in *Khairoutdinov and Randall* (2003). *Dinh et al.* (2012) replaced the SAM advection scheme with the selective monotonicity-preserving scheme described by *Blossey and Durran* (2008). I have not made any further changes to the model's dynamics. See Chapters 2 and 3 for descriptions of the microphysics and radiative transfer schemes, respectively, including the schemes used by Dr. Dinh and the changes I have made to them. *Dinh* (2012) and *Dinh et al.* (2012) provide good descriptions of the dynamical core of the model and how the microphysics and radiation calculations interact with the dynamics.

Durran et al. (2009), *Dinh* (2009) and *Dinh et al.* (2010) used a different cloud-resolving model, called Meso06. The switch to SAM was made after the 2010 paper.

4.2   Model setup

The model domain is in 2 dimensions, the zonal (x) and the vertical (z). The location is assumed to be on the equator, so that the Coriolis force can be ignored. The vertical resolution is 25 m and the horizontal resolution is 100 m. The domain extends 432 km in the x-direction and 3.25 km in the z-direction, from 14.75 km to 18 km.[1]

4.2.1   Boundary conditions

The dynamical boundary conditions are periodic on the lateral edges and employ the non-reflective, open boundary conditions described by *Bougeault* (1983) and *Klemp and Durran* (1983) at the top and bottom of the domain.[2]

  The cloud-resolving model does not calculate radiative transfer except in the cloud. The radiation boundary conditions (radiative fluxes entering the cloud) are generated using a radiative transfer model (RRTM in the longwave and RAPRAD in the shortwave) for a clear-sky case in a typical tropical atmosphere.[3] The fluxes exiting the cloud are calculated according to Equations 3.2 and 3.3, but for each cloudy model layer instead of the entire cloud.[4] This calculation uses the broadband absorption cross sections derived in Chapter 3.

---

[1]These dimensions were chosen to be similar to those used in *Dinh et al.* (2010), while satisfying additional constraints imposed by the SAM Model. SAM requires that the prime factorization of the horizontal domain dimension include only 2, 3, and 5. Also, I have been running the model on 12 parallel processors, with the domain divided into 12 subdomains in the x-direction. Therefore, the number of grid boxes in the horizontal dimension must be divisible by 12. 4320 (but not 4000) satisfies all of these conditions. The number of vertical levels (130 in this case) must be 2 less than a number divisible by 12.

[2]*Dinh et al.* (2010) instead employed a damping layer between the altitudes of 12.5 and 14.5 km to prevent waves from reflecting off the bottom of the domain. The more efficient boundary condition used here had not yet been programmed into the model in 2010.

[3]Specifically, the profile used is a March climatological average in the Galápagos (*Gettelman et al.*, 2004).

[4]For the purposes of the radiation calculation, the top and bottom of the cloud are defined as being the highest and lowest model layers, respectively, in which the horizontally integrated total cloud number concentration is at least 1 per square meter in the zonal-vertical plane.

4.2.2 Cloud configuration

The initial ice crystal number concentration is specified as follows, as in *Dinh et al.* (2010):

$$N = N_0 f(x) g(z) \tag{4.1}$$

where[5,6]

$$f(x) = \begin{cases} 1 & \text{if } x < a \\ \cos^2\left(\frac{\pi}{2a}(x-a)\right) & \text{if } a \leq x \leq 2a \\ 0 & \text{otherwise} \end{cases} \tag{4.2}$$

and

$$g(z) = \begin{cases} \cos\left(\frac{\pi}{2d}(z-z_c)\right) & \text{if } (z_c - d) \leq z \leq (z_c + d) \\ 0 & \text{otherwise} \end{cases}. \tag{4.3}$$

The initial maximum number concentration N_0 is set to 1.3×10^6 m^{-3}; the cloud quarter-width a is set to 40 km; the height of the cloud center z_c is set to 16.25 km; and the cloud half-thickness d is set to 250 m. The ice crystal size distribution is initially monodisperse, with crystals of radius 3.0 μm, or in the case of non-spherical crystals, having the equivalent mass of a 3-micron-radius sphere. Nucleation of new ice crystals is not considered, but ice crystals can grow or shrink by deposition and sublimation. Figure 4.1 shows the ice mixing ratio at model initialization; *cf. Dinh et al.* (2010), their Figure 2.

4.2.3 Temperature and humidity profiles

The initial temperature profile used in the model is an average of 12 radiosonde profiles taken in Nauru, a tropical Western Pacific site with frequent TTL cirrus coverage (*Mace*

---

[5]Here $x = 0$ at the center of the domain.

[6]The code instead uses $\sin^2\left(\pi\left(1 - \frac{x}{2a}\right)\right)$ in the definition of $f(x)$, which is algebraically equivalent to, but less intuitive than, what is printed here.

Initial ice mixing ratio (kg/kg)
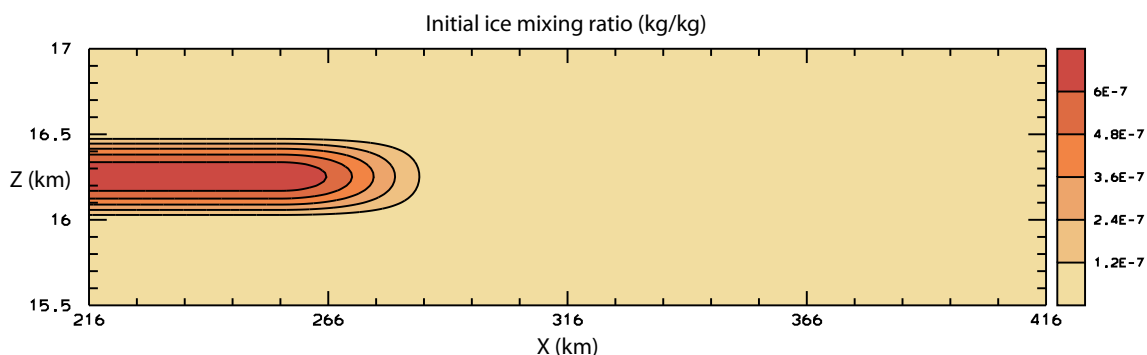
Figure 4.1: Initial ice mixing ratio (kg/kg) for all simulations. Only the right side of the domain is shown; the left side mirrors it. Portions of the domain from 14.75 to 15.5 km and from 17.0 to 18.0 km also omitted. Compare to Figure 2 of *Dinh et al.* (2010).

et al., 2009), on 1 through 12 January 2007 as part of the Atmospheric Radiation Measurement (ARM) program. Figure 4.2 (left panel) shows this temperature profile. This atmosphere is statically stable throughout the domain, with stability generally increasing with height. The temperature minimum of 188 K is located about 1 km above the middle of the initial cloud. *Dinh et al.* (2010) also used this temperature profile.

The initial water vapor profile is set so that the relative humidity is 100% in the cloud layer, including to the sides of the cloud, and 80% above and below the cloud layer. This results in an absolute humidity profile that mostly follows the temperature profile. *Dinh et al.* (2010) also used this configuration. Figure 4.2 shows the vertical profiles of the temperature and the absolute and relative (with respect to ice) humidity at the beginning of the simulation.

A second set of simulations was also done, with a different initial humidity profile that had smoother transitions at the top and bottom of the cloud. These simulations illustrate the importance of the initial humidity profile to the cloud evolution. The results from these simulations are shown in Appendix C.
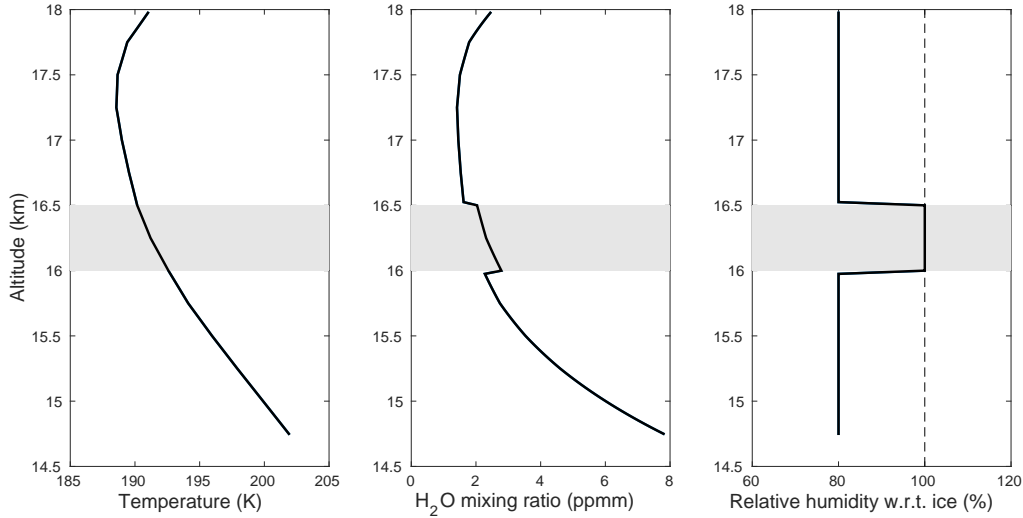
Figure 4.2: Initial profiles of temperature (left), water vapor mixing ratio (center), and relative humidity with respect to ice (right). The dashed line indicates saturation. The gray rectangle indicates the initial location of the cloud. At the beginning of these simulations, these quantities do not depend on x, although the ice number concentration does depend on x.

4.3 Control simulation: spherical crystals

My simulations include a pre-existing cloud with no prescribed large-scale motion, so that the only fluid motions in the simulation are induced by the radiative heating of the cloud. This is the setup used in *Dinh et al.* (2010). To verify that the model is producing reasonable results, I have tried to reproduce the results of *Dinh et al.* (2010) as well as possible. I have been able to get results that are mostly similar, but have several differences.

Figure 4.3 shows the horizontal velocity (u), vertical velocity (w), and potential temperature perturbation (θ') at an elapsed time of 6 hours for the sphere simulation, over the portion of the domain shown in Figure 4.1. These plots show the radiative heating
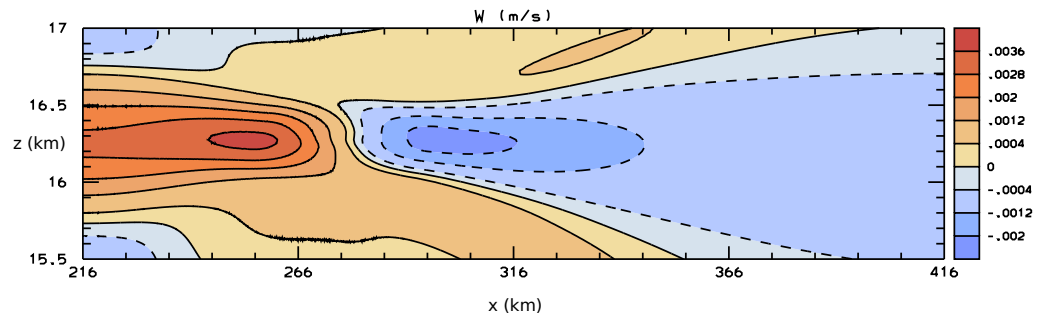
(a)
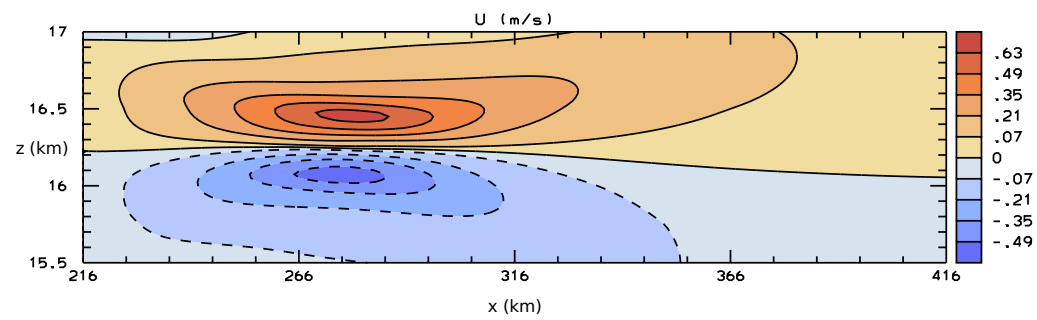
(b)
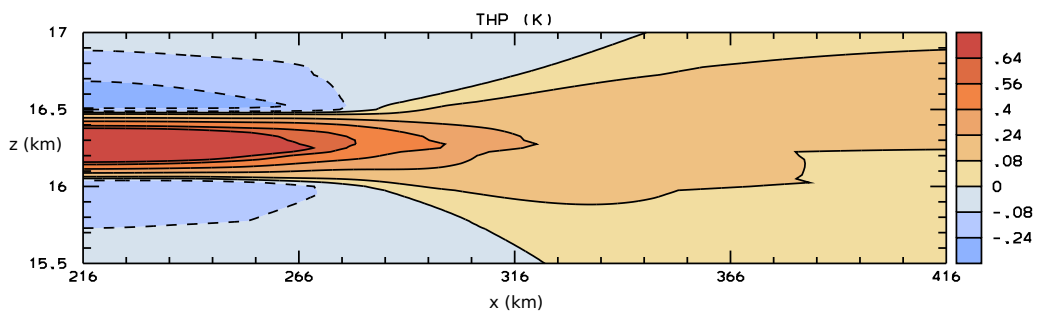
(c)

Figure 4.3: Plots of vertical velocity (a), zonal velocity (b), and potential temperature perturbation (c) at an elapsed time of 6 hours for a SAM cloud-resolving model simulation with all spherical crystals. *cf. Dinh et al.* (2010), their Figure 3.

of the cloud and the resulting circulation. The w plot shows rising motion inside the cloud and sinking motion outside it. The u plot shows divergence above the cloud and convergence below it. The θ' plot shows strong positive potential temperature perturbations in the cloud, due to radiative heating of the ice crystals. The weak positive potential temperature perturbations to the sides of the cloud are associated with advection of radiatively heated air, and with subsidence, which raises the potential temperature in an Eulerian sense in a stably stratified atmosphere. The negative potential temperature perturbations above and below the cloud are due to rising motion. The plot window and contour intervals are the same as in Figure 3 of *Dinh et al.* (2010), in order to allow a direct comparison. My plots look qualitatively similar to those of *Dinh et al.* (2010), but quantitatively, they are not exactly the same.

Figure 4.4a shows the ice mixing ratio of the cloud 24 hours after the model initialization. Several important features should be pointed out. The cloud has spread out horizontally at the top and has narrowed at the bottom; this is consistent with what we would expect based on the u field shown in Figure 4.3. Also, the ragged top of the cloud indicates small-scale convection, which is due to instability generated by the radiative heating of the cloud but not the air above it. Figure 4.4b shows the ice mixing ratio of the cloud at $t = 48$ hours. By then, the cloud base has narrowed even further, and the cloud top convection has congealed into fewer, larger cells.

Figure 6b of *Dinh et al.* (2010) shows the ice mixing ratio at 24 hours for an equivalent simulation. Their simulation shares major features with mine, including the convection and spreading at the cloud top, the narrowing at the cloud base, and the maintenance of the 16 km height of the cloud base. The main difference is that their simulation produces greater ice mixing ratios in the center of the cloud than does mine. Likewise, figure 6d of *Dinh et al.* (2010) shows a similar structure to my Figure 4.4b at 48 hours, but with more ice mass overall. Here are several differences between the simulations that could explain the discrepancies:

(a)

(b)
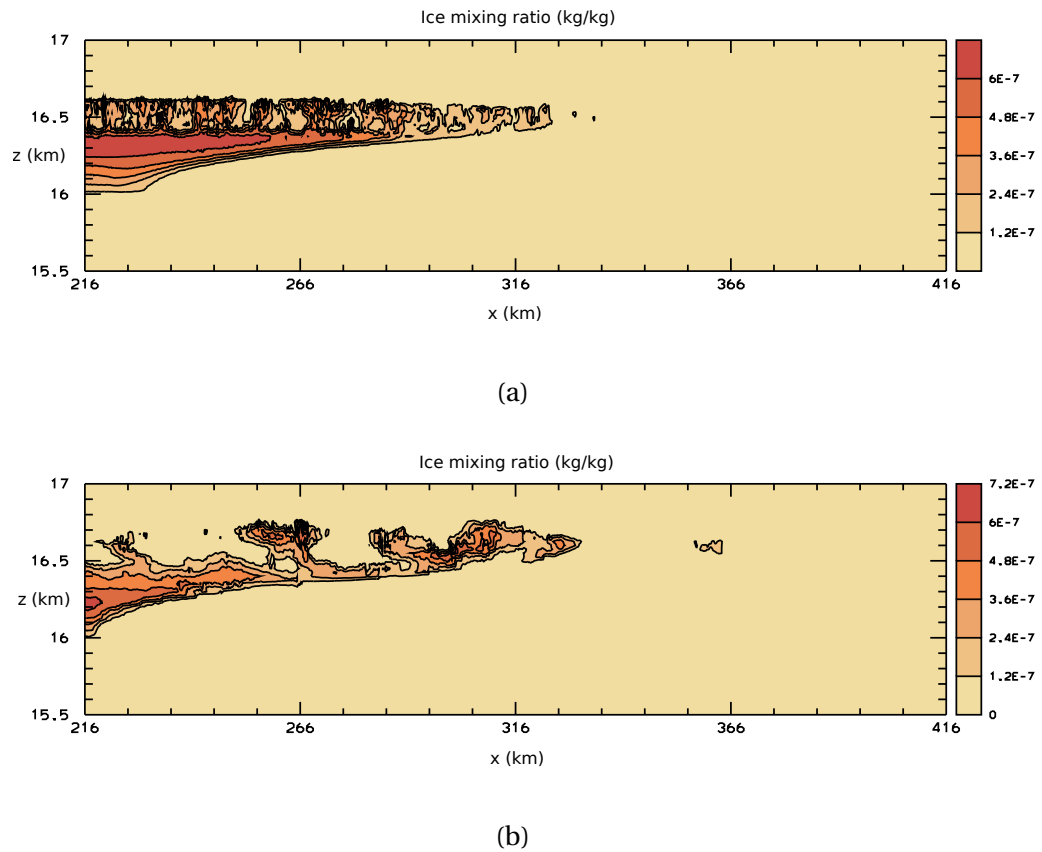
Figure 4.4: Ice mixing ratio at 24 hours (a) and 48 hours (b) for the control simulation with all spheres. Compare to Figure 4.1 and to *Dinh et al.* (2010), their Figures 6b and 6d.

- The model used is different (SAM in my simulations vs. Meso06 in *Dinh et al.* (2010)).

- The simulations of *Dinh et al.* (2010) used a different microphysics scheme (*Chen and Lamb*, 1994), which included only 10 size bins rather than the 25 used here. *Dinh and Durran* (2012) showed that these types of changes in the microphysics scheme can result in significant differences in the modeled cloud radiative heating rate.

- The fall speeds in my simulation are being calculated according to Stokes's Law rather than the method of *Böhm* (1989) (see Section 2.1).

- I have recalculated the LW ice crystal absorption cross sections for spheres and the radiative boundary conditions using a different radiative transfer model and updated optical constants of ice (see Sections 3.2.2 and 3.2.3).

I would argue that the agreement between my simulations and those of *Dinh et al.* (2010) is not good enough to directly compare my non-spherical cases with the spherical cases from *Dinh et al.* (2010), but it is good enough that we can take my spherical simulations as a reasonable control case against which the non-spherical simulations in the next section can be compared.

4.4   Non-spherical cases

I have incorporated non-spherical crystals into the calculation of three modeled properties: fall speeds, growth rates and longwave radiative absorption. For the fall speeds and growth rates, I have replaced spheres with oblate and prolate spheroids with aspect ratios of 6. See Chapter 2 for the details of this calculation. For the radiative absorption, I have regenerated the LW absorption cross section lookup table using a collection of spheres that have the same surface-area-to-volume ratio as hexagonal plates or columns with aspect ratios of 6, a method developed by *Neshyba et al.* (2003). See Chapter 3 for the details of this calculation.

This section explores the effects of these changes on the time evolution of the clouds. To quantify these effects, I have looked at several domain-integrated variables, including the cloud center of mass, the total ice mass, and the mean mass of the ice crystals. Section 4.4.1 explores the effects of the changes in the microphysics, while Section 4.4.2 explores the effects of the changes in the radiative absorption. Appendix C contains results from experiments similar to those presented here but with a different initial relative

humidity profile in the model. Section 4.5 contains results of some additional sensitivity tests in which fall speeds and radiative absorption coefficients are subjected to more extreme changes that go beyond the effects of ice crystal shape.

4.4.1 Effects of changes in microphysics

To isolate the effects of changes in microphysics, I have run the model with fall speeds and growth rates changed to the spheroid calculations one at a time and together, but still using spheres for radiative absorption. Figure 4.5a shows the center of mass of the cloud ice as a function of time for four simulations: the sphere (control) case; a case with oblate spheroids used for the fall speeds but spheres used for the growth rates; a case with spheres used for the fall speeds but oblate spheroids used for the growth rates; and a case with spheroids used for both fall speeds and growth rates. Figure 4.5b shows similar runs but for prolate spheroids.

All of the simulations show the center of mass increasing monotonically with time. This is due to some combination of the clouds being lifted by the radiatively induced circulation and the development of small-scale convection at the cloud top. Changing the growth rate to the spheroidal calculation has a negligible effect on the center of mass for most of the simulation, but doing the same for fall speeds results in a higher center of mass at all elapsed times. Recall (Figure 2.2) that these spheroids have fall speeds reduced by about a factor of about 1/3 compared with equivalent mass spheres. Therefore, a higher cloud center of mass is consistent with expectations.

Figure 4.6 shows the total mass of the cloud as a function of time for the same four cases.[7] These results are less straightforward than those for the center of mass. In all the simulations, there is an initial decline in the ice mass, which can be attributed to relative humidity decreases arising from local diabatic heating while the radiatively induced circulation is spinning up (see Section 4.5.2). After a minimum at about 9 hours,

---

[7]Since this is a 2D model, after integrating over x and z, the resulting mass is per unit length in the y direction.
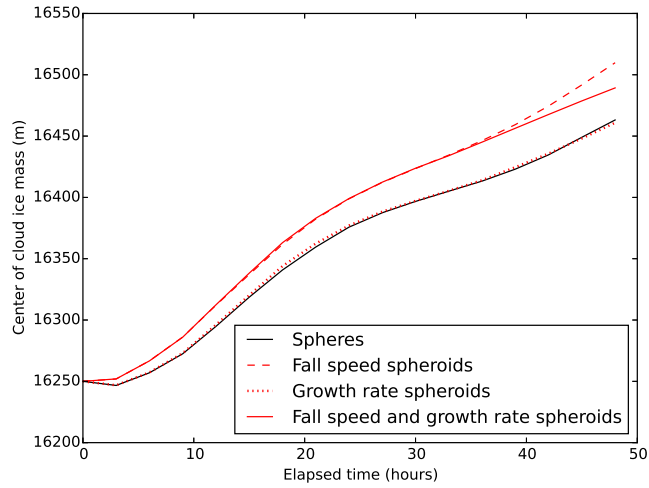
(a)
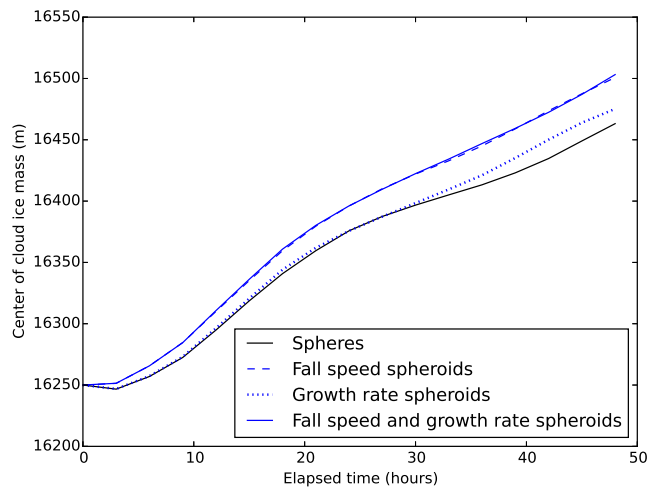
(b)

Figure 4.5: Cloud center of mass as a function of time, for spheres (black, both panels) and oblate (red, (a)) and prolate (blue, (b)) spheroids with aspect ratios of 6. Dashed lines: spheroidal shape considered only for fall speed. Dotted lines: spheroidal shape considered only for growth rate. Solid colored lines: spheroidal shape considered for both fall speeds and growth rates.

(a)

(b)

Figure 4.6: Total cloud ice mass (kg per m in *y* direction) as a function of time, for spheres (black, both panels) and oblate (red, (a)) and prolate (blue, (b)) spheroids with aspect ratios of 6. Dashed lines: spheroidal shape considered only for fall speed. Dotted lines: spheroidal shape considered only for growth rate. Solid colored lines: spheroidal shape considered for both fall speeds and growth rates.

there is a rebound in the ice mass, which peaks at about 18 hours. Using spheroidal fall speeds results in a greater total cloud ice mass than the control simulation during the first day, possibly because fewer crystals are falling into the subsaturated below-cloud region. For spheroidal growth rates, both the initial decline and the subsequent rebound are stronger, consistent with the magnitude of dm/dt being greater for spheroids than for spheres (as shown in Figure 2.3), which would mean that ice crystals would grow faster (in a mass sense) in a supersaturated environment and shrink faster in a subsaturated environment. The results of the simulations with spheroids used for both fall speeds and growth rates suggest that the effects of fall speed and growth rate often cancel if they are of opposite signs, and add if they are of the same sign. However, there are times when the combined fall speed/growth rate case is much different from the other three cases, suggesting that the two processes interact in nonlinear ways and should not be assumed to be additive.

After the peak at around 18 hours, there is a sustained decline in the total ice mass, and by 48 hours, the cloud has lost about 30% of its mass. This is different from the simulations of *Dinh et al.* (2010), who found a continued rise in cloud ice mass during the second day (see their Figure 8a).[8] The circulation in my model is generally somewhat weaker than that in Tra Dinh's simulation, likely due to one of the model differences listed above.

Since the model allows ice crystals to shrink until they disappear but does not allow new crystals to nucleate, looking at the mean ice crystal mass instead of the total cloud ice mass gives us a different sense of what is happening to the individual crystals. Figure 4.7 shows this quantity as a function of time, for the same four cases. In the first 18

---

[8]When comparing the total ice mass at 0 h in my figures and those of *Dinh et al.* (2010), there appears to be a discrepancy. My initial ice mass is greater by about a factor of 2, because my simulation includes both the left and right half of the domain while Tra Dinh's included only half, with a symmetric boundary condition in the middle. Still, the initial ice mass in my simulations is not *exactly* twice that in Tra Dinh's, as would be expected. If I do a double integral of Equation 4.1 in x and z and multiply by the mass per ice crystal, I get an answer for the total mass that is more consistent with my figure than with Tra Dinh's figure. Different ways of interpolating the continuous functions $f(x)$ and $g(z)$ onto the discrete model grids may account for the discrepancy.
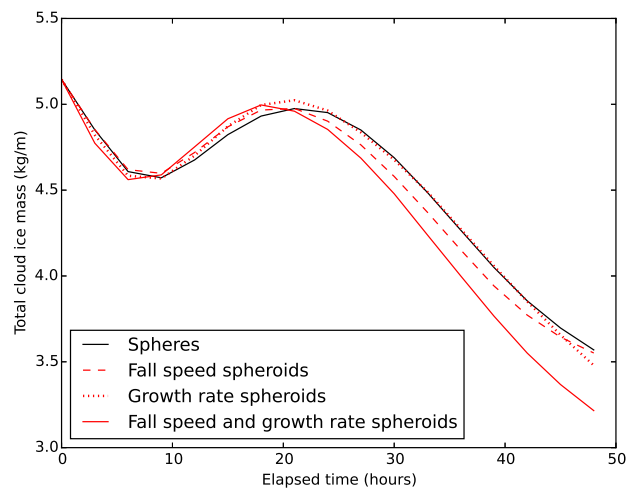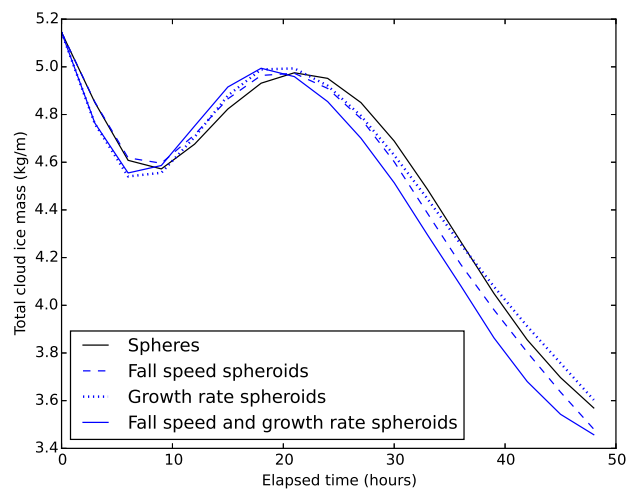
(a)
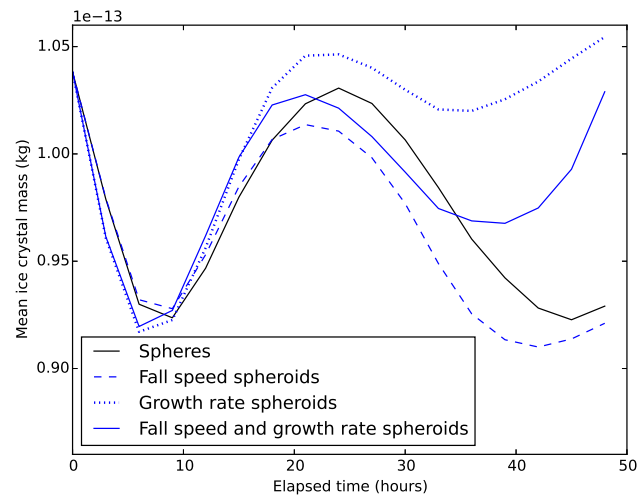
(b)

Figure 4.7: Mean ice crystal mass (kg) as a function of time, for spheres (black, both panels) and oblate (red, (a)) and prolate (blue, (b)) spheroids with aspect ratios of 6. Dashed lines: spheroidal shape considered only for fall speed. Dotted lines: spheroidal shape considered only for growth rate. Solid colored lines: spheroidal shape considered for both fall speeds and growth rates.
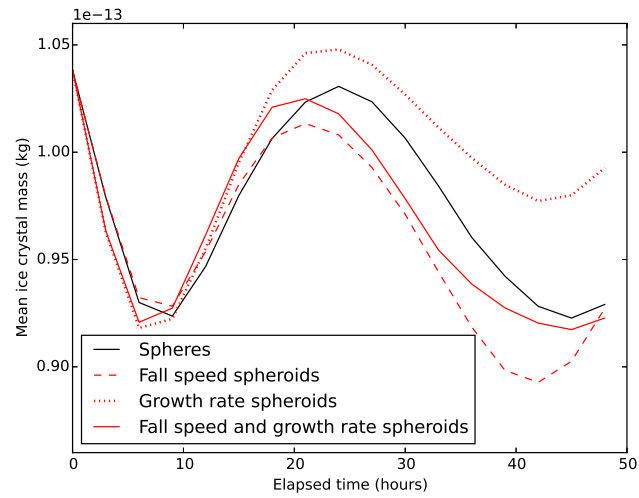
hours, the runs using spheroids for fall speed only are similar to the control case and the runs using spheroids for growth rate only are similar to the runs using spheroids for both fall speed and growth rate, suggesting that the growth rate calculation is of primary importance for how large the individual crystals grow during this part of the simulation.

After the peak, the second decline is much less pronounced in the mean ice crystal mass plots than in the total ice mass plots, and there is a second rebound that appears in some of the cases. The mean ice crystal mass never varies by more than about 15% in any of these simulations. The fact that a pronounced decline is seen in the total ice mass but not the mean crystal mass plots suggests that most of the mass loss is from crystals that shrink until they disappear entirely. This would seem to point to sedimentation below the bottom of the cloud as the reason for the decline in the total ice mass, because ice crystals that fall below the cloud never have a chance to regrow and therefore are removed from the mean crystal mass calculation once they are gone.

It is also worth noting that the spread in the mean ice crystal mass between the different model runs is much greater in the 2nd day of the simulation than in the first. This may be because a greater fraction of the cloud mass in the second day is located in the cloud-top convective cells (see Figure 4.4). It appears that these turbulent cells are chaotic and therefore sensitive to small changes in the physical constants. Even the difference between oblate and prolate spheroids, which has very little impact on the fall speeds and growth rates of individual ice crystals (Figures 2.2 and 2.3), makes a large difference to the mean ice crystal mass by 48 hours, particularly for the case that assumes a spheroidal shape for both fall speed and growth rate.

It may appear that there is a diurnal cycle in the mean ice crystal radius. However, there is no diurnal cycle in any physical process in the cloud-resolving model used here, therefore the apparent dirunal cycle is coincidental. The shortwave radiative heating assumes a constant $40°$ solar zenith angle. Appendix B argues that the possible error arising from this assumption is small.

4.4.2   Effects of changes in radiation

This section examines the results of cloud-resolving model simulations incorporating the longwave absorption cross sections for non-spherical crystals (plates and columns with aspect ratios of 6) derived in Section 3.3. The results are compared to the case from Section 4.4.1 including the effects of non-spherical shape for fall speed and growth rate but not radiation, and the control case from Section 4.3, which assumed a spherical shape for all calculations.

Figure 4.8 shows the cloud center of mass as a function of time for these cases. Comparing the result where non-spherical shape is considered for radiation to the result where shape is considered only for microphysics gives us insight into the specific role that radiation plays. The non-sphere radiation case has a higher center of mass than the other cases. Looking at the case in which non-spherical shape is considered for microphysics but not radiation suggests that microphysics is responsible for about 60% of the center of mass increase relative to the control case, and radiation is responsible for the remaining 40%, except at the very end when it is closer to 50/50. Recall from Section 3.3.2 that the ice crystal absorption cross sections for columns and plates calculated using the method of *Neshyba et al.* (2003) are generally greater than those for spheres of equivalent mass. Therefore, the radiative heating of the cloud is stronger in the runs using these numbers, and this additional heating induces stronger updrafts. Plots of the w field at 6 hours from the various cases (not shown) indicate that the updrafts are in fact stronger in simulations including the non-spherical radiation coefficients.

Figures 4.9 and 4.10 show the total ice mass and the mean ice crystal mass, respectively, as a function of time for the same three cases. Using the non-spherical absorption coefficients, and therefore increasing the radiative absorption, results in less total ice mass at all times relative to the simulation with spheroid microphysics but spherical radiation, and a similar result is seen in the mean crystal mass plots, except in the last few hours in the oblate case. This is a seemingly paradoxical result, because if there were no
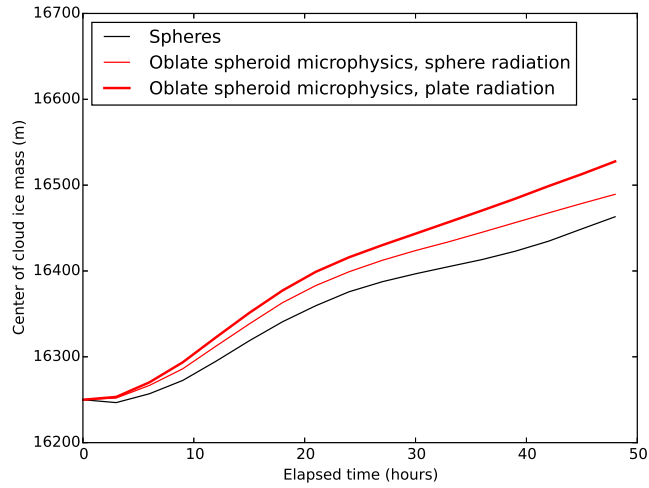
(a)
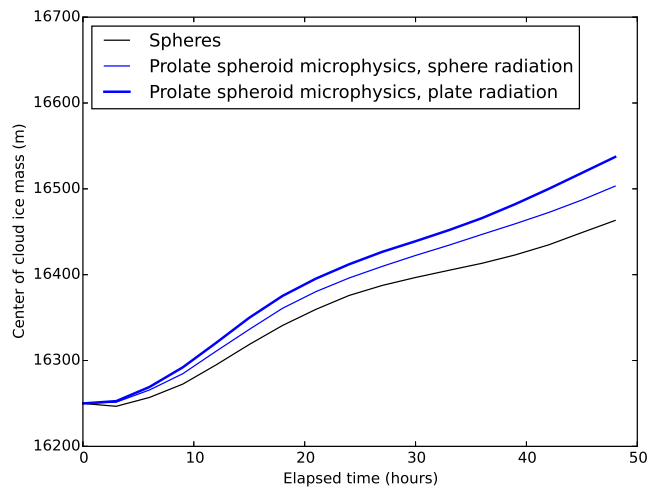
(b)

Figure 4.8: Cloud center of mass as a function of time, for spheres (black, both panels; control case) and oblate (red, (a)) and prolate (blue, (b)) spheroids with aspect ratios of 6. Thin, colored lines: non-spherical shape considered for fall speed and growth rate only. Thick, colored lines: non-spherical shape considered for fall speed, growth rate, and LW radiative absorption.

(a)

(b)

Figure 4.9: Total cloud ice mass (kg per m in *y* direction) as a function of time, for spheres (black, both panels; control case) and oblate (red, (a)) and prolate (blue, (b)) spheroids with aspect ratios of 6. Thin, colored lines: non-spherical shape considered for fall speed and growth rate only. Thick, colored lines: non-spherical shape considered for fall speed, growth rate, and LW radiative absorption.
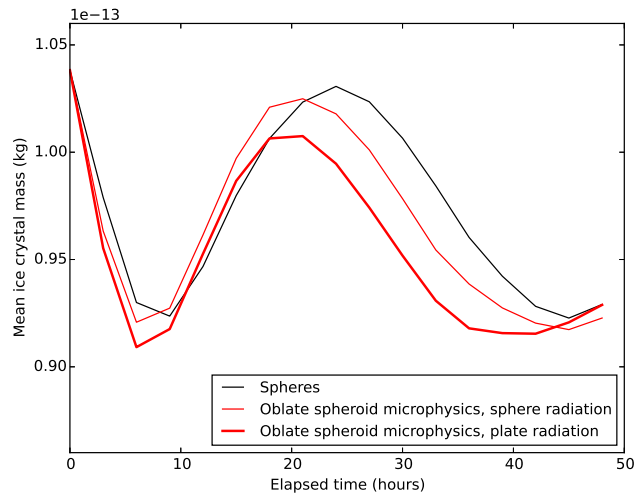
(a)

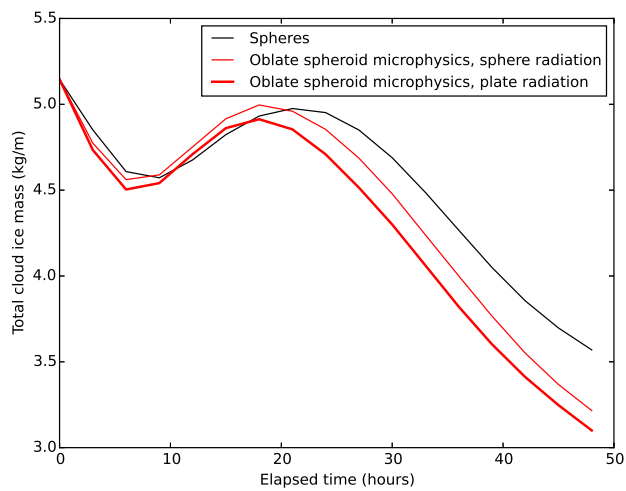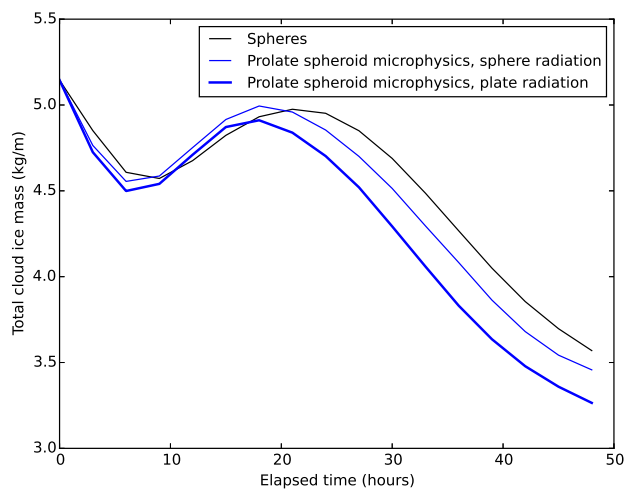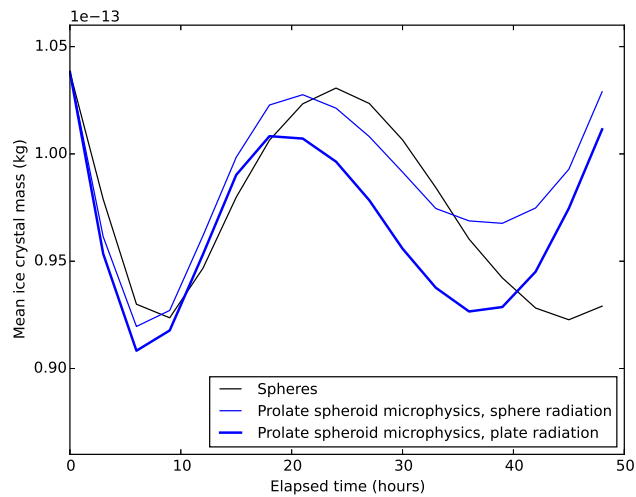

(b)

Figure 4.10: Mean ice crystal mass (kg) as a function of time, for spheres (black, both panels; control case) and oblate (red, (a)) and prolate (blue, (b)) spheroids with aspect ratios of 6. Thin, colored lines: non-spherical shape considered for fall speed and growth rate only. Thick, colored lines: non-spherical shape considered for fall speed, growth rate, and LW radiative absorption.

radiative heating, there would be no updrafts to maintain the cloud against sedimentation and the cloud would quickly dissipate. However, besides strengthening updrafts, increased radiative heating also has the potential to reduce the relative humidity by increasing the temperature locally, an effect which would compete with the additional moisture convergence and adiabatic cooling caused by stronger updrafts. Analysis is ongoing to see whether this effect is responsible for the quite counterintuitive result seen here. It may be that there is an ideal amount of radiative heating for maintaining thin TTL cirrus, and that too much radiation will actually tend towards dissipating the cloud. It could be that the control simulations presented here already involved more than the optimum amount of radiative absorption.

4.5 Additional sensitivity tests

In order to better understand the physical reasons for ways ice crystal shape affects the cloud evolution, I have run some additional sensitivity tests to changes in the fall speed and radiative absorption that go far beyond what would be expected based on non-spherical shape. The results of these experiments are discussed here.

4.5.1 Zero fall speed test

It may seem surprising that reducing ice crystal fall speeds by about 1/3 by assuming oblate or prolate spheroids with aspect ratios of 6 only resulted in about a 40 meter increase in the center of cloud ice mass at 48 hours (see Figure 4.5). But in order to determine whether this decrease is consistent with our physical intuition, it is necessary to look at what happens when sedimentation is turned off entirely.

Figure 4.11 shows the center of mass as a function of time in the control simulation, a simulation with oblate spheroidal shape assumed only for the fall speed calculation, and a simulation in which fall speeds were set to zero. (All of these simulations assumed spheroidal shape for the growth rate and radiative absorption.) When the sedimentation is turned off, the cloud is lofted by the radiative heating so that at 48 hours, the center
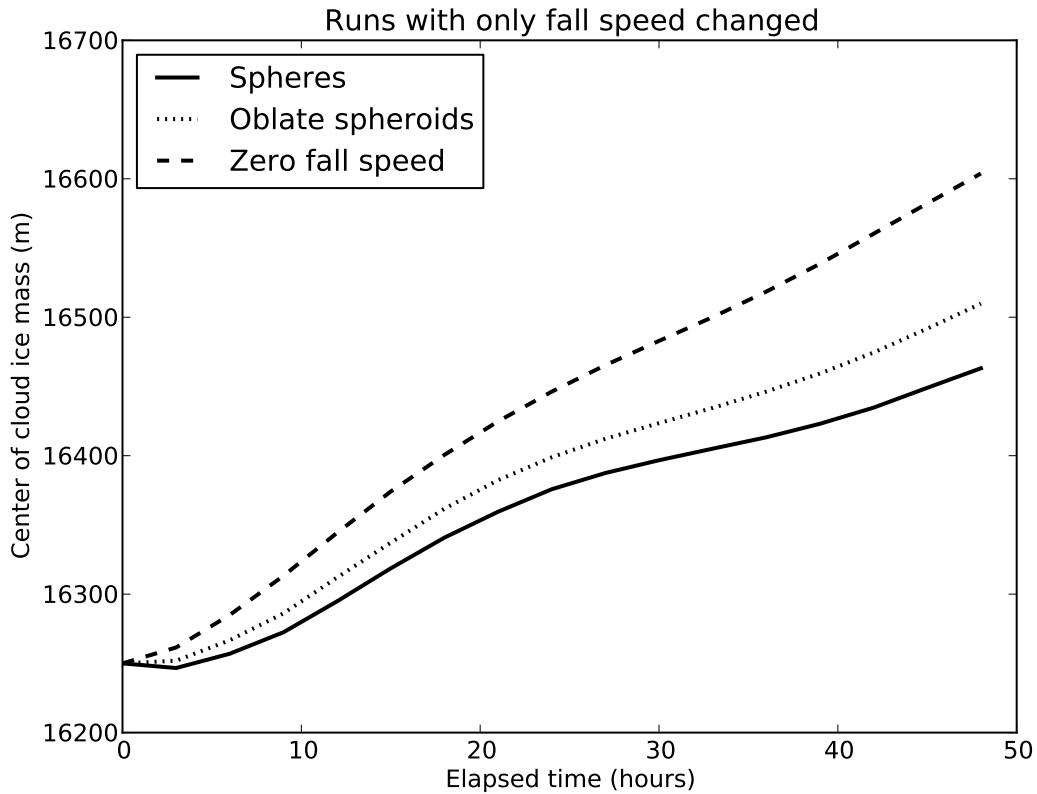
Figure 4.11: Center of cloud ice mass as a function of time in the spherical control run, a run assuming spheroidal geometry for the fall speed only (and therefore reducing fall speeds by about 1/3), and a run with sedimentation turned off.

of mass is roughly 150 m higher than in the control case. The center of mass in the spheroid case is about a third of the way between the control and zero fall speed cases, which is consistent with an intuitive expectation of what would happen when reducing fall speeds by 1/3.

4.5.2 Radiative absorption multiplier tests

The most surprising result from the previous sections was that increasing the cloud radiative absorption, by switching from the spherical to the plate or column absorption

cross sections derived in Chapter 3, actually reduced the total ice cloud mass. This seems paradoxical because the radiative absorption is responsible for the cloud being able to maintain itself against sedimentation.

To see if this effect is robust and to investigate the physical reasons for it, it is helpful to look at what happens when more extreme changes are made to the radiative absorption. I have put two "knobs" into the model that allow the LW or SW absorption to be multiplied by any (real) number. I have run one case with the LW absorption doubled relative to the spherical case, one case with the LW absorption halved relative to the spherical case, one case with the SW absorption set to zero, and one case with both the SW and LW absorption set to zero. Figures 4.12 and 4.13 show the cloud ice center of mass and total ice crystal mass, respectively, in these cases as well as the control case described in Section 4.3.

The center of mass plots (Figure 4.12) show that in general, the greater the radiative absorption, the more the cloud is lofted over time. This is what would be expected given that the radiative absorption is responsible for the updrafts that lift the cloud. With all radiative absorption shut off, the center of mass decreases nearly linearly as the ice crystals slowly fall down. The run with the shortwave absorption shut off is very similar to the control run, indicating that the shortwave absorption is not very important; while the shortwave absorption is not negligible, small changes to it due to ice crystal shape or a diurnal cycle would not significantly affect the cloud evolution. Appendix B contains another line of evidence that the SW absorption is relatively important. The longwave absorption accounts for most of the total absorption, so halving or doubling the longwave absorption has a much larger effect than shutting off the shortwave absorption.

The total ice mass plots (Figure 4.13) confirm the apparently paradoxical result from the previous section that more radiative absorption results in less total ice mass, with the exception of the run with all radiative absorption turned off. With no radiative absorption, the total ice mass begins to decline as the ice crystals falls into the subsaturated region below the cloud's original location, and there is no circulation to counteract this
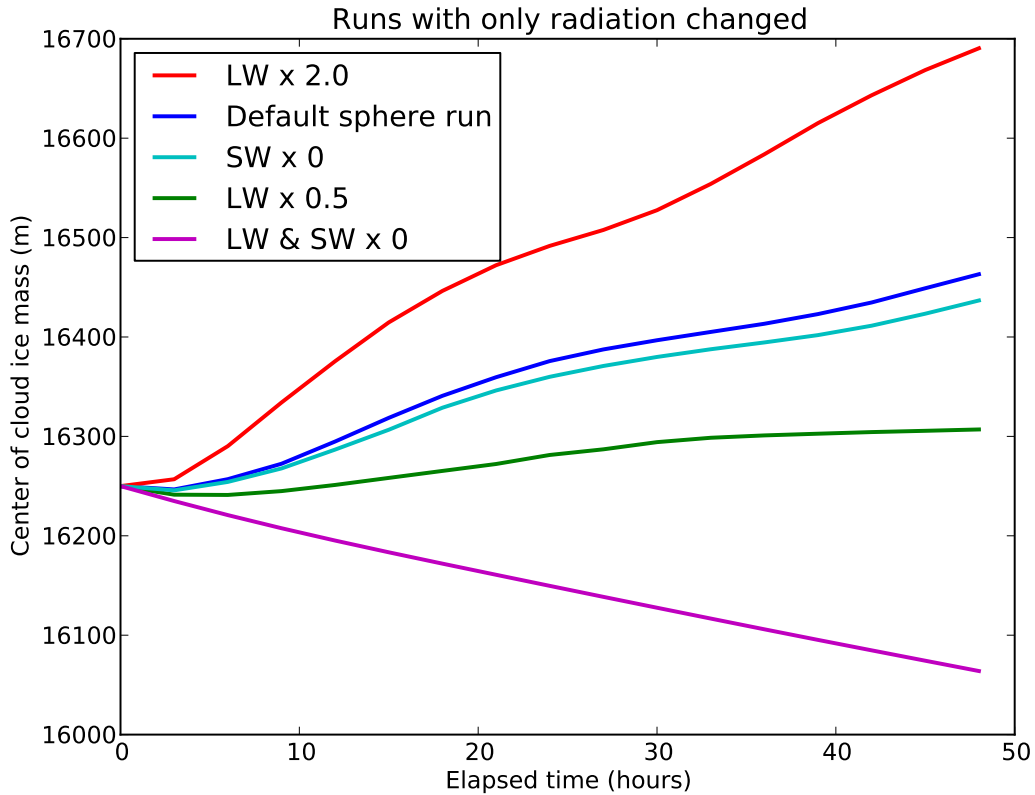
Figure 4.12: Center of cloud ice mass as a function of time in the control run (blue), a run with the short-wave absorption turned off (teal), a run with the longwave absorption doubled (red), a run with the long-wave absorption halved (green), and a run with both the longwave and the shortwave absorption turned off (magenta). All of these simulations assumed spherical crystals for the microphysical calculations.

effect. Therefore, radiative absorption is necessary to maintain the cloud. However, the other runs indicate that there is an optimum amount of radiative absorption that will maximize the peak ice cloud mass in the simulation; after that optimum is passed, additional absorption lowers the peak cloud ice mass, as well as shifting the peak to earlier times.

The physical reasons for the inverse relationship between absorption and peak ice crystal mass are still under investigation. But the situation in the model spin-up period
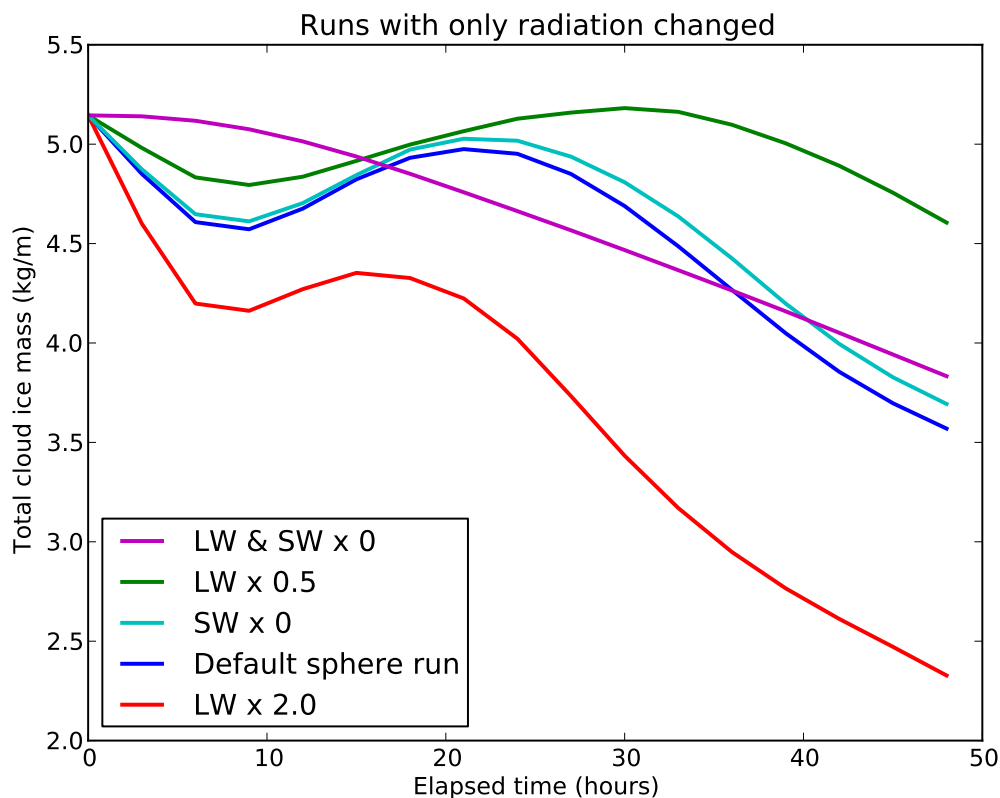
Figure 4.13: Total ice mass as a function of time in the control run (blue), a run with the shortwave absorption turned off (teal), a run with the longwave absorption doubled (red), a run with the longwave absorption halved (green), and a run with both the longwave and the shortwave absorption turned off (magenta). All of these simulations assumed spherical crystals for the microphysical calculations.

in the first 9 hours is relatively straightforward. Before running these simulations, I had thought that the initial decline in ice mass in the control simulations was because of ice crystals sedimenting into the subsaturated region below the cloud, but the very slow initial decline in total ice mass in the run with no radiative absorption shows that sedimentation could not be responsible for most of the initial ice mass decline in the control run. Instead, the radiative heating must be directly involved in this decline. The stronger the radiative heating, the greater the initial decline in cloud ice mass.
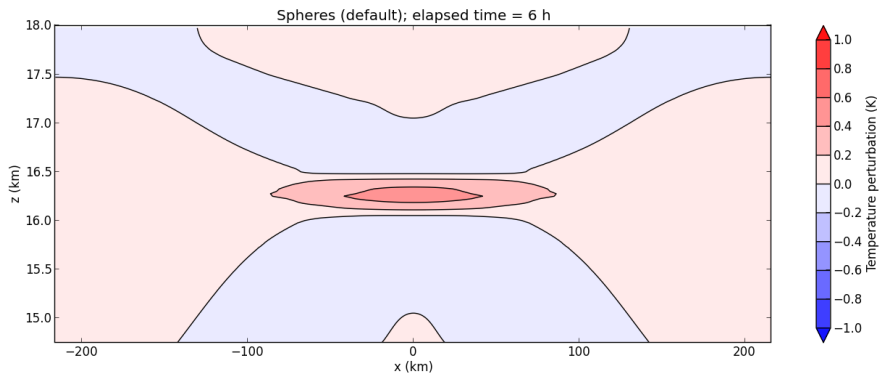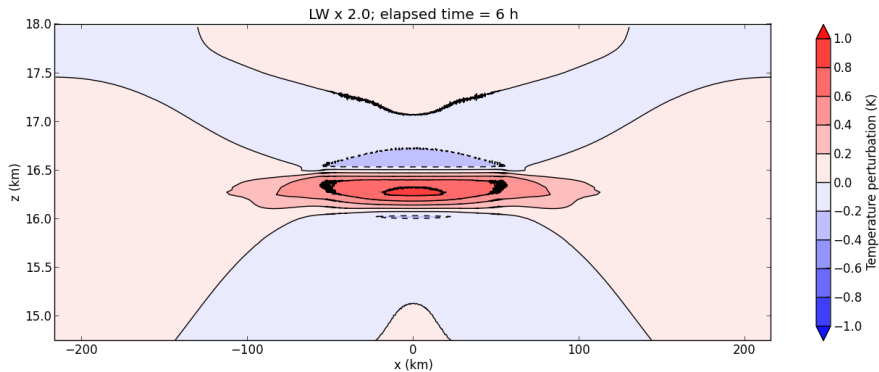
Figure 4.14: Temperature perturbation (K) at 6 hours in control spherical simulation (a) and simulation with doubled LW absorption (b). The initial cloud was between 16 and 16.5 km, centered at x = 0, and extended out 80 km from the center.

In support of this argument, Figures 4.14 and 4.15 show contour plots of the pertur-
bation temperature and supersaturation ratio with respect to ice, respectively, at $t = 6$
hours in the control case and the case with doubled LW absorption. These plots show
that doubling the radiative absorption raises the temperature in the center of the cloud,
due to local diabatic heating. As for the relative humidity, the case with doubled LW
absorption has lower relative humidity in the center of the cloud, where the ice mass is
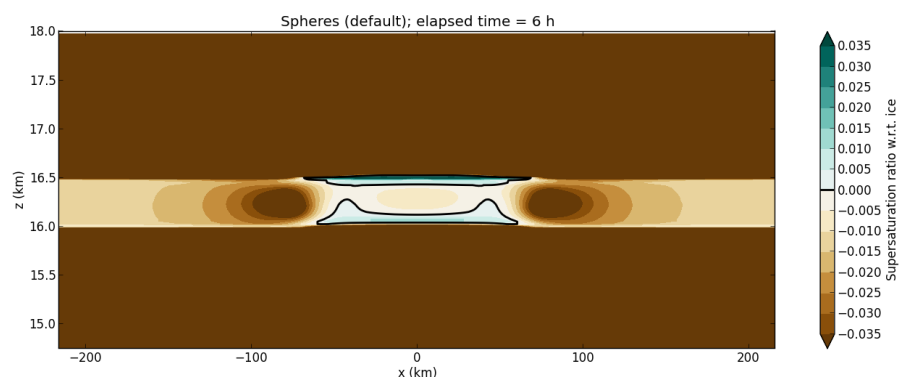
(a)
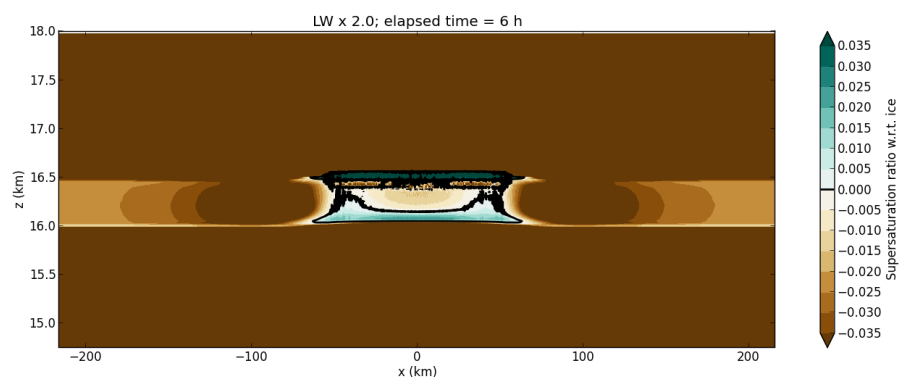
(b)

Figure 4.15: Supersaturation ratio (relative humidity minus 1) with respect to ice at 6 hours in control spherical simulation (a) and simulation with doubled LW absorption (b). The initial cloud was between 16 and 16.5 km, centered at x = 0, and extended out 80 km from the center.

greatest. This points to a role for local diabatic heating in the initial decline in ice mass in the model spin-up period.

Interestingly, the relative humidity is also lower well out to the sides of the cloud in the doubled LW simulation. The temperature perturbation is greater there, presumably due to greater adiabatic compression from the stronger circulation. The sides of the cloud are the regions from which moisture is drawn in order to sustain growth of ice

crystals in the cloud once the circulation has spun up (*Dinh et al.*, 2010). If the relative humidity in the source air for the cloud is lower, it may inhibit the growth of ice crystals later in the simulation.

Another mechanism by which stronger radiative heating might limit the eventual cloud growth is that as the entire cloud is lofted by the stronger circulation, it rises into the region above the original cloud top that was originally at 80% relative humidity. Also, if the cloud top convection is stronger (it has already started by $t = 6$ hours in the doubled LW simulation), it may entrain more dry air into the cloud from above. More investigation is needed to determine which of these processes is most important to the inverse relationship between radiative heating and ice crystal mass in the later part of the cloud evolution.

4.6   Ice crystal size distributions

In order to evaluate whether the model's treatment of microphysics is realistic, it is important to get some sense of the model's agreement with observations. Microphysical observations of ice crystals are typically done using laser instruments that measure the lengths of the crystals along their maximum dimension. Figure 4.16 shows ice crystal size distributions at 24 and 48 hours from the spherical control case and the runs with non-spherical shape considered for both microphysics and radiation. The *x*-axis in these plots is length (diameter for spheres, major axis for spheroids), rather than mass, which is the measure of ice crystal size used elsewhere in this thesis. Observations from *Lawson et al.* (2008) are also shown.

In all of the simulations, the modeled size distributions are too narrow compared with observations, but less so at 48 hours than at 24 hours. This is because the simulations began as a delta function, with all of the ice crystals having the same size (6 μm diameter for spheres, or the equivalent mass for spheroids). While the distribution spreads out in the model over time due to ice crystals growing and sublimating, there has not been enough time even at 48 hours to reach a spread as wide as the observations.
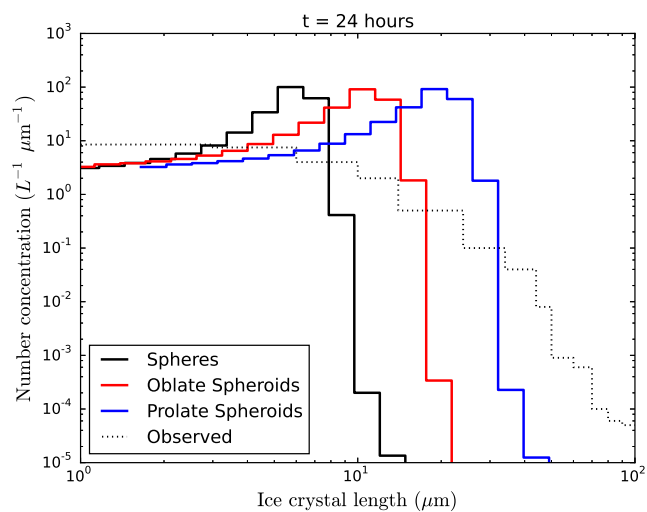
(a)
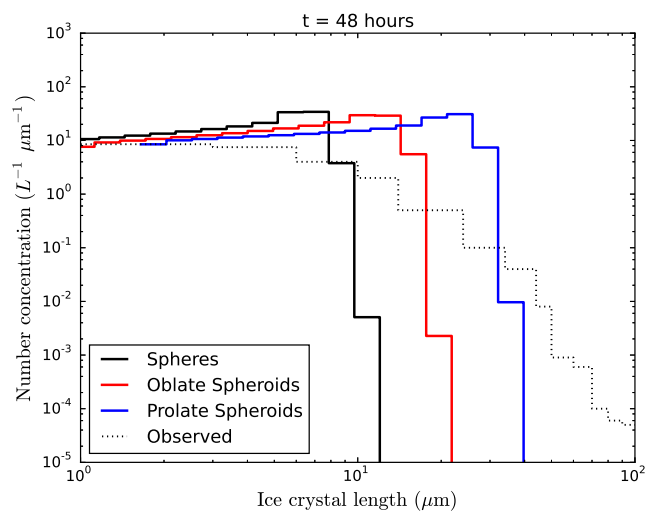
(b)

Figure 4.16: Ice crystal size distributions at (a) 24 hours and (b) 48 hours from runs with all spheres (control), all oblate spheroids and all prolate spheroids with aspect ratios of 6. Observations taken from TTL cirrus over the Eastern Pacific (*Lawson et al.*, 2008).

Dinh et al. (2012) obtained a more realistic spread in the ice crystal size distribution by nucleating ice crystals from aerosols, but could not reproduce observed concentrations of large (greater than about 20 μm in length) ice crystals in observations when assuming a spherical geometry (see their Figure 7a). This was the original motivation for incorporating non-spherical ice crystals into the model. My sphere simulations also underproduce observed large crystals. Switching to oblate or especially prolate spheroids shifts the size distribution further to the right. The spheroidal cases produce more large crystals, but they now produce too few small crystals, at least at 24 hours. This suggests that some sort of intermediate case between all spheres and all spheroids with aspect ratios of 6 would be helpful for producing realistic size distributions.

One way to do an intermediate case would be to assume that the smallest particles are spherical but that the aspect ratio increases as a function of the ice crystal mass. The assumed dependence of the aspect ratio on size could be the same as that used by *Fu et al.* (1998) or *Yang et al.* (2013) when they generated their databases of ice crystal single scattering properties. This strategy would have the added advantage that single-scattering properties have already been calculated, making the radiation parameterization process easier to redo for the new shapes. However, both of these databases assume that the plates or columns have aspect ratios close to 1 for nearly all of the ice crystal masses considered in the microphysics scheme used here, so SAM simulations following those assumptions would be very similar to the spherical control case and therefore probably not very useful.

It is important to note here that the differences in the modeled size distributions in the different cases are due to the chosen assumption about the geometry itself, and not to the effects of the shape on the rate of ice crystal mass growth. Figure 4.10 shows that the variation in the mean ice crystal mass is less than about 10% between the different cases, but Figure 4.16 shows that the prolate spheroids are generally over 3 times longer than the spheres. If mass is held constant, spheroids are more elongated than spheres, so it is not at all surprising that the size distributions will look different when "size" is

defined according to the maximum dimension. Indeed, size distribution plots with mass on the x axis (not shown) look very similar between the spherical, oblate spheroid and prolate spheroid cases. While information about the ice crystal shapes can be collected *in situ* using high-resolution photography, the technology is currently not good enough to resolve shapes for ice crystals less than about 65 μm long (see *Lawson et al.* (2008), Figure 5). Therefore, it is not possible from current measurements to plot observed ice crystal size distributions binned by mass without making untested assumptions about the ice crystal shape.

Chapter 5

CONCLUSION

5.1   Summary of Findings

I have incorporated calculations of fall speeds, growth rates, and longwave radiative absorption for non-spherical ice crystals, specifically oblate and prolate spheroids with aspect ratios of 6 (or plates and columns in the case of the radiation), into a cloud-resolving model suitable for conducting experiments with idealized, optically thin cirrus in the tropical tropopause layer (TTL). Results were compared with control simulations that assumed only spherical crystals; the control simulations were qualitatively similar to those of *Dinh et al.* (2010), but my simulations produced a less massive cloud.

Calculations based on individual ice crystals show that the non-spherical crystals would have slower fall speeds (Figure 2.2), faster rates of growth by deposition and shrinking by sublimation (Figure 2.3), and stronger radiative absorption (Figure 3.5) than spheres of the same mass. The results of the cloud-resolving model simulations show that these changes in the ice crystal habits do in fact affect the time evolution of the cloud, as is evident in plots of domain-integrated variables over time. The full non-spherical simulation produces a cloud center of mass about 75 m higher than the control case after 48 hours. Based on simulations in which the various calculations were changed one at a time, this additional lofting appears to be about 60% due to the reduction in fall speeds, and 40% due to the stronger radiative heating, which increases vertical velocities. For the total cloud ice mass and the mean ice crystal mass, the effects of the different processes are much less straightforward than for the cloud center of mass. There appear to be multiple competing effects. The greater magnitude of the growth rate for non-spherical crystals means that ice crystals grow faster if they are in a supersaturated environment but

sublimate faster if they are in a subsaturated environment. Stronger radiative heating strengthens the radiatively induced circulation, which increases moisture convergence and adiabatic cooling, helping ice crystals grow. But, stronger radiative heating can also increase the temperature locally, which would make ice crystals shrink. Reducing the fall speeds makes ice crystals less likely to sediment out of the cloud, but may also keep them from falling into highly supersaturated regions favorable for growth. In terms of the overall evolution of the cloud, it appears that the effects of non-spherical shape on three physical processes considered–fall speeds, growth rates and radiative absorption– all affect the cloud's time evolution. While the effects do not seem to be extremely important, they are not negligible, either.

Compared with observations, the modeled size distributions are too narrow, probably because the cloud was initially monodisperse. Changing from spheres to spheroids results in a size distribution with more large crystals, but fewer small crystals, when size is measured by the maximum dimension. This is due to the assumption about the geometry and not due to the effect of the assumed shape on the microphysics. Assuming that the aspect ratio increases as size increases may help improve agreement with observations.

Because no airborne instruments yet exist that can accurately resolve the habits of ice crystals of the small sizes commonly seen in TTL cirrus, the shape and the aspect ratio are really unknown, but small crystals do tend to appear roughly equidimensional in microphotographs (*Lawson et al.*, 2008). Therefore, an aspect ratio of 6 should be seen as a relatively extreme case that could bracket the possible effects of ice crystal shape, rather than our best guess as to what the crystals actually look like. However, the model could be modified for other aspect ratios relatively easily, especially for the microphysics. Redoing the radiation parameterization calculations would take more time, but the computational infrastructure is already in place.

It should be noted that the changes made to the cloud-resolving model have a minimal impact on the computational expense. When running on a single node containing

12 processors at the University of Washington's Hyak cluster, the simulations generally take roughly 1 hour to run per 6 hours of model time. The model as it currently exists could be used for many more simulations with relatively little computational cost.

5.2 Future Work

Given the uncertainties in the absorption coefficients calculated for non-spherical crystals using the equivalent surface-area-to-volume ratio spheres method of *Neshyba et al.* (2003), it may make sense to redo these calculations using a more accurate method. There are advantages and disadvantages to many methods available.

One question is whether to try to calculate the properties of oblate and prolate spheroids or plates and columns with facets. Using spheroids has the advantage of being consistent with what I have done with the microphysics, but the lack of facets makes these shapes a less physically realistic representation of the actual ice crystals in TTL cirrus.

Calculating the single-scattering properties for individual non-spherical crystals is a difficult problem. Unlike for spheres, there is no single method currently available that is both exact and computationally feasible for all size parameters for non-spherical ice crystals. The T-Matrix code fails at size parameters well within the range considered in SAM, as discussed in Chapter 3. A method was once developed by Dr. Shoji Asano's group which calculates the single-scattering properties of individual (*Asano and Yamamoto*, 1975) or randomly oriented (*Asano and Sato*, 1980) oblate or prolate spheroids of arbitrary aspect ratio. This code should, in theory, work for all size parameters, but the Fortran code has not been well-maintained since 1980 and I have thus far been unable to get it to work using a modern Fortran compiler. Fixing or rewriting this code and using it to calculate the absorption coefficients for spheroids is one possible direction I could explore in the future.

Several databases of the single-scattering properties of non-spherical ice crystals have been compiled based on extensive calculations (e.g. *Fu et al.*, 1998; *Yang et al.*, 2013), but these databases do not have the calculations for the specific shapes that I

have been simulating in the model. For plates and columns, they assume an aspect ratio that changes as a function of particle size, whereas in my model I am assuming that the aspect ratio is constant. *Yang et al.* (2013) also have made calculations for spheroids with fixed aspect ratios, but the largest aspect ratio considered was 4. One possibility would be to change the model's ice crystal aspect ratio to match that for which radiation calculations have already been done.

Finally, I could perform new calculations for spheroids or plates and columns using the same methods used by *Yang et al.* (2013). For small size parameters, they used the *T*-Matrix code for spheroids and the Amsterdam Discrete Dipole Approximation (ADDA) method (*Yurkin et al.*, 2007) for faceted crystals. For larger size parameters, they used the Improved Geometric Optics Method (IGOM) (*Bi et al.*, 2009), which allows for geometric optics calculations to be extended into size parameters between the Mie scattering and geometric optics regimes. These calculations would be time-consuming because an empirical correction process is required to reconcile differences between the IGOM and Mie scattering results where the two methods overlap. However, I may find it to be the best way to generate a more accurate parameterization of the absorption coefficients for non-spherical ice crystals.

It would be interesting to use the improved SAM model to investigate the effects of thin cirrus on troposphere-stratosphere water vapor exchange, or on the earth's radiation budget. In order for the model simulations to be relevant to these problems, however, it is important that they be constrained by observations of TTL cirrus. Past observations have included ground and space based Lidar data (e.g. from the CALIPSO satellite), as well as *in situ* observations from manned aircraft, but these have been too limited in spatial and temporal extent to constrain cloud-resolving model simulations very well. Many of these limitations have been addressed by the recent Airborne Tropical Tropopause Experiment (ATTREX) field campaign. The campaign involved flights of the NASA Global Hawk unmanned aircraft, which, owing to its exceptional flight duration (30+ hours) and large payload capacity, provided unprecedented observations of

TTL cirrus over a wide temporal and spatial range. Flights were made over the eastern Pacific in 2012, 2013 and 2015, and over the Western Pacific in 2014. The most relevant observations included ice crystal size distributions and habits, water vapor concentrations, temperatures, horizontal and vertical wind speeds, and backscatter profiles from a Lidar mounted on the aircraft. There were also some nearby CALIPSO overpasses during the flight, which provide useful supplementary Lidar data.

Another possible area of future research would be to run 3D instead of 2D simulations. *Grosvenor et al.* (2007) were investigating a similar problem, involving the impact of overshooting deep convection on the humidity of the TTL and lower stratosphere, and found a drying effect in 2D simulations but a moistening effect in 3D simulations, suggesting that a similar discrepancy between 2D and 3D results may also exist for thin TTL cirrus. SAM supports 3D as well as 2D configurations, so the microphysics and radiation schemes currently in use should be easily portable.

Ultimately, between further improvements to the model and incorporation of analysis of observations, it is hoped that insights will be gained that will lead to an improved representation of the physics of thin TTL cirrus in global models in order to aid in the accuracy of predictions of the future of Earth's climate and stratospheric chemistry. The process modeling that Dr. Dinh and I have been doing fills a unique niche in solving these problems, since most current efforts are directed at collecting observations and tuning existing "knobs" in the global models to try to improve agreement with the observations.

BIBLIOGRAPHY

Asano, S., and M. Sato (1980), Light scattering by randomly oriented spheroidal particles, *Applied Optics*, *19*(6), 962–974.

Asano, S., and G. Yamamoto (1975), Light scattering by a spheroidal particle, *Applied Optics*, *14*(1), 29–49.

Bates, D. R., and M. Nicolet (1950), The photochemistry of atmospheric water vapor, *Journal of Geophysical Research*, *55*(3), 301–327, doi:10.1029/JZ055i003p00301.

Bi, L., P. Yang, G. W. Kattawar, B. A. Baum, Y. X. Hu, D. M. Winker, R. S. Brock, and J. Q. Lu (2009), Simulation of the color ratio associated with the backscattering of radiation by ice particles at the wavelengths of 0.532 and 1.064 μm, *Journal of Geophysical Research: Atmospheres*, *114*(D4), D00H08, doi:10.1029/2009JD011759.

Blossey, P. N., and D. R. Durran (2008), Selective monotonicity preservation in scalar advection, *Journal of Computational Physics*, *227*(10), 5160–5183, doi: http://dx.doi.org/10.1016/j.jcp.2008.01.043.

Böhm, H. P. (1989), A general equation for the terminal fall speed of solid hydrometeors, *Journal of the Atmospheric Sciences*, *46*, 2419–2427.

Bougeault, P. (1983), A non-reflective upper boundary condition for limited-height hydrostatic models, *Monthly Weather Review*, *111*, 420–429.

Bougeault, P. (1985), The diurnal cycle of the marine stratocumulus layer: A higher-order model study, *Journal of the Atmospheric Sciences*, *42*, 2826–2843.

Brewer, A. (1949), Evidence for a world circulation provided by the measurement of helium and water vapour distribution in the stratosphere, *Quarterly Journal of the Royal Meteorological Society, 75*, 351–363.

Chen, J.-P., and D. Lamb (1994), Simulation of cloud microphysical and chemical processes using a multicomponent framework. Part I: Description of the microphysical model, *Journal of the Atmospheric Sciences, 51*(18), 2613–2630.

Comstock, J. M., T. P. Ackerman, and G. G. Mace (2002), Ground-based lidar and radar remote sensing of tropical cirrus clouds at nauru island: Cloud statistics and radiative impacts, *Journal of Geophysical Research: Atmospheres, 107*(D23), AAC 16–1–AAC 16–14, doi:10.1029/2002JD002203.

Corti, T., B. P. Luo, Q. Fu, H. Vömel, and T. Peter (2006), The impact of cirrus clouds on tropical troposphere-to-stratosphere transport, *Atmospheric Chemistry and Physics, 6*(9), 2539–2547, doi:10.5194/acp-6-2539-2006.

Dinh, T., and D. R. Durran (2012), A hybrid bin scheme to solve the condensation/evaporation equation using a cubic distribution function, *Atmospheric Chemistry and Physics, 12*(2), 1003–1011, doi:10.5194/acp-12-1003-2012.

Dinh, T., and S. Fueglistaler (2014), Microphysical, radiative and dynamical impacts of thin cirrus clouds on humidity in the tropical tropopause layer and lower stratosphere, *Geophysical Research Letters, 41*, 6949–6955, doi:10.1002/2014GL061289.

Dinh, T., D. Durran, and T. Ackerman (2010), Maintenance of tropical tropopause layer cirrus, *Journal of Geophysical Research (Atmospheres), 115*, D02104, doi:10.1029/2009JD012735.

Dinh, T., D. R. Durran, and T. Ackerman (2012), Cirrus and water vapor transport in the tropical tropopause layer – Part 1: A specific case modeling study, *Atmospheric Chemistry and Physics, 12*(20), 9799–9815, doi:10.5194/acp-12-9799-2012.

Dinh, T., S. Fueglistaler, D. Durran, and T. Ackerman (2014), Cirrus and wter vapour transport in the tropical topopause layer – Part 2: Roles of ice nucleation and sedimentation, cloud dynamics, and moisture conditions, *Atmospheric Chemistry and Physics*, *14*, 12,225–12,236, doi:doi:10.5194/acp-14-12225-2014.

Dinh, T. P. (2009), The maintenance of tropical tropopause layer cirrus, Master's thesis, University of Washington, Seattle, WA, USA.

Dinh, T. P. (2012), Cirrus and water vapor transport in the tropical tropopause layer, Ph.D. thesis, University of Washington, Seattle, WA, USA.

Durran, D. R., T. Dinh, M. Ammerman, and T. Ackerman (2009), The mesoscale dynamics of thin tropical tropopause cirrus, *Journal of the Atmospheric Sciences*, *66*(9), 2859 – 2873.

Dvortsov, V. L., and S. Solomon (2001), Response of the stratospheric temperatures and ozone to past and future increases in stratospheric humidity, *Journal of Geophysical Research: Atmospheres*, *106*(D7), 7505–7514, doi:10.1029/2000JD900637.

Fu, Q., P. Yang, and W. Sun (1998), An accurate parameterization of the infrared radiative properties of cirrus clouds for climate models, *Journal of Climate*, *11*, 2223–2237.

Fuchs, N. A. (1964), *The Mechanics of Aerosols*, Pergamon Press, New York, NY, USA.

Fueglistaler, S., A. E. Dessler, T. J. Dunkerton, I. Folkins, Q. Fu, and P. W. Mote (2009), Tropical tropopause layer, *Reviews of Geophysics*, *47*, RG1004.

Gettelman, A., P. M. d. F. Forster, M. Fujiwara, Q. Fu, H. Vmel, L. K. Gohar, C. Johanson, and M. Ammerman (2004), Radiation balance of the tropical tropopause layer, *Journal of Geophysical Research: Atmospheres*, *109*(D7), D07103, doi:10.1029/2003JD004190.

Grenfell, T. C., and S. G. Warren (1999), Representation of a nonspherical ice particle by a collection of independent spheres for scattering and absorption of radia-

tion, *Journal of Geophysical Research: Atmospheres, 104*(D24), 31,697–31,709, doi: 10.1029/1999JD900496.

Grenfell, T. C., S. P. Neshyba, and S. G. Warren (2005), Representation of a nonspherical ice particle by a collection of independent spheres for scattering and absorption of radiation: 3. hollow columns and plates, *Journal of Geophysical Research: Atmospheres, 110*(D17), D17203, doi:10.1029/2005JD005811.

Grosvenor, D. P., T. W. Choularton, H. Coe, and G. Held (2007), A study of the effect of overshooting deep convection on the water content of the TTL and lower stratosphere from cloud resolving model simulations, *Atmospheric Chemistry and Physics, 7*(18), 4977–5002, doi:10.5194/acp-7-4977-2007.

Hall, W., and H. Pruppacher (1976), The survival of ice particles falling from cirrus clouds in subsaturated air, *Journal of the Atmospheric Sciences, 33*, 1995–2006.

Holton, J. R., and A. Gettelman (2001), Horizontal transport and the dehydration of the stratosphere, *Geophysical Research Letters, 28*(14), 2799–2802, doi: 10.1029/2001GL013148.

Jensen, E., and L. Pfister (2004), Transport and freeze-drying in the tropical tropopause layer, *Journal of Geophysical Research: Atmospheres, 109*(D2), D02207, doi: 10.1029/2003JD004022.

Jensen, E. J., O. B. Toon, H. B. Selkirk, J. D. Spinhirne, and M. R. Schoeberl (1996a), On the formation and persistence of subvisible cirrus clouds near the tropical tropopause, *Journal of Geophysical Research: Atmospheres, 101*(D16), 21,361–21,375, doi:10.1029/95JD03575.

Jensen, E. J., O. B. Toon, L. Pfister, and H. B. Selkirk (1996b), Dehydration of the upper troposphere and lower stratosphere by subvisible cirrus clouds near the tropical tropopause, *Geophysical Research Letters, 23*(8), 825–828, doi:10.1029/96GL00722.

Jensen, E. J., et al. (2008), Formation of large ($\simeq$ 100 μm) ice crystals near the tropical tropopause, *Atmospheric Chemistry and Physics*, *8*(6), 1621–1633, doi:10.5194/acp-8-1621-2008.

Jensen, E. J., L. Pfister, and O. B. Toon (2011), Impact of radiative heating, wind shear, temperature variability, and microphysical processes on the structure and evolution of thin cirrus in the tropical tropopause layer, *Journal of Geophysical Research: Atmospheres*, *116*(D12), D12,209, doi:10.1029/2010JD015417.

Kato, S., T. P. Ackerman, J. H. Mather, and E. E. Clothiaux (1999), The k-distribution method and correlated-k approximation for a shortwave radiative transfer model, *Journal of Quantitative Spectroscopy and Radiative Transfer*, *62*(1), 109 – 121, doi: http://dx.doi.org/10.1016/S0022-4073(98)00075-2.

Khairoutdinov, M. F., and D. A. Randall (2003), Cloud resolving modeling of the ARM summer 1997 IOP: Model formulation, results, uncertainties, and sensitivities., *Journal of the Atmospheric Sciences*, *60*(4), 607–625.

Klemp, J. B., and D. R. Durran (1983), An upper boundary condition permitting internal gravity wave radiation in numerical mesoscale models, *Monthly Weather Review*, *111*, 430–444.

Koop, T., B. Luo, A. Tsias, and T. Peter (2000), Water activity as the determinant for homogeneous ice nucleation in aqueous solutions, *Nature*, *406*, 611–614.

Lamb, D., and J. Verlinde (2011), *Physics and Chemistry of Clouds*, 584 pp., Cambridge University Press, Cambridge, UK.

Lawson, R. P., B. Pilson, B. Baker, Q. Mo, E. Jensen, L. Pfister, and P. Bui (2008), Aircraft measurements of microphysical properties of subvisible cirrus in the tropical tropopause layer, *Atmospheric Chemistry and Physics*, *8*(6), 1609–1620, doi: 10.5194/acp-8-1609-2008.

le Texier, H., S. Solomon, and R. R. Garcia (1988), The role of molecular hydrogen and methane oxidation in the water vapour budget of the stratosphere, *Quarterly Journal of the Royal Meteorological Society, 114*(480), 281–295, doi:10.1002/qj.49711448002.

Liou, K.-N., Q. Fu, and T. P. Ackerman (1988), A simple formulation of the delta-four-stream approximation for radiative transfer parameterizations, *Journal of the Atmospheric Sciences, 45*(13), 1940–1947.

List, R. J. (Ed.) (1984), *Smithsonian meteorological tables*, Smithsonian Institution, Washington, DC, USA.

Mace, G. G., Q. Zhang, M. Vaughan, R. Marchand, G. Stephens, C. Trepte, and D. Winker (2009), A description of hydrometeor layer occurrence statistics derived from the first year of merged Cloudsat and CALIPSO data, *Journal of Geophysical Research: Atmospheres, 114*(D8), n/a–n/a, doi:10.1029/2007JD009755.

Mishchenko, M. I., and L. D. Travis (1998), Capabilities and limitations of a current FORTRAN implementation of the T-matrix method for randomly oriented, rotationally symmetric scatterers, *Journal of Quantitative Spectroscopy and Radiative Transfer, 60*(3), 309 – 324, doi:http://dx.doi.org/10.1016/S0022-4073(98)00008-9.

Mlawer, E. J., S. J. Taubman, P. D. Brown, M. J. Iacono, and S. A. Clough (1997), Radiative transfer for inhomogeneous atmospheres: RRTM, a validated correlated-k model for the longwave, *Journal of Geophysical Research: Atmospheres, 102*(D14), 16,663–16,682, doi:10.1029/97JD00237.

Neshyba, S. P., T. C. Grenfell, and S. G. Warren (2003), Representation of a nonspherical ice particle by a collection of independent spheres for scattering and absorption of radiation: 2. hexagonal columns and plates, *Journal of Geophysical Research: Atmospheres, 108*(D15), 4448, doi:10.1029/2002JD003302.

Newell, R. E., and S. Gould-Stewart (1981), A stratospheric fountain?, *Journal of the Atmospheric Sciences*, *38*, 2789–2796.

Petty, G. (2006), *A First Course in Atmospheric Radiation*, 2nd ed., 458 pp., Sundog Publishing, Madison, WI, USA.

Pruppacher, H. R., and J. D. Klett (1978), *Microphysics of clouds and precipitation*, 1st ed., D. Reidel, Dotrecht, Holland.

Rogers, R. R., and M. K. Yau (1989), *A Short Course in Cloud Physics*, 3rd ed., 304 pp., Butterworth-Heinemann, Woburn, MA, USA.

Solomon, S., R. R. Garcia, F. S. Rowland, and D. J. Wuebbles (1986), On the depletion of Antarctic ozone, *Nature*, *321*, 755–758.

Solomon, S., K. Rosenlof, R. W. Portmann, J. S. Daniel, S. M. Davis, T. J. Sanford, and G.-K. Plattner (2010), Contributions of stratospheric water vapor to decadal changes in the rate of global warming, *Science*, *327*, 1219–1223.

Stamnes, K., S.-C. Tsay, W. Wiscombe, and K. Jayaweera (1988), Numerically stable algorithm for discrete-ordinate-method radiative transfer in multiple scattering and emitting layered media, *Appl. Opt.*, *27*(12), 2502–2509, doi:10.1364/AO.27.002502.

Stamnes, K., S.-C. Tsay, and I. Laszlo (2000), DISORT, a general-purpose Fortran program for discrete-ordinate-method radiative transfer in scattering and emitting layered media: Documentation of methodology, *Tech. rep.*, NASA, version 1.1.

Taylor, J. R., W. J. Randel, and E. J. Jensen (2011), Cirrus cloud-temperature interactions in the tropical tropopause layer: a case study, *Atmospheric Chemistry and Physics*, *11*(19), 10,085–10,095, doi:10.5194/acp-11-10085-2011.

Toon, O. B., and T. P. Ackerman (1981), Algorithms for the calculation of scattering by stratified spheres, *Appl. Opt.*, *20*(20), 3657–3660, doi:10.1364/AO.20.003657.

Toon, O. B., C. McKay, T. Ackerman, and K. Santhanam (1989), Rapid calculation of radiative heating rates and photodissociation rates in inhomogeneous multiple scattering atmospheres, *Journal of Geophysical Research, 94*(D13), 16,287–16,301.

Virts, K. S., and J. M. Wallace (2010), Annual, interannual, and intraseasonal variability of tropical tropopause transition layer cirrus, *Journal of the Atmospheric Sciences, 67*, 3097–3112.

Wang, P.-H., P. Minnis, M. P. McCormick, G. S. Kent, and K. M. Skeens (1996), A 6-year climatology of cloud occurrence frequency from Stratospheric Aerosol and Gas Experiment II observations (1985-1990), *Journal of Geophysical Research, 101*(D23), 29,407–29,429.

Warren, S. G. (1984), Optical constants of ice from the ultraviolet to the microwave, *Appl. Opt., 23*(8), 1206–1225, doi:10.1364/AO.23.001206.

Warren, S. G., and R. E. Brandt (2008), Optical constants of ice from the ultraviolet to the microwave: A revised compilation, *Journal of Geophysical Research: Atmospheres, 113*(D14), D14220, doi:10.1029/2007JD009744.

Winker, D. M., and C. R. Trepte (1998), Laminar cirrus observed near the tropical tropopause by LITE, *Geophysical Research Letters, 25*(17), 3351–3354, doi:10.1029/98GL01292.

Yang, P., L. Bi, B. A. Baum, K.-N. Liou, G. W. Kattawar, M. I. Mishchenko, and B. Cole (2013), Spectrally consistent scattering, absorption, and polarization properties of atmospheric ice crystals at wavelengths from 0.2 to 100 μm, *Journal of the Atmospheric Sciences, 70*, 330–347.

Yurkin, M., V. Maltsev, and A. Hoekstra (2007), The discrete dipole approximation for simulation of light scattering by particles much larger than the wavelength, *Jour-*

83

nal of Quantitative Spectroscopy and Radiative Transfer, 106(13), 546 – 557, doi: http://dx.doi.org/10.1016/j.jqsrt.2007.01.033.

Appendix A

SENSITIVITY OF PARAMETERIZED ABSORPTION CROSS SECTIONS FOR SPHERES TO ICE OPTICAL CONSTANTS

It appears from Figures 3.2 and 3.3 that the wavelength chosen within each RRTM band would affect the ice optical constants, and therefore the parameterized absorption cross sections, more than whether the old (*Warren*, 1984) or new (*Warren and Brandt*, 2008) optical constants of ice were used. This is especially true for the longest-wavelength band, where the imaginary index of refraction varies over several orders of magnitude. It is not obvious exactly which wavelengths to use when running the Mie scattering code to compute the single-scattering properties for use in the radiative transfer model. Tra Dinh used the midpoints of the RAPRAD bands in wavelength space; in my analysis I have used the midpoints of the RRTM bands in wavenumber space.

To try to constrain the possible error caused by this uncertainty, I have repeated the process of generating absorption cross sections for spheres using RRTM, but I have used the maximum and minimum values of the refractive index found in each bin, rather than the values at the bin's middle wavenumber, when calculating the single-scattering properties. I changed the real and imaginary index separately, continuing to use the midpoint values for the index not being changed, resulting in four cases called "MaxI, MinI, MaxR, and MinR", with "I" referring to the imaginary index being changed and "R" referring to the real index being changed. The results of these tests are shown in Table A.1.

For bulk ice, the real index of refraction is associated with bending of light in a geo-metric optics sense, while the imaginary index is associated with the absorption of light. Therefore, I would expect the parameterized absorption cross section from the MaxI

r (μm)	Control	MaxI	MinI	MaxR	MinR
1.0	6.65×10^{-13}	8.80×10^{-13}	3.49×10^{-13}	6.45×10^{-13}	6.70×10^{-13}
2.2	6.81×10^{-13}	8.29×10^{-13}	4.09×10^{-13}	7.02×10^{-13}	6.59×10^{-13}
3.4	2.23×10^{-13}	2.54×10^{-11}	1.51×10^{-11}	2.34×10^{-11}	2.11×10^{-11}
4.6	4.76×10^{-11}	5.22×10^{-11}	3.52×10^{-11}	5.01×10^{-11}	4.51×10^{-11}
5.8	8.22×10^{-11}	8.74×10^{-11}	6.53×10^{-11}	8.64×10^{-11}	7.84×10^{-11}
7.0	1.27×10^{-10}	1.32×10^{-10}	1.07×10^{-10}	1.33×10^{-10}	1.22×10^{-10}
8.2	1.79×10^{-10}	1.85×10^{-10}	1.59×10^{-10}	1.87×10^{-10}	1.74×10^{-10}
9.4	2.42×10^{-10}	2.48×10^{-10}	2.23×10^{-10}	2.51×10^{-10}	2.37×10^{-10}
10.6	3.10×10^{-10}	3.21×10^{-10}	2.97×10^{-10}	3.21×10^{-10}	3.08×10^{-10}
11.8	3.91×10^{-10}	4.06×10^{-10}	3.86×10^{-10}	4.03×10^{-10}	3.91×10^{-10}
13.0	4.79×10^{-10}	4.99×10^{-10}	4.81×10^{-10}	4.94×10^{-10}	4.81×10^{-10}
15.5	7.00×10^{-10}	7.22×10^{-10}	7.23×10^{-10}	7.17×10^{-10}	7.02×10^{-10}
22.9	1.56×10^{-9}	1.60×10^{-9}	1.70×10^{-9}	1.58×10^{-9}	1.58×10^{-9}
33.8	3.39×10^{-9}	3.45×10^{-9}	3.75×10^{-9}	3.42×10^{-9}	3.44×10^{-9}
50.0	7.32×10^{-9}	7.35×10^{-9}	8.02×10^{-9}	7.34×10^{-9}	7.40×10^{-9}

Table A.1: Parameterized LW absorption cross sections (m^{-2}) from sensitivity tests to changes in ice optical constants. The "Control" case is the same as the "RRTM (new optical constants)" case from Table 3.2 and uses the optical constants of ice at the midpoints, in wavenumber space, of each RRTM band (see Figures 3.2 and 3.3). "MaxI" and "MinI" cases use the maximum and minimum values, respectively, of the imaginary index of refraction within each RRTM band, with midpoint values used for the real index. "MaxR" and "MinR" cases use the maximum and minimum values, respectively, of the real index of refraction within each RRTM band, with midpoint values used for the imaginary index.

case to be greater than that from the MinI case, and that control case would be between these two. Table A.1 shows that these conditions are met only for particles smaller than

13.0 microns. I would attribute the deviations from this expectation to the fact that scattering becomes more important as the particles get larger (which can be verified from the single-scattering albedos output by the T-Matrix code), and that RRTM considers both scattering and absorption but our parameterization combines both of these effects into a single number representing absorption.

The MaxR and MinR cases generally differ from the control case by less than the MaxI and MinI cases do, as I would expect because the real index of refraction varies less within the bands than the imaginary index does (see Figures 3.2 and 3.3–note that the imaginary index figure has a y-axis on a log scale, while the real index figure does not.) The differences caused by changing the real index of refraction are not systematic–the sign of the MaxR-MinR difference changes twice, and for particles with radius 13.0 microns or larger, the control case is not between either of them. I would attribute this lack of systematicity to the fact that these changes to the real index of refraction affect the absorption as well as the scattering cross sections output by the T-Matrix code. Similarly, the imaginary index of refraction affects the scattering, in addition to the absorption.

I had hoped to be able to show that the results from these sensitivity tests would envelop the difference between the "RAPRAD" and "RRTM (new optical constants)" cases shown in Table 3.2. In fact, for all radii except 10.6 through 15.5 μm, at least one of the sensitivity tests listed accounts for the difference between these cases, and for the remaining radii, the RAPRAD result can be obtained for by adding the difference between the old and new optical constants cases for RRTM to the MaxI case. Therefore, I would argue that the differences between my and Dr. Dinh's parameterized absorption cross sections for spherical ice crystals are not significant because they can be accounted for by possible errors in the optical constants of ice. I am taking my new values as the control case for the non-spherical crystals not because I believe my values are more correct than Dr. Dinh's, but because I need to keep the methods as consistent as possible in order to isolate the effects of ice crystals' shape on their radiative properties.

Appendix B

ON THE RELATIVE CONTRIBUTIONS OF SHORTWAVE AND LONGWAVE ABSORPTION

The absorption of shortwave radiation is important for the dynamics of various types of clouds, for example causing a diurnal cycle in marine stratocumulus (*Bougeault*, 1985). Therefore, it may be surprising to some readers that shortwave absorption is relatively unimportant compared to longwave absorption for optically thin cirrus. If shortwave absorption was on the same order of magnitude as longwave absorption, then it would be hard to justify considering the effect of the ice crystal shape on the longwave but not the shortwave absorption, or not including a diurnal cycle of incident solar radiation in the cloud-resolving model.

The LW absorption cross sections in Table 3.1 are about two orders of magnitude larger than the SW absorption cross sections. However, this does not tell us everything we need to know about the relative importance of SW and LW heating, because there may be more solar radiation than longwave radiation coming into the cloud. Instead, we need to look at the radiative heating rates from the radiative transfer model simulations that were used to generate the lookup table of absorption cross sections used in the cloud-resolving model. I have not run RRTM in the shortwave case, but Tra Dinh ran RAPRAD for both the shortwave and the longwave during her M.S. thesis work, and recorded the results.

Table B.1 shows the in-cloud flux longwave and shortwave radiative flux convergence, a quantity proportional to the radiative heating, calculated by Tra Dinh using RAPRAD. These calculations were performed for a cirrus cloud with a longwave optical depth of .005, and the flux convergence in the cloud layer from a clear-sky case has

r (μm)	1.0	2.2	3.4	4.6	5.8	7.0	8.2	9.4	10.6	11.8	13.0	15.5	22.9	33.8	50.0
LW FC (W m^{-2})	1.32	1.35	1.33	1.34	1.34	1.32	1.37	1.36	1.33	1.35	1.31	1.30	1.36	1.34	1.32
SW FC (W m^{-2})	.190	.184	.162	.156	.152	.141	.148	.148	.149	.157	.149	.161	.196	.234	.290
SW/LW ratio	.144	.136	.122	.116	.113	.107	.108	.109	.112	.116	.113	.124	.144	.175	.219

Table B.1: Longwave and shortwave flux convergences, to 3 significant digits, calculated using RAPRAD for a cirrus cloud with a longwave optical depth of .005, composed of spherical ice crystals of various sizes, at noon. Flux convergence due to gases has already been subtracted out. Calculations done by Tra Dinh in 2009.

been subtracted out to isolate the effects of the cloud. The ratio of the SW to the LW flux convergence varies from 10.7% to 21.9%, depending on the ice crystal size. Most of the crystals in the SAM simulations are towards the smaller end of the size range, where the SW/LW ratio is less than 15%. Therefore, the SW heating can be said to be weaker than the LW heating by an order of magnitude.

These simulations were done assuming zero zenith angle, and therefore place an upper bound on the relative importance of shortwave absorption. Averaged over the diurnal cycle, the ratio of SW to LW heating would be much less than that shown in the table. If the effect of shape on the shortwave radiative heating was similar to that for the longwave (Figure 3.5), then the variation in the total radiative heating caused by the effect of ice crystal shape on the SW heating would be at most a few percent and probably less than 1%. Therefore, the effect of ice crystal shape on the SW radiative heating is not likely to be an important factor in the cloud dynamics, which implies that redoing the parameterization of ice crystal absorption cross sections to account for the effect of shape on the shortwave heating should not be a very high priority.

The tabulated SW/LW ratios also place an upper bound on any dirunal cycle in these clouds. A roughly 10-15% variation in the total cloud radiative heating was not thought to be very important, and therefore Tra Dinh took out the diurnal cycle of SAM, instead assuming a constant solar zenith angle of 40°.

In optically thicker clouds, such as thicker cirrus or marine stratocumulus, the long-wave radiation from the surface would be quickly attenuated in the lowermost portion of the cloud. In that case, shortwave radiation incident from above would be the dominant contributor to radiative heating in most of the cloud. This is responsible for the observed diurnal cycle in these clouds. For the clouds I am studying however, the LW optical depth is on the order of .01, so the LW radiative heating penetrates through the entire thickness of the cloud and is an order of magnitude more important than the SW heating at both the top and the bottom of the cloud.

Appendix C

MODEL RUNS WITH A DIFFERENT INITIAL HUMIDITY PROFILE

I ran a different set of SAM simulations in which the initial water vapor profile was different from that in the simulations presented in Chapter 4 and from those described by *Dinh et al.* (2010).[12]

In the simulations presented here, the vapor profile is initialized according to the following equation:

$$q_v(z) = 0.8q_{v,s}^* + 0.2q_{v,s}^* g(z) \tag{C.1}$$

where q_v is the water vapor mixing ratio, $q_{v,s}^*$ is the saturation mixing ratio at the altitude of the cloud center, and $g(z)$ is defined according to Equation 4.3. Figure C.1 shows the vertical profiles of the temperature and the absolute and relative (with respect to ice) humidity at the beginning of the simulation. Because the absolute humidity is referenced to the center of the cloud while the temperature in the cloud decreases with height, much of the cloud, especially the lower half, is initially subsaturated. A real cirrus cloud would be expected to have a subsaturated layer at the bottom due to ice crystals sedimenting out, so a subsaturated layer in the lower portion of the cloud is not an unrealistic assumption. Also, there is a supersaturated layer that starts about 0.5 km above

---

[1]I actually ran the simulations presented here first. This was the configuration of SAM when I received the code from Tra Dinh. I did not check what the water vapor profile was set to until long after I had run the simulations. I am not sure why the model was ever set up to run this way, but it may have been thought that a vapor profile with sharp boundaries between 100% and 80% relative humidity at the top and bottom of the cloud was unrealistic, a concern mentioned by *Dinh et al.* (2010).

[2]The simulations presented in this appendix, except for the spherical control case, contained an error in the bin microphysics scheme implementation in which lower bin boundary masses instead of bin mean masses were used when calculating the growth rates of ice crystals, thus underestimating the growth rates. This error had a small effect on the results, for example a 10 m difference in the cloud ice center of mass at 48 hours. This error has been corrected in all of the simulations described and plotted in the main body of the text.

the top of the cloud, but this does not result in the formation of a second cloud because ice nucleation is not considered, and in any case it is well below the roughly 60% super-saturation threshold required for homogeneous nucleation (*Koop et al.*, 2000).
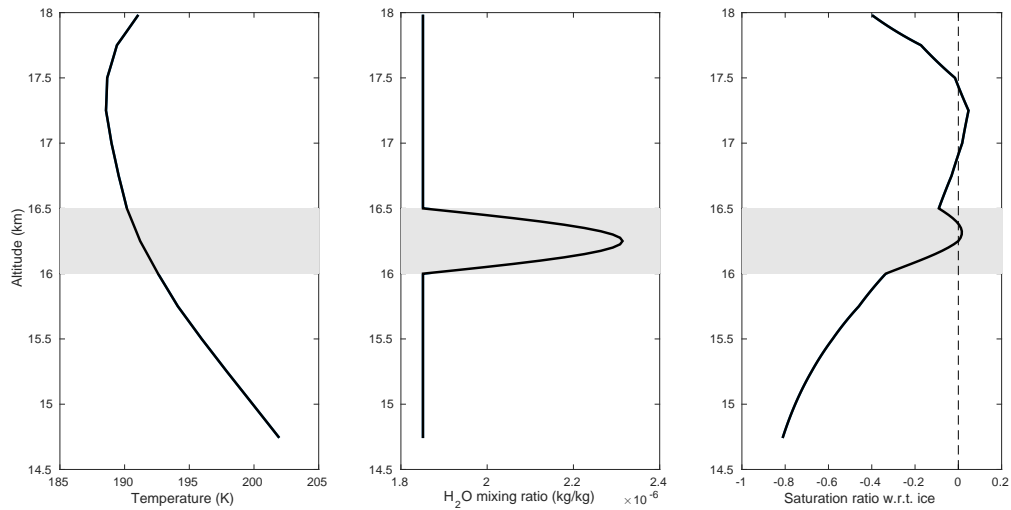

Figure C.1: Initial profiles of temperature (left), water vapor mixing ratio (center), and relative humidity with respect to ice (right). The dashed line indicates supersaturation. The gray rectangle indicates the initial location of the cloud. At the beginning of these simulations, these quantities do not depend on x, although the ice number concentration does.

Figure C.2 shows the u, w and θ' fields at 6 hours elapsed time in the control (spherical) case for these simulations. Comparison with Figure 4.3 shows that the radiatively induced circulation is slightly weaker with the altered humidity profile. The region of positive θ' associated with the diabatic heating is slightly thinner due to sublimation in the initially subsaturated lower part of the cloud.

Figure C.3 shows the ice mixing ratio at 24 hours for the spherical case for these simulations. These runs went out to only 24 hours rather than 48 hours. In this case, the
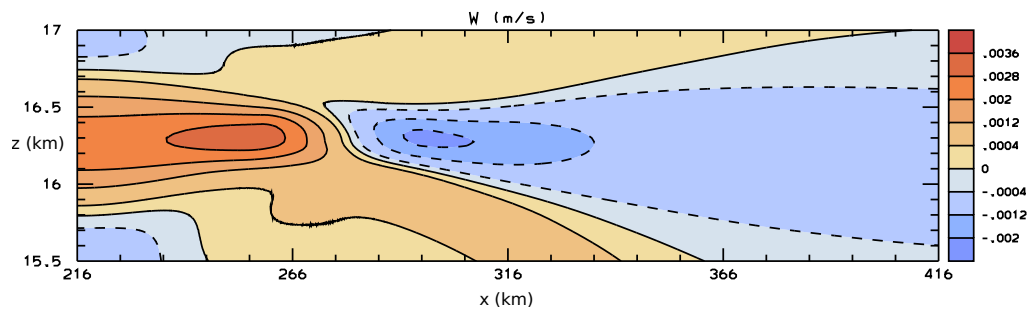
(a)
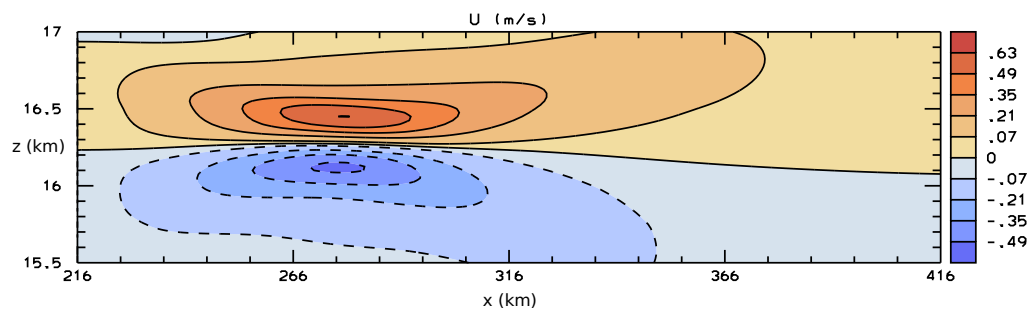
(b)
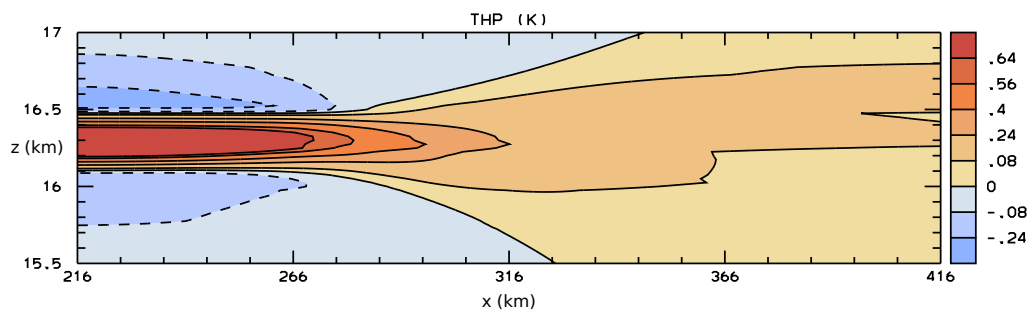
(c)

Figure C.2: Plots of vertical velocity (a), zonal velocity (b), and potential temperature perturbation (c) at an elapsed time of 6 hours for a SAM cloud-resolving model simulation with all spherical crystals. *cf. Dinh et al.* (2010), their Figure 3.

cloud bottom is higher up at 24 hours than at the beginning of the simulation, unlike in the case where the entire cloud is initially saturated (see Figure 4.4a). This is due to sublimation in the originally subsaturated layer in the bottom half of the cloud.
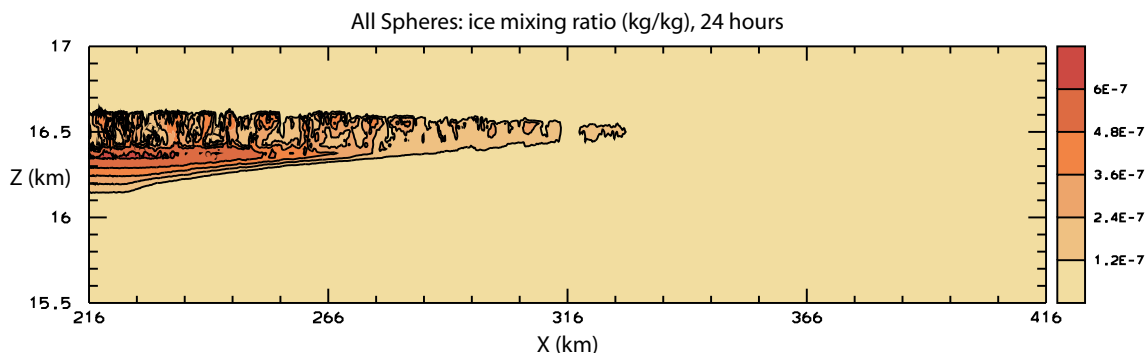
Figure C.3: Ice mixing ratio at 24 hours for the control simulation with all spheres. Compare to Figure 4.4a and to *Dinh et al.* (2010), their Figure 6b.

Figures C.4 through C.9 show time series of domain integrated quantities, including center of cloud ice mass, total cloud ice mass and mean ice crystal mass, for these runs. They are analogous to the first 24 hours shown in Figures 4.5 through 4.10. Figures C.4 through C.6 show the effect of considering spheroidal shape in the fall speed and growth rate calculations alone and together. Figures C.7 through C.9 the effects of also considering non-spherical shape in the radiation calculation.

The center of mass plots (Figures C.4 and C.7) show similar results to those shown in Chapter 4, in that the effect of the microphysics on the center of mass is entirely due to the fall speed and not the growth rate, and that the additional radiative heating associated with the non-spherical shape results in further lofting of the cloud. What is different here is that in all of the simulations with the initially subsaturated lower half of the cloud, the center of mass is higher after 24 hours than in the corresponding simulation in which the entire cloud was initially saturated. Sublimation in the subsaturated bottom half raises the center of mass.

In all the simulations shown here, the initial decline in the total ice mass and the mean ice crystal mass is much steeper than in Chapter 4, and the subsequent rebound is much weaker. This is also due to the sublimation in the lower portion of the cloud. The rebound is slightly stronger in the mean crystal mass than in the total ice mass, because ice crystals that completely sublimate away are no longer counted in the mean crystal mass calculation.

In general, considering the non-spherical geometry of the ice crystals in the fall speed, growth rate and radiative absorption calculations has similar effects in these simulations as in the simulations shown in Chapter 4. However, there are broad differences between the entire envelopes of simulations, especially for the mean ice crystal mass and total cloud ice mass, indicating that the initial relative humidity profile affects these quantities much more than the shape of the ice crystals does. This suggests that when observing TTL cirrus, the temperature and water vapor profiles, which determine the relative humidity, are very important quantities to measure.
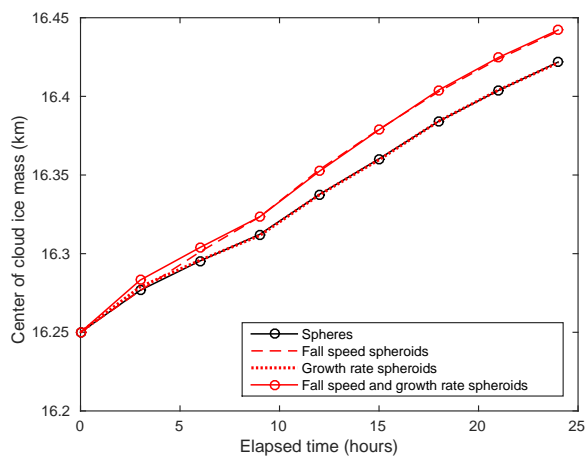
(a)
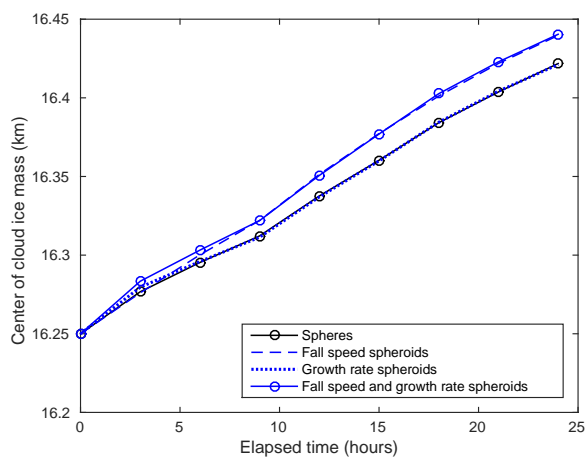
(b)

Figure C.4: Cloud center of mass as a function of time, for spheres (black, both panels) and oblate (red, (a)) and prolate (blue, (b)) spheroids with aspect ratios of 6. Dashed lines: spheroidal shape considered only for fall speed. Dotted lines: spheroidal shape considered only for growth rate. Solid colored lines: spheroidal shape considered for both fall speeds and growth rates.
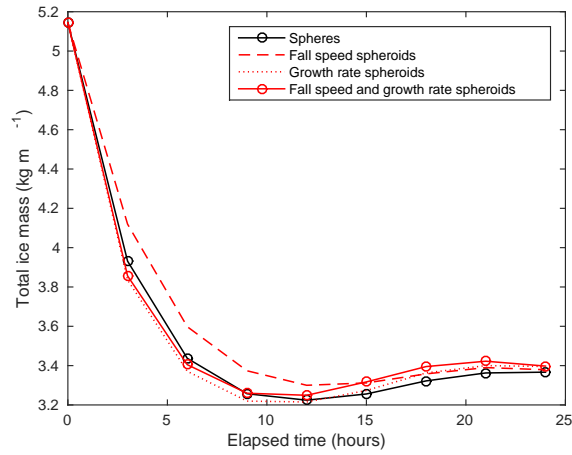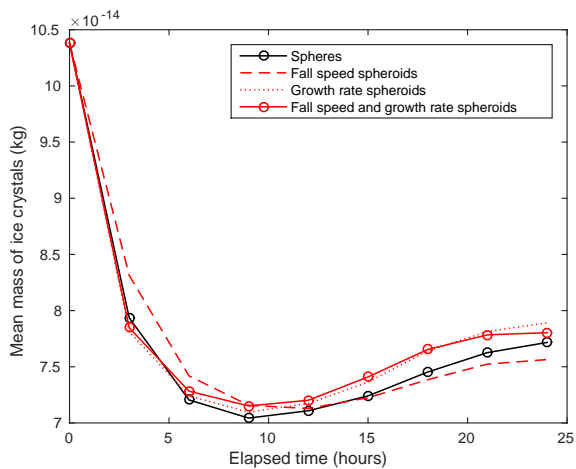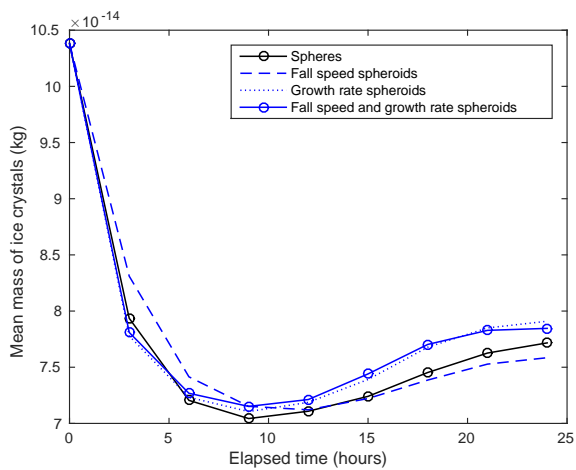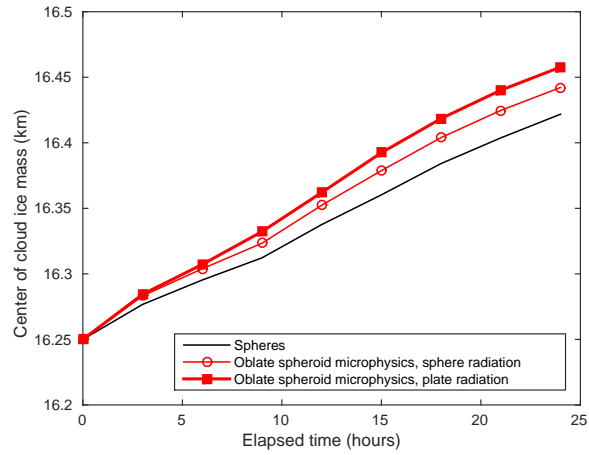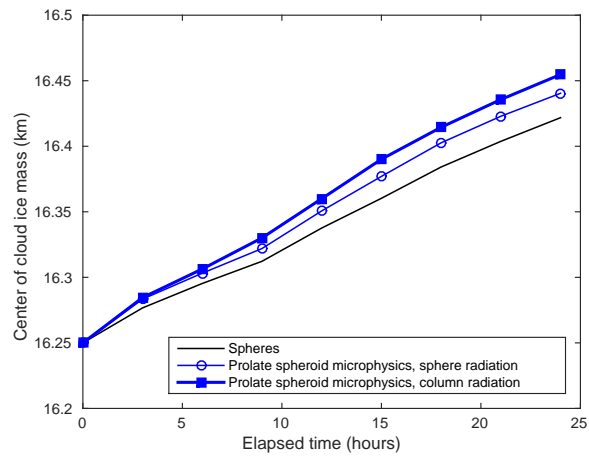
(a)
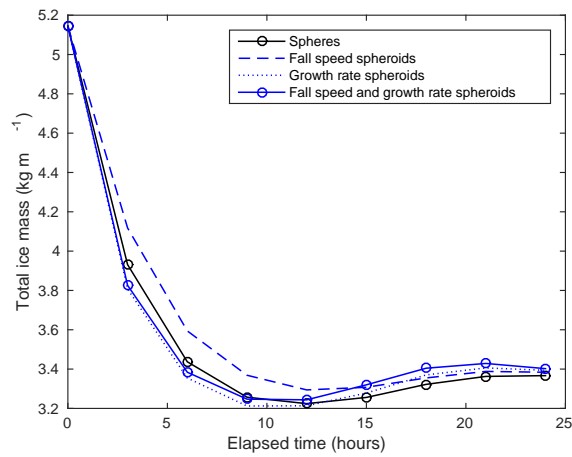
(b)

Figure C.5:   Total cloud ice mass (kg per m in *y* direction) as a function of time, for spheres (black, both panels) and oblate (red, (a)) and prolate (blue, (b)) spheroids with aspect ratios of 6. Dashed lines: spheroidal shape considered only for fall speed. Dotted lines: spheroidal shape considered only for growth rate. Solid colored lines: spheroidal shape considered for both fall speeds and growth rates.
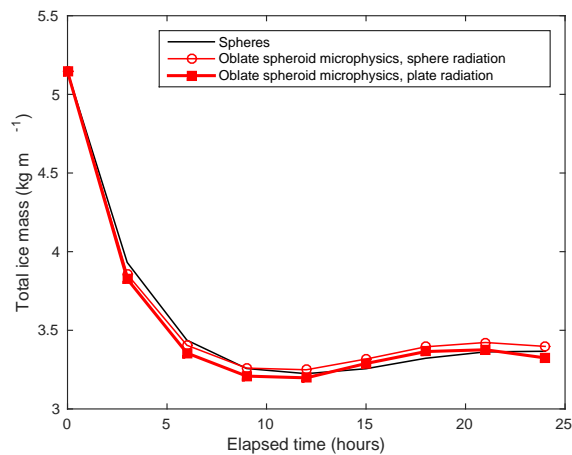
(a)

(b)

Figure C.6: Mean ice crystal mass (kg) as a function of time, for spheres (black, both panels) and oblate (red, (a)) and prolate (blue, (b)) spheroids with aspect ratios of 6. Dashed lines: spheroidal shape considered only for fall speed. Dotted lines: spheroidal shape considered only for growth rate. Solid colored lines: spheroidal shape considered for both fall speeds and growth rates.
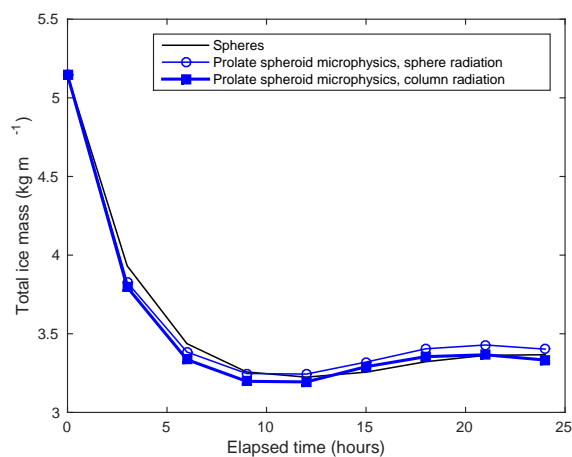
(a)

(b)

Figure C.7: Cloud center of mass as a function of time, for spheres (black, both panels; control case) and oblate (red, (a)) and prolate (blue, (b)) spheroids with aspect ratios of 6. Thin, colored lines: non-spherical shape considered for fall speed and growth rate only. Thick, colored lines: non-spherical shape considered for fall speed, growth rate, and LW radiative absorption.
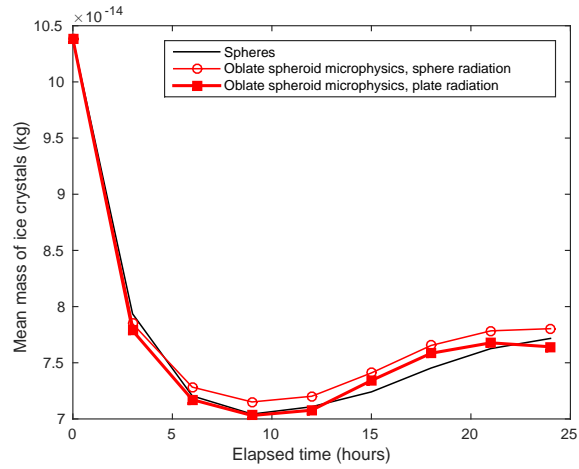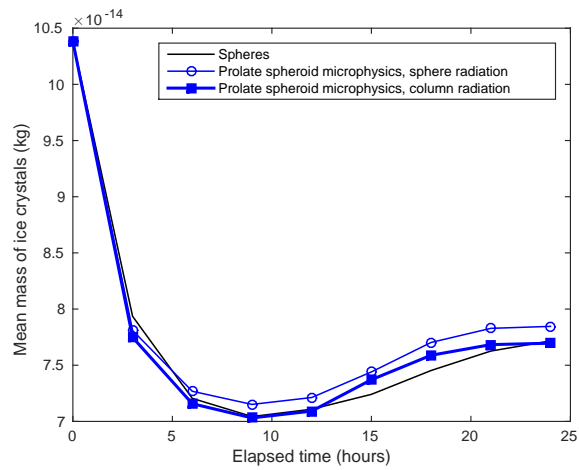
(a)

(b)

Figure C.8: Total cloud ice mass (kg per m in y direction) as a function of time, for spheres (black, both panels; control case) and oblate (red, (a)) and prolate (blue, (b)) spheroids with aspect ratios of 6. Thin, colored lines: non-spherical shape considered for fall speed and growth rate only. Thick, colored lines: non-spherical shape considered for fall speed, growth rate, and LW radiative absorption.

(a)

(b)

Figure C.9: Mean ice crystal mass (kg) as a function of time, for spheres (black, both panels; control case) and oblate (red, (a)) and prolate (blue, (b)) spheroids with aspect ratios of 6. Thin, colored lines: non-spherical shape considered for fall speed and growth rate only. Thick, colored lines: non-spherical shape considered for fall speed, growth rate, and LW radiative absorption.